APPLICATIONS OF THE ATOM-OPTICAL KICKED ROTOR

By

RAJENDRA KUMAR SHRESTHA

Master of Science in Physics
Tribhuvan University
Kirtipur, Kathmandu, Nepal
2003

Master of Science in Physics
Southern Illinois University
Edwardsville, Illinois, USA
2008

Submitted to the Faculty of the
Graduate College of
Oklahoma State University
in partial fulfillment of
the requirements for
the Degree of
DOCTOR OF PHILOSOPHY
May, 2013

APPLICATIONS OF THE ATOM-OPTICAL KICKED ROTOR

Dissertation Approved:

Gil Summy

Dissertation Advisor

Albert T. Rosenberger

Yingmei Liu

Nicholas F. Materer

TABLE OF CONTENTS

Chapter Page

LIST OF FIGURES

Figure Page

CHAPTER 1

INTRODUCTION

1.1 Historical overview of Bose-Einstein condensation

The history of Bose-Einstein condensation starts in 1924 with the notion of Satyendra Nath Bose's statistical argument in deriving the black-body photon spectrum [1]. This concept was later extended and generalized to the case of noninteracting atoms by Albert Einstein [2, 3] which is now known as Bose-Einstein statistics. This predicted that at very low but finite temperature a large fraction of the atoms would go into the lowest energy quantum state. This phenomenon is now known as Bose-Einstein condensation (BEC). Some good reviews on BEC can be found in references [4–6].

Einstein's prediction was not taken seriously until mid 1930s when Fritz London and Laszlo Tisza revived those ideas as a possible mechanism underlying superfluidity in liquid Helium-4 [7, 8]. This was in fact the first work to suggest that BEC displays quantum behavior on a macroscopic scale. BEC is a genuinely quantum statistical phase transition that occurs without the help of interactions. Einstein called it "condensation without interaction" [3] to draw the contrast to most phase transitions that occur due to the interactions between the constituent particles. For example, ferromagnetism is caused due to the spin exchange interaction [9,10] and superconductivity occurs due to the effective interactions between electrons [11, 12]. The occurrence of the transition to BEC requires a phase space density roughly greater than unity. More precisely the transition occurs when the de Broglie wavelength, λ_{dB}, of atoms overlap each other. For a noninteracting Bose gas, the phase space density, $n\lambda_{dB}^3$, should be approximately greater than 2.61 (see section 1.2).

It took about 70 years in order for scientists to finally realize a BEC in dilute gases in a series of remarkable experiments in 1995 [13–15]. Eric Cornel and Carl Wieman's group at JILA, University of Colorado, Boulder, created a BEC of ^{87}Rb atoms [13], Wolfgang Ketterle's group at MIT, created a BEC of Na atoms [14], and Randall Hulet's group at Rice University, created a BEC of ^{7}Li atoms [15–17]. It should be mentioned here that the effort on BEC was begun with hydrogen a long time before. However the first observation of BEC in spin-polarized hydrogen was not reported until 1998 [18]. Towards the realization of BEC, some other remarkable discoveries should not be forgotten. These include: the demonstration of the idea of the magneto-optical trap (MOT) by Migdall, *et al* (1985) [19], the first observation of optically trapped atoms by Chu, *et al.* (1986) [20], realization of a MOT by Rabb, *et al.* (1987) [21], demonstration of evaporative cooling by Davis, *et al.* and Petrich *et al.* (1994) [22, 23], and the demonstration of a time orbiting potential by Petrich, *et al.* (1995) [24]. These incredible works opened the pathway to the realization of the BEC, revolutionizing the field of atomic physics. Two Nobel prizes were awarded for these remarkable achievements: laser cooling (1997) and BEC (2001).

A BEC of ^{87}Rb atoms is produced in our lab at Oklahoma state University using an all-optical trap, which has proved to be a simple, yet robust method [25,26]. An in-depth discussion of BEC in the Summy group can be found in the theses of Ahmadi, Timmons, Behin Aein, Ramareddy, and Talukdar [27–31].

1.2 Fundamentals of Bose-Einstein condensation

Quantum statistics is governed by the principle of indistinguishability of identical particles. Particles with integer spin are called bosons and half integer spins are called fermions. Photons are example of bosons whereas the elementary particles such as electrons, protons, neutrons, quarks and neutrinos are examples of fermions. Thus an atom with an even number of total constituent particles is a boson. Bosons obey

Bose-Einstein statistics in which there is no restriction on the occupation number of any single-particle state. However in the case of fermions, no more than one particle can occupy any single-particle state (Pauli's exclusion principle [32]). Moreover the many-body wave function of identical bosons is symmetric under the exchange of any two bosons. For identical fermions, such an exchange is anti-symmetric.

The grand partition function, Ξ, of a system of particles with particle-number operator $\hat{N}$ and the Hamiltonian $\hat{H}$ is given by

$$\Xi = \mathrm{Tr} e^{-\beta'(\hat{H}-\mu\hat{N})}, \tag{1.1}$$

where $\beta' = 1/(k_B T)$ with k_B and T the Boltzman constant and temperature respectively, and μ is the chemical potential which serves as the Lagrange multiplier. For an ideal Bose gas (i.e., noninteracting identical bosons) with the dispersion relation $\epsilon_k = \hbar^2 k^2/2M$, one can write

$$\hat{H} - \mu\hat{N} = \sum_k (\epsilon_k - \mu)\hat{n}_k. \tag{1.2}$$

Where $\hat{n}_k$ is the number operator of a particle with wave vector k. Thus Eq. (1.1) can be written as

$$\Xi = \Pi_k \sum_{n_k=0}^{\infty} [e^{\beta'(\mu-\epsilon_k)}]^{n_k}. \tag{1.3}$$

This is a geometric series which converges only if $e^{\beta'(\mu-\epsilon_k)}$ is less than one. It requires $\mu < 0$ provided $\epsilon_k \geq 0$. Then Eq. (1.3) becomes

$$\Xi = \Pi_k \frac{1}{1 - e^{\beta'(\mu-\epsilon_k)}}. \tag{1.4}$$

With this grand partition function the thermodynamic potential can be defined as

$$\Omega = -\frac{1}{\beta'} \ln \Xi = \sum_k \frac{1}{\beta'} \ln(1 - e^{\beta'(\mu-\epsilon_k)}). \tag{1.5}$$

This leads to the Bose-Einstein distribution function

$$N = \sum_k \bar{n}_k = \sum_k \frac{1}{e^{\beta'(\epsilon_k-\mu)} - 1}. \tag{1.6}$$

Where $\bar{n}_k = -\frac{\partial \Omega_k}{\partial \mu}$ is the average number of particles with wave vector k and N is the average total number of bosons. In the thermodynamic limit in which both the volume V and N are infinitely large, the sum in Eq. (1.6) can be replaced by an integral i.e., $\sum_k \rightarrow \frac{V}{(2\pi)^3}\int \mathrm{d}^3k$ then Eq. (1.6) becomes

$$\frac{N}{V} = \frac{1}{(2\pi)^3}\int \mathrm{d}^3k \frac{1}{e^{\beta'(\epsilon_k - \mu)} - 1}. \tag{1.7}$$

If the temperature is reduced maintaining the particle number density, $n = N/V$ a constant, the value of chemical potential increases and becomes zero at some temperature T_c. Substituting $\mu = 0$ and $\epsilon_k = \hbar^2 k^2/2M$ one gets

$$n = 2.612 \left(\frac{M k_B T_c}{2\pi\hbar^2}\right)^{3/2}, \tag{1.8}$$

where we have used the formula $\int_0^\infty \frac{x^{a-1}}{e^x - 1} = \Gamma(a)\xi(a)$. Here $\xi(a)$ is the Riemann zeta function with $\xi(\frac{3}{2}) = 2.612$ and $\Gamma(\frac{3}{2}) = \frac{\sqrt{\pi}}{2}$. Now one can calculate the transition temperature for Bose-Einstein condensation (BEC). Which from Eq. (1.8) is

$$k_B T_c = \frac{3.31\hbar^2}{M} n^{2/3} \tag{1.9}$$

For $T < T_c$, a nonzero fraction of bosons condense into the lowest-energy state. Note that the particles with $\epsilon = 0$ do not contribute to the integral. For $T < T_c$, we can write a quantity called normal fraction as $\frac{N_{\epsilon>0}}{N} = \left(\frac{T}{T_c}\right)^{3/2}$. Thus the fraction of condensate atoms can be written as

$$\frac{N_{\epsilon=0}}{N} = 1 - \left(\frac{T}{T_c}\right)^{3/2}. \tag{1.10}$$

BEC occurs when quantum degeneracy sets in, i.e., when the thermal de Broglie length defined as $\lambda_{dB} = \frac{h}{\sqrt{2\pi M k_B T}}$ [33], of individual bosons begins to overlap. Using this expression for the de Broglie length in Eq. (1.8), the phase space density, ρ, of Bose gas at $T = T_c$ can be written as

$$\rho = n\lambda_{dB}^3 \simeq 2.612. \tag{1.11}$$

This shows that an ideal Bose gas undergoes BEC at a phase space density of 2.612 and that at the transition temperature, the thermal de Broglie length is on the order of the average interparticle distance. The condensation of an ideal Bose gas at constant volume is a third-order phase transition because the specific heat of an ideal Bose gas is continuous whereas its derivative is discontinuous.

1.3 Thesis organization

The work presented in this thesis is almost entirely releted to the atom-optical quantum kicked rotor (AOQKR) and closely related systems. The experimental study of the AOQKR has been made possible due to the existence of laser cooling and trapping and more recently BEC. Thus we begin Chapter 2 with an overview of the theory of this process and continue with a discussion of the magneto-optical trap (MOT) and evaporative cooling techniques. The realization of Bose-Einstein condensation is also discussed in this Chapter.

The classical $\delta-$kicked rotor model and its quantum analog using atom-optics is introduced in Chapter 3. A closely related model called the atom-optical $\delta-$kicked accelerator (AOQKA) is also discussed in this Chapter. Quantum resonances and anti-resonances are defined and the $\varepsilon-$ classical theory, that describes the dynamics of the system near these resonances is explained.

Chapter 4 details the experimental set up required to create a MOT and a BEC of ^{87}Rb including the imaging system, vacuum chamber and the alignment of the far off-resonant trap. From the day of its realization, the AOQKR has become the workhorse for the study of several quantum mechanical effects. The two applications of the AOQKR studied in this thesis are fidelity and the quantum ratchet effect. Fidelity, a relatively new concept for applying the AOQKR towards possible precision measurements of frequency and acceleration are the subject of discussion in Chapter 5. It is shown that the width of fidelity resonances scale at sub-Fourier rates with respect

to the measurement time. The sensitivity of the fidelity to an external acceleration is also studied. An in-depth discussion of fidelity of a quantum kicked accelerator is presented in Chapter 5.

It is shown that by creating an initial external atomic state which is a superposition of two momentum states and exposing it to a periodic potential, a non-dissipative transport of atoms known as a quantum ratchet can be produced. A purely quantum treatment of the ratchet effect at resonance and the experimental findings are presented in Chapter 6. The quantum ratchet effect is studied in a very general away and it is shown that it can be described by a classical treatment that depends on a single variable which encapsulates all of the important experimental parameters. The mean momentum is found to change direction without altering the underlying symmetry center of the system.

In Chapter 7 a brief review of $\varepsilon-$classical theory to explain quantum accelerator modes is presented. The decay of quantum accelerator modes is also discussed. Finally, the summary of the work in this thesis has been drawn and some of the future experiments are laid out in Chapter 8.

CHAPTER 2

Laser cooling and trapping

2.1 Preliminary concepts

The interaction of atoms with the light field of a laser can cause a force on atoms due to the scattering of photons. The average force is defined as the expectation value of the quantum mechanical force operator,

$$\hat{F} = -\nabla \hat{H}. \tag{2.1}$$

Where $\hat{H} = \hat{H}_0 + \hat{H}'(t)$ is the total Hamiltonian of the system with $\hat{H}_0$, the field-free time independent Hamiltonian and $\hat{H}'(t)$, the time dependent interaction Hamiltonian. The expectation value of $\hat{F}$ is given by,

$$\langle \hat{F} \rangle = \mathrm{Tr}(\hat{\rho}\hat{F}). \tag{2.2}$$

Where $\hat{\rho}$ is the density matrix and its time evolution is given by,

$$\frac{\mathrm{d}\hat{\rho}}{\mathrm{d}t} = -\frac{i}{\hbar}[\hat{H}, \hat{\rho}]. \tag{2.3}$$

Here the operator $\hat{H}_0$ has eigenvalues $E_n = \hbar\omega_n$ and eigenfunctions $\phi_n(\vec{r})$. Also the eigenfunctions are linearly independent forming a complete set. In order to calculate the force on the atoms by the laser field, a good starting point is the solution of the time dependent Schrödinger equation,

$$\hat{H}\psi(\vec{r}, t) = i\hbar\frac{\partial\psi(\vec{r}, t)}{\partial t}, \tag{2.4}$$

where the wavefunction $\psi(\vec{r}, t)$ can be expanded in terms of $\phi_n(\vec{r})$ as

$$\hat{H}(t)\psi(\vec{r}, t) = [\hat{H}_0 + \hat{H}'(t)] \sum_k c_k(t)\phi_k(\vec{r}) \tag{2.5}$$

Multiplying by $\phi_j^*(\vec{r})$ after applying Eq. (2.5) to Eq. (2.4) and integrating over spatial coordinates $\vec{r}$ one gets,

$$i\hbar\frac{\mathrm{d}c_j(t)}{\mathrm{d}t} = c_j(t)E_j + \sum_k c_k(t)\hat{H}'_{jk}(t), \tag{2.6}$$

where $\hat{H}'_{jk}(t) = \langle\phi_j|\hat{H}'(t)|\phi_k\rangle$. When considering a simple two state atom the problem is known as the Rabi two-level problem [34] and has just two coupled differential equations

$$i\hbar\frac{\mathrm{d}c_g(t)}{\mathrm{d}t} = c_g(t)(E_g + \hat{H}'_{gg}) + c_e(t)\hat{H}'_{ge}(t), \tag{2.7}$$

and

$$i\hbar\frac{\mathrm{d}c_e(t)}{\mathrm{d}t} = c_e(t)(E_e + \hat{H}'_{ee}) + c_g(t)\hat{H}'_{eg}(t). \tag{2.8}$$

The subscripts g and e refer to ground and excited states respectively and $\hat{H}'_{ge} = \hat{H}'^*_{eg}$. The interaction term is given by $\hat{H}'_{ge}(t) = -\vec{\mu}\cdot\vec{E}(\vec{r},t)$ [35] . Here $\vec{E}(\vec{r},t)$ is the electric field and $\vec{\mu} = q\langle e|\vec{r}|g\rangle$ is the induced dipole moment of the atom, where q is the electronic charge, and $\vec{r}$ is the position. Also due to the odd parity of $\hat{H}'$, only opposite parity atomic states can couple through the dipole interaction ($\hat{H}'_{ee}(t) = \hat{H}'_{gg}(t) = 0$) giving the final form of the Hamiltonian matrix as,

$$\hat{H} = \begin{pmatrix} 0 & -\vec{\mu}\cdot\vec{E}^*(\vec{r},t) \\ -\vec{\mu}\cdot\vec{E}(\vec{r},t) & \hbar\omega_e \end{pmatrix}. \tag{2.9}$$

Using Eq. (2.9) in Eq. (2.3) one can now calculate the time evolution of the density matrix which becomes

$$\begin{pmatrix} \dot{\rho}_{gg} & \dot{\rho}^*_{eg} \\ \dot{\rho}_{eg} & \dot{\rho}_{ee} \end{pmatrix} = i\begin{pmatrix} \Omega^*(\vec{r},t)\rho_{eg} - \Omega(\vec{r},t)\rho^*_{eg} & \omega_e\rho^*_{eg} - \Omega^*(\vec{r},t)u \\ -\omega_e\rho_{eg} + \Omega(\vec{r},t)u & -\Omega^*(\vec{r},t)\rho_{eg} + \Omega(\vec{r},t)\rho^*_{eg} \end{pmatrix}. \tag{2.10}$$

Where $\Omega(\vec{r},t) = \vec{\mu}\cdot\vec{E}(\vec{r},t)/\hbar$ is the Rabi frequency and $u = \rho_{gg} - \rho_{ee}$ is the population difference. For a closed two level system, the total population is conserved i.e., $\rho_{ee} + \rho_{gg} = 1$, and $\rho_{eg} = \rho^*_{ge}$. Then the optical Bloch equations can be written as [36]

$$\frac{\mathrm{d}\rho_{eg}(t)}{\mathrm{d}t} = -\frac{\gamma}{2}\rho_{eg} - i\omega_e\rho_{eg} + i\Omega(\vec{r},t)u \tag{2.11}$$

and

$$\frac{\mathrm{d}u}{\mathrm{d}t} = \gamma(1-u) + i\left(\Omega^*(\vec{r},t)\rho_{eg} - \Omega(\vec{r},t)\rho_{eg}^*\right). \tag{2.12}$$

Where the spontaneous emission rate is $\gamma = \frac{\omega_\ell^3 \mu^2}{3\pi\epsilon_0\hbar c^3}$, with ω_ℓ the laser frequency. The first term in the equations is introduced to account for the effect of spontaneous emission in the evolution of the density matrix. Let us write $\rho_{eg} = \sigma_{eg}e^{-i\omega_\ell t}$ and $\vec{E}(\vec{r},t) = \vec{E}(\vec{r})\cos(\omega_\ell t)$ then Eq. (2.11) and Eq. (2.12) reduce to

$$\frac{\mathrm{d}\sigma_{eg}}{\mathrm{d}t} = -(\gamma/2 - i\delta)\sigma_{eg} + \frac{iu\Omega^*(\vec{r})}{2} \tag{2.13}$$

and

$$\frac{\mathrm{d}u}{\mathrm{d}t} = \gamma(1-u) + i\left(\Omega^*(\vec{r})\sigma_{eg} - \Omega(\vec{r})\sigma_{eg}^*\right). \tag{2.14}$$

Where the rotating wave approximation is used (we ignore the terms with high frequencies ($2\omega_\ell$) because they average to zero) and $\delta = \omega_\ell - \omega_e$ is the laser frequency detuning from the atomic transition. The steady state solutions of Eq. (2.13) and Eq. (2.14) are

$$\sigma_{eg} = \frac{2\Omega\left(-\delta + i\frac{\gamma}{2}\right)}{\gamma^2\left[1 + \left(\frac{2\delta}{\gamma}\right)^2 + 2\frac{\Omega^2}{\gamma^2}\right]} \tag{2.15}$$

and

$$u = \frac{1 + \left(\frac{2\delta}{\gamma}\right)^2}{\left[1 + \left(\frac{2\delta}{\gamma}\right)^2 + 4\frac{\Omega^2}{\gamma^2}\right]} \tag{2.16}$$

where $\Omega = \vec{\mu}\cdot\vec{E}(\vec{r})/\hbar$ is the Rabi frequency. Using the conservation of total population, we can explicitly calculate ρ_{gg} and ρ_{ee} and thus the force operator. For a special case, where electric field is produced by a traveling wave propagating in $z-$direction, $E(z) = E_0\cos(kz - \omega_\ell t)$, the force operator can be written as

$$\hat{F} = \begin{pmatrix} 0 & \mu\frac{\partial E^*(z)}{\partial z} \\ \mu\frac{\partial E(z)}{\partial z} & 0 \end{pmatrix}. \tag{2.17}$$

Now Eq. (2.2) can be rewritten as,

$$\langle\hat{F}\rangle = \mathrm{Tr}(\hat{\rho}\hat{F}) = \mu\frac{\partial E}{\partial z}\sigma_{eg}^* e^{i\omega_\ell t} + \mu\frac{\partial E^*}{\partial z}\sigma_{eg}e^{-i\omega_\ell t}, \tag{2.18}$$

after substituting Eq. (2.15) in Eq. (2.18), the force on a stationary atom is

$$F = \frac{\hbar k \gamma s}{2\left[1 + \left(\frac{2\delta}{\gamma}\right)^2 + s\right]}, \tag{2.19}$$

where $s = \frac{2\Omega^2}{\gamma^2}$, is the saturation parameter. It is also defined as $s = I/I_s$, where I and $I_s = \frac{\pi hc}{3\lambda^3 \tau}$, and τ the upper state life time, are the laser light intensity and saturation intensity respectively. Now we can extend this result to an atom moving with velocity v. An atom moving with velocity v will see a Doppler shift of $\pm kv$ in the laser frequency. Where the plus (minus) sign refers to an atom moving in the opposite (same) direction to the laser beam. Thus an atom sees the laser frequency detuned by $\delta \pm kv$ and the force on a moving atom is given by

$$F = \pm \frac{\hbar k \gamma s}{2\left[1 + \left(\frac{2(\delta \mp kv)}{\gamma}\right)^2 + s\right]}. \tag{2.20}$$

Where the plus (minus) refers to the force experienced by an atom moving along (opposite) the direction of light field. Let us consider the case of an atom interacting with two counter propagating beams in $z-$direction, then the total force on an atom will be

$$F = \frac{\hbar k \gamma s}{2\left[1 + \left(\frac{2(\delta - kv)}{\gamma}\right)^2 + s\right]} - \frac{\hbar k \gamma s}{2\left[1 + \left(\frac{2(\delta + kv)}{\gamma}\right)^2 + s\right]}. \tag{2.21}$$

In the limit of Doppler shift small compared to δ, the above equation results in a velocity dependent force $F = -\beta v$, where β is a damping coefficient given by

$$\beta = \frac{8\hbar k^2 s \delta}{\gamma\left[\left(1 + \left(\frac{2\delta}{\gamma}\right)^2 + s\right)\right]^2}. \tag{2.22}$$

This equation can be interpreted as follows: With a laser light frequency detuned below the atomic resonant frequency i.e., $\delta < 0$, atoms traveling towards the laser beam see the light Doppler shifted closer to resonance where as atoms moving in the same direction to that of laser beam see the light Doppler shifted further away from

the resonance. Thus atoms scatter more photons from the beam counter propagating to their velocity resulting in a decreasing velocity. This is a damping mechanism called optical molasses. By using three pairs of counter propagating beams in three orthogonal directions the atoms will feel a damping force in three dimensions no matter what the direction of the atom's motion. Note that this is a velocity dependent force and is therefore non-conservative. This force from the counter propagating laser beams with a frequency detuned below the atomic resonant frequency is one of the basic tools of laser cooling. The experimental implementation of this theory to cool atoms was first done by Chu and co-worker [37].

2.2 Limits of laser cooling

With a purely damping force as described in the previous section, one may think that the atomic velocity can be reduced without any limitations. However there is a lowest temperature that can be obtained in an optical molasses because of recoil heating. Due to the random nature of the photon scattering process, this causes a diffusion of atoms in momentum space and atoms are heated. A steady state is reached when the molasses cooling rate equal the recoil heating rate. This determines the limiting temperature called the Doppler temperature, T_D, which is given by

$$T_D = \frac{\hbar\gamma}{2k_B}, \tag{2.23}$$

where k_B is the Boltzman constant and γ is the natural line width. For ^{87}Rb the Doppler temperature is 146μK. However, surprisingly, in one of the early experiments [38], a lower temperature than the Doppler temperature was observed. W. Phillips and co-workers revealed that the multiple levels that were not considered in the simple two level treatment were playing a role to produce this sub-Doppler cooling [39, 40]. The theory of this cooling, which is also known as the polarization gradient cooling since the origin of the cooling is the gradient in polarization, was then developed by

Cohen Tanoudji [41]. The next limit to the laser cooling temperature is determined by the energy associated with a single photon recoil, $E_r = \frac{\hbar^2 k^2}{2m}$. The limit of the temperature by this process is.

$$T_r = \frac{\hbar^2 k^2}{m k_B}. \tag{2.24}$$

For ^{87}Rb, the recoil limit has a value of 360nK.

2.3 Magneto-Optical Trap

Magneto-optical trapping is the most popular approach for trapping neutral atoms and employs both optical and magnetic fields. It was first demonstrated in 1987 [21]. The operation of a magneto-optical trap (MOT) depends on both an inhomogeneous magnetic field and an appropriate arrangement of near-resonant laser beams. The MOT is a very robust trap because it neither depends on precise balance nor high degrees of polarization of the counterpropagating laser beams. In order to understand the operation of the MOT, let us consider an atomic transition with a simple scheme $J_g = 0 \rightarrow J_e = 1$ subjected to a linearly inhomogeneous magnetic field $B = B(z) = B_0 z$. This magnetic field splits the excited state into three Zeeman components $M_e = -1$, 0, and $+1$ as shown in Fig. 2.1. Adding two counterpropagating laser beams of opposite circular polarization, each detuned below the zero field atomic transition completes the requirement to create a MOT.

Because of the Zeeman shift for $B > 0$, the excited states $M_e = +1$ is shifted up and $M_e = -1$ is shifted down. The shift of $M_e = \pm 1$ is reversed for $B < 0$. Thus at a position z' in Fig. 2.1, the magnetic field tunes the $\Delta M = -1$ transition closer to the resonance and the $\Delta M = +1$ transition further away from the transition. If the polarization of the laser beam incident from the right is chosen to be σ_- and correspondingly σ_+ for the beam incident from left, then the atoms scatter more light from the σ_- beam than from the σ_+ beam. Thus the atoms are driven towards the center of the trap where the magnetic field is zero. On the other side of the center

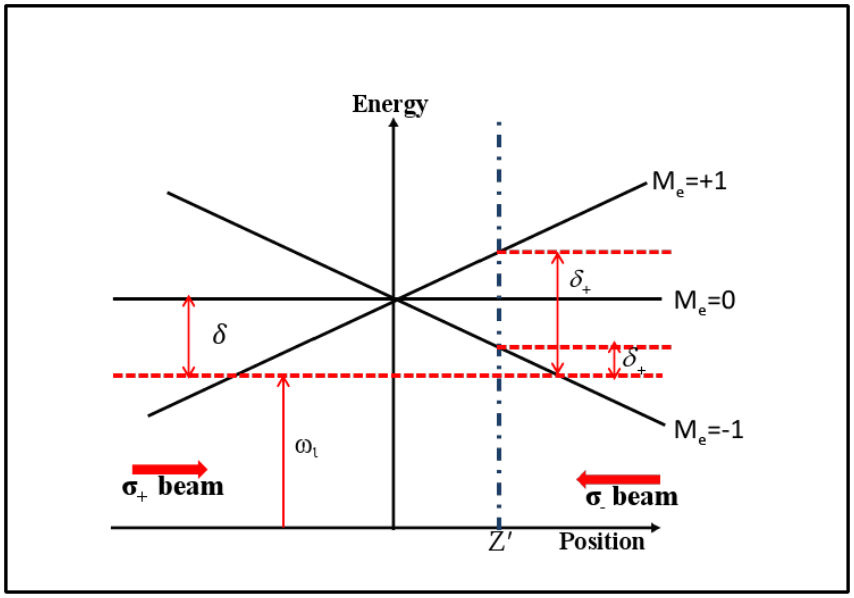

Figure 2.1: Arrangement for a MOT. Three Zeeman components of the excited state of atoms in the $J_g = 0 \rightarrow J_e = 1$ schemes are represented by $M_e = -1$, 0, and $+1$. Two oppositely circular polarized beams are incident from left (σ_+) and right (σ_-). At $z = z'$, atoms are closer to resonance with the σ_- beam than with the σ_+ beam, and are therefore driven toward the center of the trap.

of the trap, the magnetic field tunes the $\Delta M = +1$ transition closer to the resonance hence the atoms scatter more light from the σ_+ beam driving the atoms towards the center of the trap. In the optical molasses, the damping force due to Doppler effect operates in the velocity space whereas in this situation it operates in position space. Thus by using the laser light with a frequency detuned below the resonance in conjuction with the B-field gradient, compression and cooling of the atoms is obtained simultaneously. A 3D extension of a MOT scheme can be implemented by using three pairs of counterpropagating laser beams in three orthogonal directions. The detuning of each laser beam in the presence of the magnetic field is given by

$$\delta_\pm = \delta \mp \vec{k}.\vec{v} \pm \mu' \mathrm{B}/\hbar. \tag{2.25}$$

Where the effective magnetic moment is $\mu' = \mu_B(g_e M_e - g_g M_g)$, with μ_B the Bohr magneton and g the Lande$^{'}$ g-factor. Thus the total force on the atom is

$$F_\pm = \pm \frac{\hbar \vec{k} \gamma}{2} \frac{s_0}{1 + s_0 + (2\delta_\pm/\gamma)^2)}, \tag{2.26}$$

where $s_0 = 2|\Omega|^2/\gamma^2 = I/I_s$.

2.4 Evaporative cooling

In order to observe the BEC transition, the phase space densities, $\rho = n\lambda_{dB}^3$, should be greater than 2.612 [42], where n is the density and λ_{dB} is the thermal de Broglie wavelength of the atom [33]. For ordinary gases at room temperature and pressure, $\rho \sim 10^{-6}$ and for an atomic beam $\rho \sim 10^{-10}$. In the early days of laser cooling there was a great hope that this technique could be used to cool the atoms with out any limitations. However due to the limitation in temperature imposed by recoil heating as described in the previous section, the maximum achievable phase space density with laser cooling is about 10^{-5}–10^{-4}. With laser cooling, one can obtain μK temperatures with very little loss of atoms, thus increasing the density of the

atomic gas. However the increase in density leads to an increase in the collision rate between atoms with one in the excited state (S+P collision). Since this collision is inelastic, the energy exchange leads to a heating effect on the atoms. Therefore near-resonant light should be avoided in order to achieve BEC, and thus laser cooling alone is not the most likely route for achieving BEC. Physicists soon made a breakthrough on overcoming this problem realizing that evaporative cooling would be a way to increase the phase space density further [43–45]. Harald Hess [43] originally proposed this idea for atomic hydrogen. His idea was based on the preferential removal of atoms with energy higher than the average from a trap, followed by rethermalization of the remaining atoms by elastic collisions. Since both the temperature and volume decrease, the phase space density can increase. In 1994 this idea was extended to alkali atoms by combining evaporative cooling with laser cooling [22].

For evaporative cooling of atoms, magnetic fields or far-off-resonant optical fields have been used. The later has been used in Summy's lab and will be described here. A far off-resonant trap (FORT) is based on the fact that an off-resonant laser creates a potential which is attractive or repulsive depending on whether it is red or blue detuned from an atomic transitions. The depth of the trap depends approximately on the laser intensity I divided by the detuning δ_ℓ ($U \approx \hbar I/4\delta_\ell$) whereas the spontaneous scattering rate depends on intensity divided by the square of the detuning ($\gamma \approx \Gamma I/4\delta_\ell^2$, where Γ is the spontaneous-emission rate of atom) [46]. Thus the advantage of a large detuning is that the same potential well depth can be achieved with a reduced scatter rate.

Several models for the evaporating cooling process have been developed [47–51]. A simple but instructive model is due to Davis *et al.* [49] and will be reviewed here. In this model, the trap depth is lowered in one single step to a finite energy $\eta k_B T$, the atoms then thermalize by collisions and the effect on the thermodynamical quantities such as the volume, the density, and the temperature are finally calculated. The

fraction of atoms remaining in the trap after cooling is given by $\nu = N'/N$ and the decrease in temperature of the remaining atoms due to removal of hot atoms is measured by a quantity, γ (not the natural linewidth), as

$$\gamma = \frac{\log(T'/T)}{\log \nu}. \tag{2.27}$$

Here the primed quantities refer to values after the cooling process. Thus we have the scaling of important thermodynamical quantities, $N' = N\nu$, $T' = T\nu^{\gamma}$, and $V' = V\nu^{\gamma\xi}$ [36], where the quantity ξ characterizes the type of potential. For example, for a linear potential like a spherical quadrupole trap, $\xi = 3$ and for a harmonic potential as in an optical trap, $\xi = 3/2$. The phase space density scales as $\rho' = \rho\nu^{1-\gamma(\xi+3/2)}$ and the collision rate scales as $k' = k^{1-\gamma(\xi-1/2)}$. Thus with the help of the parameters such as ξ, ν, and γ for a given value of η, the evolution of all thermodynamical quantities can be determined. The density of states for the atoms in a trapping potential $U(x, y, z)$ is given by [52],

$$D(E) = \frac{2\pi(2M)^{3/2}}{\hbar^3} \int_V \sqrt{E - U(x, y, z)} \mathrm{d}^3 r \tag{2.28}$$

and the fraction of atoms in the trap after lowering the trap depth to $\eta k_B T$ is

$$\nu = \frac{1}{N} \int_0^{\eta k_B T} D(E) e^{-(E-\mu)/k_B T} \mathrm{d}E, \tag{2.29}$$

where μ is the chemical potential and the occupancy number is given by the Maxwell-Boltzman distribution. Defining the reduced energy as $\epsilon = E/k_B T$ and the reduced density of states as $\Delta(\epsilon) = \frac{\epsilon^{\xi+1/2}}{\Gamma(\xi+3/2)}$, where $\Gamma(x)$ is a gamma function, Eq. (2.29) can be written as [36],

$$\nu = \int_0^{\eta} \Delta(\epsilon) e^{-\epsilon} \mathrm{d}\epsilon. \tag{2.30}$$

The total energy of the atoms after truncation is $\alpha(\eta) N k_B T$ where

$$\alpha(\eta) = \int_0^{\eta} \epsilon \Delta(\epsilon) e^{-\epsilon} \mathrm{d}\epsilon. \tag{2.31}$$

Therefore the average total energy per atom in units of $k_B T$ is $\alpha(\eta)/\nu(\eta)$. When $\eta \to \infty$, this quantity is $\alpha(\infty)/\nu(\infty) = (3/2 + \xi)/1$ and the ratio of the temperature

is given by,

$$\frac{T'}{T} = \frac{\alpha(\eta)/\nu(\eta)}{\alpha(\infty)/\nu(\infty)}. \tag{2.32}$$

Thus the quantity γ in Eq. (2.27) can be written as

$$\gamma = \frac{\log\left[\frac{\alpha(\eta)}{\nu(\eta)\alpha(\infty)}\right]}{\log[\nu(\eta)]}. \tag{2.33}$$

This quantity measures the excess energy above average energy that has been carried away by the evaporated atoms. For a specific type of potential one can determine the value of γ. For example, for a harmonic trap: $\xi = 3/2$,

$$\nu(\eta) = \frac{1}{\Gamma(3)}\int_0^\eta \epsilon^2 e^{-\epsilon}\mathrm{d}\epsilon = 1 - \frac{2+2\eta+\eta^2}{2e^\eta},$$

and

$$\alpha(\eta) = \frac{1}{\Gamma(3)}\int_0^\eta \epsilon^3 e^{-\epsilon}\mathrm{d}\epsilon = 3 - \frac{6+6\eta+3\eta^2+\eta^3}{2e^\eta}.$$

Where $\Gamma(n) = (n-1)!$ and $\int u(x)v(x)\mathrm{d}x = u\int v dx - \int u'(\int v\mathrm{d}x)\mathrm{d}x$ have been used. Here it can be seen that for larger ξ, higher phase space density is achieved due to the faster shrinking of the volume with decreasing temperature ($T \propto V^\xi$). In addition, this increases the rate of elastic collisions and consequently the rethermalization process, thus speeding up the cooling process.

CHAPTER 3

The Atom-Optics Quantum Delta Kicked Rotor and Accelerator

Understanding the nature of the crossover between classical and quantum behavior is one of the most important unresolved problems in physics. One place where the stark difference between the two paradigms becomes very clear is in classical non-linear systems. Classically, such a system can exhibit chaos in which it is effectively impossible to predict its long term evolution, while in contrast because of the linearity of the Schrödinger equation, an equivalent quantum mechanical systems is completely deterministic. One of the systems of choice for studying this behavior is the so-called delta-kicked rotor, typically realized with a sample of cold or ultra-cold atoms kicked by short pulses of an optical standing wave. While theory and experiment has been successful in elucidating some features of this and similar systems, there are still many aspects that remain to be discovered.

Ever since the realization of the atom optics quantum kicked rotor (AOQKR) [53, 54], it has been one of the workhorses for studies of experimental quantum chaos. It has revealed a wide variety of interesting effects including: dynamical localization [55, 56], quantum resonances (QR) [55, 57–59], and quantum ratchets [60–67]. A closely related system, the quantum delta kicked accelerator (QDKA), differs from the usual QDKR by adding a linear potential in the form of an acceleration. The QDKA has been used in studying aspects of the transition to chaos in both classical and quantum regimes [68], and is a system in which quantum accelerator modes [69–74] are observed. In this chapter we will discuss the classical kicked rotor system and its quantum analog the AOQKR as well as the closely related QDKA.

3.1 The classical $\delta-$kicked rotor

The classical kicked rotor is defined as a particle of mass M with linear momentum $\vec{p}$, constrained to move in a circle of radius R, which is exposed to a periodic constant force referred as kicks as shown in Fig. 3.1. The effect of a kick depends sinusoidally on the azimuthal angular displacement θ. The kicked rotor is described by a Hamiltonian [75]

$$H = \frac{J'^2}{2I} + V_0 \cos(\theta) \sum_q \delta(t - qT). \tag{3.1}$$

Where $J' = |\vec{J'}| = |\vec{R} \times \vec{p}|$ is the angular momentum and $I = MR^2$ is the moment of inertia. The time-evolution of the canonically conjugate position and momentum variables are given by Hamilton's equations of motion

$$\dot{\theta} = \frac{\partial H}{\partial J'} = \frac{J'}{I} \tag{3.2}$$

$$\dot{J'} = -\frac{\partial H}{\partial \theta} = V_0 \sin(\theta) \sum_q \delta(t - qT). \tag{3.3}$$

Now we evaluate the evolution over one period between $t = q$ and $t = q + 1$ by integrating Eqns. (3.2) and (3.3). This becomes

$$\int_{qT}^{(q+1)T} \dot{\theta} \mathrm{d}t = \theta_{q+1} - \theta_q = \frac{J'_{q+1}}{I} T \tag{3.4}$$

$$\int_{qT}^{(q+1)T} \dot{J'} \mathrm{d}t = J'_{q+1} - J'_q = V_0 \sin\theta_q. \tag{3.5}$$

Using the rescaled variables $J = J'T/I$ and $K = TV_0/I$, we obtain the Chirikov-Taylor standard map [75, 76]

$$\theta_{q+1} = \theta_q + J_{q+1} \tag{3.6}$$

$$J_{q+1} = J_q + K \sin\theta_q. \tag{3.7}$$

This map describes the dynamics of a kicked rotor by a single variable K, known as the stochasticity parameter. A stable trajectory characterized by closed curves dominates the phase space (θ, J') plot for small values of K, whereas the chaotic

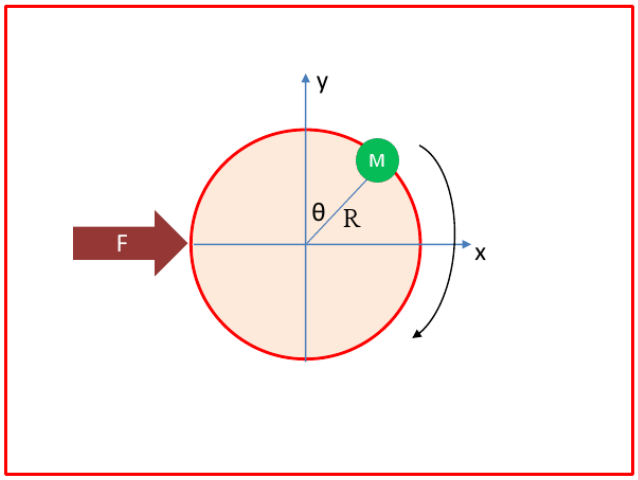

Figure 3.1: The classical $\delta-$kicked rotor. A particle of mass M is constrained to move on a circle of radius R and is subjected to periodic pulses of force $\vec{F}$.

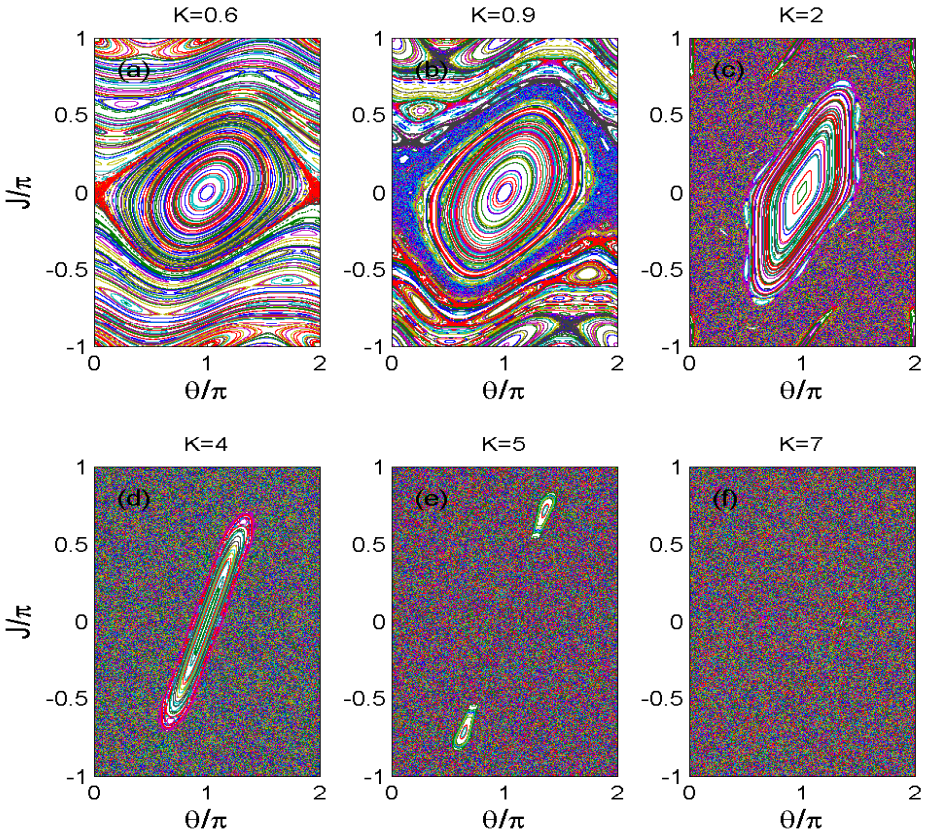

Figure 3.2: Phase space plot of the classical $\delta-$kicked rotor for different values of K. Note that the chaotic region dominates for higher values of K.

region dominates for large values of K as shown in Fig. 3.2. The transition from stability to global chaos is predicted to occur for $K = 0.971635$ [77, 78].

3.2 The quantum $\delta-$kicked rotor

While Rydberg atoms provided the first insights into the quantum version of the $\delta-$kicked rotor, most of the work on this system has been reformed using atom optics. Such a system is realized by exposing a collection of atoms to short, periodic pulses of far-detuned optical standing wave. The quantum $\delta-$kicked rotor can be described by the Hamiltonian

$$H = \frac{\hat{P}^2}{2M} + \hbar\phi_d \cos(G\hat{X}) \sum_{q=0}^{\mathrm{t}} \delta(t - qT). \tag{3.8}$$

Where $\hat{P}$ is the momentum, $\hat{X}$ is the position, $G = 2\pi/\lambda_G$ is the grating wave vector with λ_G the spatial period of the standing wave. Other quantities are $\phi_d = \frac{\Omega^2 \Delta t}{8\delta_L}$, the strength of the kick (phase modulation depth), t , the continuous time variable (integer units), and q, the number of kicks with period T. Where Ω is the Rabi frequency between the ground and excited state, Δt is the length of a pulse and δ_L is the detuning of the laser frequency from the atomic transition.

It is convenient to write the above Hamiltonian in dimensionless units. Let us define the momentum in units of two photon recoils, $\hbar G$, i.e., $\hat{p} = \hat{P}/\hbar G$, the position in units of spatial period of the standing wave i.e., $\hat{x} = G\hat{X}$. The scaled pulse period is written as $\tau = 2\pi T/T_{1/2}$, where $T_{1/2}$ is a characteristic time called half-Talbot time which is defined as

$$T_{1/2} = \frac{2\pi M}{\hbar G^2}. \tag{3.9}$$

Now the Hamiltonian in dimensionless unit can be written as

$$\mathcal{H} = \frac{\hat{p}^2}{2} + \phi_d \cos(\hat{x}) \sum_{q=1}^{\mathrm{t}} \delta(t' - q\tau). \tag{3.10}$$

Where $\mathcal{H} = \frac{H}{(\hbar^2 G^2/M)}$ and $t' = \frac{2\pi t}{T_{1/2}}$. Also an identity $\sum \delta(Ax) = \frac{1}{A}\sum \delta(x)$ is used. It is convenient to write the momentum into discrete and continuous components as $p = n + \beta$ with n, the integer part and β, the fractional part also called quasi-momentum. Since the potential is periodic with spatial period of $2\pi/G$, only the transitions between the momenta that differ by integer multiples of two photon recoils, $\hbar G$ are allowed. The periodicity of the potential allows the connection between a particle and the kicked rotor where the position of the particle can be folded into an angular coordinate $\theta = x \mod 2\pi$. The solutions are invariant under the translation of the wave function by one period of the potential and hence by the Bloch theorem [10] the quasi-momentum is conserved. The dynamics of the rotor are then described by a one-period evolution operator called the Floquet operator, given by

$$\hat{\mathcal{U}} = e^{-i\phi_d \cos\hat{\theta}} e^{-i\hat{p}^2 \frac{\tau}{2}}. \tag{3.11}$$

3.2.1 Quantum resonance and anti-resonance

The evolution of the wave function from one kick to immediately after the next kick is given by the Floquet operator which is written as

$$\begin{aligned} \hat{F} &= \hat{U}_{\text{kick}} \hat{U}_{\text{free}} \\ &= e^{-i\phi_d \cos(\hat{x})} e^{-i\frac{\hat{p}^2}{2}\tau} \end{aligned} \tag{3.12}$$

and the wave function after t kicks is then given by

$$|\psi(\mathrm{t}\tau)\rangle = \hat{U}^{\mathrm{t}} |\psi(0)\rangle. \tag{3.13}$$

When the kicking period τ is an integer multiple of 4π, this corresponds to the Talbot time [79, 80] defined as $T_T = \frac{4\pi M}{\hbar G^2}$. In this case the free evolution operator will be unity and the effect of all the kicks add coherently which is equivalent to a single kick of strength $\mathrm{t}\phi_d$. This is a quantum resonance and the Floquet operator takes the form

$$\hat{F} = \hat{U}^{\mathrm{t}}_{\text{kick}} = e^{-i\mathrm{t}\phi_d \cos(\hat{x})}. \tag{3.14}$$

Assuming an initial momentum state $|0\rangle$, the probability for a momentum state $|n\rangle$ to be populated in the final state after t kicks is given by

$$\begin{aligned} P_n &= |\langle n|\hat{U}^{\mathrm{t}}|0\rangle|^2 \\ &= |\langle n|e^{-i\mathrm{t}\phi_d\cos(\hat{x})}|0\rangle|^2 \\ &= J_n^2(\mathrm{t}\phi_d). \end{aligned} \tag{3.15}$$

Where the Jacobi-Anger relation, $e^{iz\cos x} = \sum_{n=-\infty}^{\infty} i^n J_n(z)e^{inx}$, is used. Then the mean energy of the ensemble at the end of t^{th} kick is given by

$$\begin{aligned} \langle E\rangle &= \sum_{n=-\infty}^{\infty} n^2 P_n \\ &= \sum_{n=-\infty}^{\infty} n^2 J_n^2(\mathrm{t}\phi_d) \\ &= \frac{1}{2}\mathrm{t}^2\phi_d^2. \end{aligned} \tag{3.16}$$

Which shows that for a kicked rotor starting from the zero momentum state, the mean energy grows quadratically in time, a characteristic of the quantum resonance.

Now we consider the evolution dynamics of a kicked rotor with a kicking period equal to the half-Talbot time $T_{1/2}$ i.e., $\tau = 2\pi$ or any odd multiple of 2π. The wave function after a one-period evolution can be written as

$$\begin{aligned} |\psi(\tau = T_{1/2})\rangle &= e^{-i\phi_d\cos(\hat{x})}e^{-i\frac{\hat{p}^2}{2}\tau}|\psi(0)\rangle. \\ &= \sum_{n=-\infty}^{\infty}(-i)^n J_n(\phi_d)e^{-i\pi n^2}e^{-in\hat{x}}|\psi(0)\rangle \\ &= \sum_{n=-\infty}^{\infty}(i)^n J_n(\phi_d)e^{-in\hat{x}}|\psi(0)\rangle \\ &= \sum_{n=-\infty}^{\infty}(i)^{-n} J_{-n}(\phi_d)e^{in\hat{x}}|\psi(0)\rangle \\ &= \sum_{n=-\infty}^{\infty}(i)^n J_n(\phi_d)e^{in\hat{x}}|\psi(0)\rangle \\ &= e^{i\phi_d\cos\hat{x}}|\psi(0)\rangle \end{aligned} \tag{3.17}$$

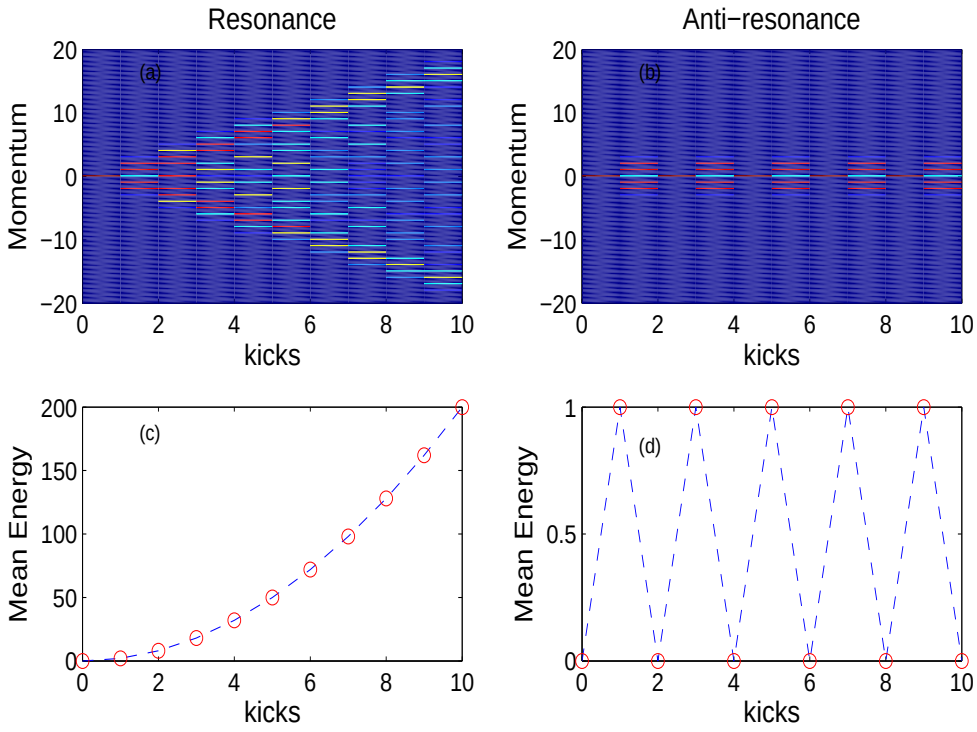

Figure 3.3: Momentum distribution as a function of kick number at (a) quantum resonance and (b) anti-resonance with $\phi_d = 2$. A quadratic growth in mean energy at a quantum resonance (Talbot time) and an oscillatory mean energy at an anti-resonance (half-Talbot time) can be seen in (c) and (d) respectively.

Where the Bessel function property, $J_{-n}(x) = (-1)^n J_n(x)$, is used. Equation (3.17) shows that when the kicking period is an odd multiple of 2π, the phase evolution between kicks changes the sign and results in a re-image of the grating transmission function which is inverse to the previous one. Thus the effect is that two kicks with a period equal to half the Talbot time cancel each other, recreating the original state and thus the mean energy will be oscillatory. This is called quantum anti-resonance. In general the resonance condition can be described in terms of scaled pulse period as

$$\tau = 2\pi\ell, \tag{3.18}$$

where ℓ is integer and even (odd) values of ℓ correspond to resonance (anti-resonance). Figure 3.3 shows a numerical simulation beginning with a zero momentum initial state for (a) quantum resonance and (b) anti-resonance along with the quadratic growth in mean energy with time in resonance (c) and oscillatory behavior of mean energy at quantum anti-resonance (d).

3.3 The $\delta-$kicked accelerator

3.3.1 The Hamiltonian

The dynamics of an atom of mass M subjected to pulses of sinusoidal potential with temporal period, T, in the presence of an external acceleration, g', is described by

$$H = \frac{\hat{P}^2}{2M} + Mg'\hat{X} + \hbar\phi_d \cos(G\hat{X}) \sum_{q=0}^{\mathrm{t}} \delta(t - qT), \tag{3.19}$$

which differs from Eq. (3.8) by an extra second term where g' is the acceleration of the atoms relative to the standing wave. By defining $\eta = \frac{Mg'T}{\hbar G}$, a dimensionless acceleration parameter, the Hamiltonian of a QDKA takes the form

$$\mathcal{H} = \frac{\hat{p}^2}{2} + \frac{\eta}{\tau}\hat{x} + \phi_d \cos(\hat{x}) \sum_{q=1}^{\mathrm{t}} \delta(t' - q\tau). \tag{3.20}$$

In the presence of acceleration the potential is not periodic and hence the quasi-momentum is not conserved anymore. However the spatial periodicity of the potential and hence the conservation of quasi-momentum can be restored by writing the above Hamiltonian in a non-accelerating frame (moving to a frame co-moving with the acceleration).

3.3.2 Hamiltonian in the non-accelerating frame

In the non-accelerating frame, the Hamiltonian after a gauge transformation will become

$$\mathcal{H}(t') = \frac{1}{2}\left(\hat{P} - \frac{\eta t'}{\tau}\right)^2 + \phi_d \cos(\hat{x}) \sum_{q=1}^{\mathrm{t}} \delta(t' - q\tau) \tag{3.21}$$

which is periodic in space and hence the quasi-momentum is conserved. Decomposing $p = n + \beta$, where n and β are the integer and fractional part of the momentum p respectively. Since the quasi-momentum β is conserved the evolution dynamics are equivalent to that of an independent $\beta-$ rotor, characterized by a particular value of β. The one-step evolution operator becomes

$$\mathcal{U}_\beta(q) = e^{\left(-i\phi_d \cos\hat{\theta}\right)} e^{-i\frac{\tau}{2}\left(\hat{N}+\beta-\eta q-\eta/2\right)^2}. \tag{3.22}$$

Where $\theta = x \mathrm{mod}(2\pi)$ and $\hat{N} = -i\frac{\mathrm{d}}{\mathrm{d}\theta}$ is the momentum operator which gives the integer eigenvalues n. For $\eta = \beta = 0$, the above expression reduces to usual kicked rotor.

3.3.3 $\varepsilon-$classical theory

We are interested in the case close to resonance such that $\tau = 2\pi\ell + \varepsilon$ with $|\varepsilon| \ll 1$. We simplify Eq. (3.22) by substituting $\alpha = \beta - \eta q - \eta/2$, which then becomes

$$\begin{aligned}
\mathcal{U}_\beta(q) &= e^{\left(-i\phi_d \cos\hat{\theta}\right)} e^{\left[-i\frac{\tau}{2}(n+\alpha)^2\right]} \\
&= e^{\left(-i\phi_d \cos\hat{\theta}\right)} e^{\left[-i\frac{2\pi\ell+\varepsilon}{2}(n^2+2n\alpha+\alpha^2)\right]} \\
&= e^{\left(-i\phi_d \cos\hat{\theta}\right)} e^{\left[-i\pi\ell n - i(2\pi\ell+\varepsilon)n\alpha - i\frac{\varepsilon}{2}n^2 - i\frac{\tau}{2}\alpha^2\right]} \\
&= e^{\left(-i\phi_d \cos\hat{\theta}\right)} e^{\left[-i\frac{\varepsilon}{2}n^2 - in(\pi\ell+\tau\alpha)\right]} \\
\hat{\mathcal{U}}_\beta(q) &= e^{\left(-i\phi_d \cos\hat{\theta}\right)} e^{\left[-i\frac{\varepsilon}{2}\hat{N}^2 - i\hat{N}(\pi\ell+\tau(\beta-\eta q-\eta/2))\right]}.
\end{aligned} \tag{3.23}$$

In the third step, an identity $e^{-i\pi\ell n^2} = e^{-i\pi\ell n}$ is used and an irrelevant phase factor is dropped. Let us define the scaling variables $\hat{I} = |\epsilon|\hat{N}$ and $\tilde{k} = \phi_d|\epsilon|$ so that the evolution operator takes the form

$$\begin{aligned}
\hat{\mathcal{U}}_\beta(q) &= e^{\left(-i\frac{\tilde{k}}{|\varepsilon|}\cos\hat{\theta}\right)} e^{\left[-i\frac{\varepsilon}{2}\left(\frac{\hat{I}}{|\varepsilon|}\right)^2 - i\frac{\hat{I}}{\varepsilon}(\pi\ell+\tau(\beta-\eta q-\eta/2))\right]} \\
&= e^{\left(-i\frac{\tilde{k}}{|\varepsilon|}\cos\hat{\theta}\right)} e^{\left[-\frac{i}{2|\varepsilon|}\mathrm{sign}(\varepsilon)\hat{I}^2 - i\frac{\hat{I}}{|\epsilon|}(\pi\ell+\tau(\beta-\eta q-\eta/2))\right]} \\
&= e^{\left(-i\frac{\tilde{k}}{|\varepsilon|}\cos\hat{\theta}\right)} e^{\left[-\frac{i}{|\varepsilon|}\hat{\mathcal{H}}_\beta(\hat{I},q)\right]}.
\end{aligned} \tag{3.24}$$

Where

$$\hat{\mathcal{H}}_\beta(\hat{I},q) = \frac{1}{2}\mathrm{sign}(\varepsilon)\hat{I}^2 + \hat{I}\left(\pi\ell + \tau(\beta - \eta q - \eta/2)\right). \tag{3.25}$$

From the above operator, we can deduce the Hamiltonian from the general evolution relation

$$\hat{\mathcal{U}} = e^{\left(-\frac{i}{\hbar}\int \hat{\mathcal{H}}(t)\mathrm{d}t\right)}. \tag{3.26}$$

If $|\varepsilon|$ is assigned the role of Planck's constant we can write the Hamiltonian as

$$\hat{\mathcal{H}} = \frac{1}{2}\mathrm{sign}(\varepsilon)\hat{I}^2 + \hat{I}\left(\pi\ell + \tau(\beta - \eta q - \eta/2)\right) + \tilde{k}\cos(\hat{\theta})\sum_{q=0}^{\mathrm{t}}\delta(t'-q). \tag{3.27}$$

Let us now write Hamilton's equations of motion usin Eq. (3.27)

$$\dot{I} = -\frac{\partial \mathcal{H}}{\partial \theta} = \tilde{k}\sin(\theta)\sum_q \delta(t'-q), \tag{3.28}$$

$$\dot{\theta} = \frac{\partial \mathcal{H}}{\partial I} = \text{sign}(\varepsilon)I + \pi\ell + \tau(\beta - \eta q - \eta/2). \tag{3.29}$$

The above equations are now integrated from a time just before the kick q at $t' = q\tau$ to just before the subsequent kick $q+1$ at $t' = (q+1)\tau$ so that the kick at $q+1$ does not contribute to the integral. Thus the integrals describe the dynamics due to a kick which is on for infinitesimally short time $\Delta t(\Delta t \to 0)$, followed by a period of free evolution. The evolution dynamics will be described by a map obtained after solving the following integrals:

$$\begin{aligned}
\int_{q\tau^-}^{(q+1)\tau^-} \dot{\theta}\mathrm{d}t' &= \int_{q\tau^-}^{(q\tau^-+\Delta t)} \dot{\theta}\mathrm{d}t' + \int_{q\tau^-+\Delta t}^{(q+1)\tau^-} \dot{\theta}\mathrm{d}t' \\
\theta_{q+1} - \theta_q &= 0 + \int_{q\tau^-+\Delta t}^{(q+1)\tau^-} [\pm I + \pi\ell + \tau(\beta - \eta q - \eta/2)]\mathrm{d}t' \\
&= \pm I_{q+1} + [\pi\ell + \tau(\beta - \eta q - \eta/2)] \\
\theta_{q+1} &= \theta_q \pm [I_{q+1} \pm \pi\ell \pm \tau(\beta - \eta q - \eta/2)]
\end{aligned} \tag{3.30}$$

and

$$\begin{aligned}
\int_{q\tau^-}^{(q+1)\tau^-} \dot{I}\mathrm{d}t &= \int_{q\tau^-}^{(q\tau^-+\Delta t)} \dot{I}\mathrm{d}t + \int_{q\tau^-+\Delta t}^{(q+1)\tau^-} \dot{I}\mathrm{d}t \\
I_{q+1} - I_q &= \tilde{k}\sin\theta_q + 0 \\
I_{q+1} &= I_q + \tilde{k}\sin\theta_q.
\end{aligned} \tag{3.31}$$

Thus the maps become

$$\theta_{q+1} = \theta_q \pm [I_{q+1} \pm \pi\ell \pm \tau(\beta - \eta q - \eta/2)], \qquad I_{q+1} = I_q + \tilde{k}\sin\theta_q \qquad \text{mod } (2\pi) \tag{3.32}$$

The assumptions made in these integrals are that during the kick, which is on for short time Δt ($\delta-$kick), the potential term in Hamiltonian (3.27) dominates the

kinetic energy term (which corresponds to the Raman-Nath approximation) and in between kicks, the potential term is zero and the motion is that of a free particle. Furthermore the explicit time dependence of the maps (3.32) can be removed by changing the variable $J_q = I_q \pm \pi\ell \pm \tau(\beta - \eta q - \eta/2)$. Thus the map takes the form

$$\begin{aligned} J_{q+1} &= J_q + \tilde{k}\sin\theta_q \pm \tau\eta, \\ \theta_{q+1} &= \theta_q \pm J_{q+1}. \end{aligned} \tag{3.33}$$

These area-preserving maps are $2\pi-$periodic in J and θ.

CHAPTER 4

EXPERIMENTAL CONFIGURATION

In this chapter the detailed experimental configuration used to create a magneto-optical trap (MOT) and A Bose-Einstein condensate (BEC) of ^{87}Rb atoms is presented. The experimental set up was broadly divided into two optical tables namely the "Laser table" and the "BEC optical table". The Laser table was isolated from the BEC optical table and the light was transported between the two using optical fibers.

4.1 Laser table

4.1.1 MOT laser

The laser optical table consisted of optics which were used to produce light to trap and cool the ^{87}Rb atoms. There were two sets of lasers set up on this table. The master laser and associated injection locked slave lasers, and the repump laser. The latter will be described in the next section. The master laser was a grating stabilized DL 100 Toptica laser in a temperature controlled housing. The laser operated in cw mode and had 20mW of output power. It was frequency locked to the transition between the $5^2S_{1/2}$, $F = 2$ ground state and the cross-over line between the $5^2P_{3/2}$, $F = 2$ and $F = 3$ excited state as shown in Fig. 4.1. Since the output power from the master laser was very low, three other home built diode lasers referred to as slave lasers were used. Each slave laser was a 100 mW cw laser operated in a temperature controlled housing. Following the injection locking techniques modes of the slave lasers were identical to the mode of the master laser.

The optical components used to produced the MOT light are shown in Fig. 4.2. A small portion of light coming out from the master laser was taken to the optical set up to perform saturation absorption spectroscopy, the basis of the frequency locking technique. The collimated laser beam from the laser was initially elliptical in shape, passing through a pair of anamorphic prisms so as to change the profile into a circular shape. A half-wave ($\lambda/2$) plate placed immediately after the prism pair rotated the polarization of the light so that all the light went through a polarizing beam splitter cube (PBSC) that was placed with its rotation axis at 45^o to the vertical. The light was then sent through a Faraday rotator which rotated the polarization of light coming from the left 45^o clockwise, making it horizontally polarized. Any reflected horizontally polarized light passing from the right through the Faraday rotator had its plane of polarization rotated in the other direction so that the light was reflected (eliminated) by the PBSC placed in front of the laser. Thus the master laser was isolated from any reflected and scattered light. About 5 mW of light from the master laser was sent to a slave laser with the help of PBSC for injection locking. In order to monitor whether the slave frequency followed the master laser or not, some light ($\sim 200\mu$W) was directed through a rubidium vapor cell using a partial reflector. This light was monitored using a Thorlabs PDA 400 photodiode model. If it was possible to see an absorption dip on the oscilloscope, the slave followed the master laser. All the slave lasers were setup using near identical procedures. In order to realize a BEC, precise control of the laser frequency was crucial. The following four different laser frequencies were needed:

1. -20 MHz detuning from the $F = 2$ of the $5^2S_{1/2}$ ground state to $F = 3$ of the $5^2P_{3/2}$ excited state transitions to make the MOT (MOT light).

2. -90 MHz detuning from the $F = 2$ of the $5^2S_{1/2}$ ground state to $F = 3$ of the $5^2P_{3/2}$ excited state transitions for optical molasses cooling and loading of the atoms into an optical trap.

3. Exact resonant light with the $F = 2$ of the $5^2S_{1/2}$ ground state to $F = 3$ of the $5^2P_{3/2}$ excited state transition for imaging the atoms (Imaging light)

4. Light for the $F = 1$ of the $5^2S_{1/2}$ ground state to $F = 2$ of the $5^2P_{3/2}$ excited state transitions (Repump light described in the next section).

The first three requirements were met by using several acousto-optic modulators (AOMs) which were electronically controlled by using LabView program. The master laser was locked at a frequency of 133.3 MHz below the MOT transition. After being injection locked to the master laser, the light from the main slave was double passed through an ISOMET 1205 C-2 AOM excited with an rf frequency of f_{AOM} as shown in Fig. 4.4. This AOM was used to change the detuning of the MOT light. Taking the positive first order on each pass through the AOM gave a frequency for the slave light of $f = f_0 + 2f_{\mathrm{AOM}}$), where f_0 is master laser frequency. This light was then used for the injection locking of the other slave lasers referred to as slave 1 and slave 2. The advantage of using the double pass AOM was that use of different frequencies would not cause a deflection of the beam, which was very important in the alignment. A telescopic configuration using two lenses were used for this purpose so that the retro-reflected first order beam from the mirror after the second lens co-propagate with the original beam before the AOM. The light beams from slave 1 and slave 2 were sent together through another ISOMET 1205 C-1 AOM which was driven at frequency of 80 MHz. The negative first order ($f' = f - 80\mathrm{MHz}$) was separated into two beams by using a PBSC and then sent to the BEC optical table by using two polarization preserving, single mode fibers referred to as fiber 1 and fiber 2. It is worthy of note that the coupling efficiency of the fiber depends on the shape and size of the laser beam. Thus using two lenses in a telescopic configuration before the fiber enhanced the coupling efficiency significantly. The final detuning achieved by the light entering

the vacuum chamber can be found using the equation [30]

$$\delta_{MOT} = -133.3\text{MHz} + 2f_{\text{AOM}} - 80\text{MHz}. \tag{4.1}$$

To obtain a good MOT, -20MHz detuning was normally used. This was achieved by driving the double pass AOM at a frequency of $f_{\text{AOM}} = 96.65$ MHz. The -90MHz detuning and resonant imaging light required the double pass AOM be driven at frequencies $f_{\text{AOM}} = 61.65$ MHz and 106.65 MHz respectively.

4.1.2 Repump laser

Due to the power broadening mechanism, there is always some possibility that atoms excited to the $5^2P_{3/2}$, $F = 3$ excited state by the MOT light can decay to the $5^2S_{1/2}$, $F = 1$ ground state, so that without further intervention the MOT would disappear. To prevent this and maintain a closed "cycling" transition an additional laser called the repump laser is needed. The repump laser depopulates the $F = 1$, $5^2S_{1/2}$ state in order to maintain the cycling transition for the MOT.

The repump laser was a grating stabilized DL 100 Toptica laser in a temperature controlled housing which was frequency locked to the cross over line between the $5^2S_{1/2}$, $F = 1$ to $5^2P_{3/2}$, $F = 1$ and $F = 2$ excited state. The optical alignment of the repump laser was similar to that of the master laser as described above and is shown in Fig. 4.4. The laser was double passed through an ISOMET 1205 C-2 AOM driven by an ISOMET model 301B voltage tunable rf driver. The positive first order after double pass was sent to the BEC optical table with the MOT light beam in fiber 2. This enabled the atoms to be excited from the $5^2S_{1/2}$,$F = 1$ ground state to the $5^2P_{3/2}$, $F = 2$ excited state and thus to eventually decay to the $5^2S_{1/2}$, $F = 2$ state. During the loading of the atoms into the optical dipole trap, the repump power had to be reduced to optimize the loading. This was done by changing the rf power in the AOM via a command from the controlling LabView program.

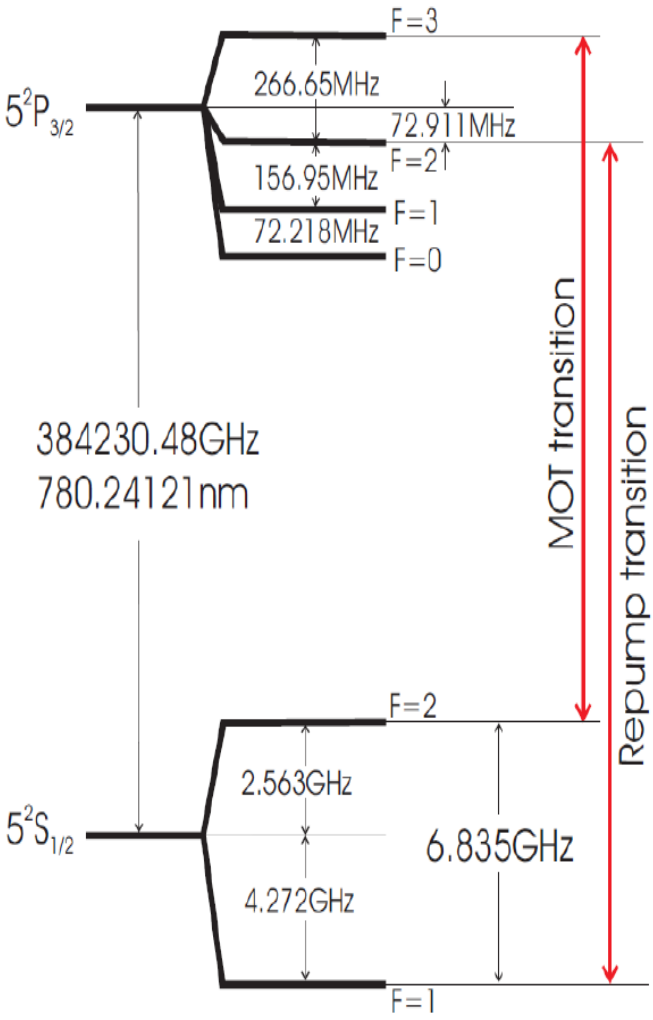

Figure 4.1: Energy level structure of Rubidium-87 D2 line. The transitions for MOT light and repump light are shown.

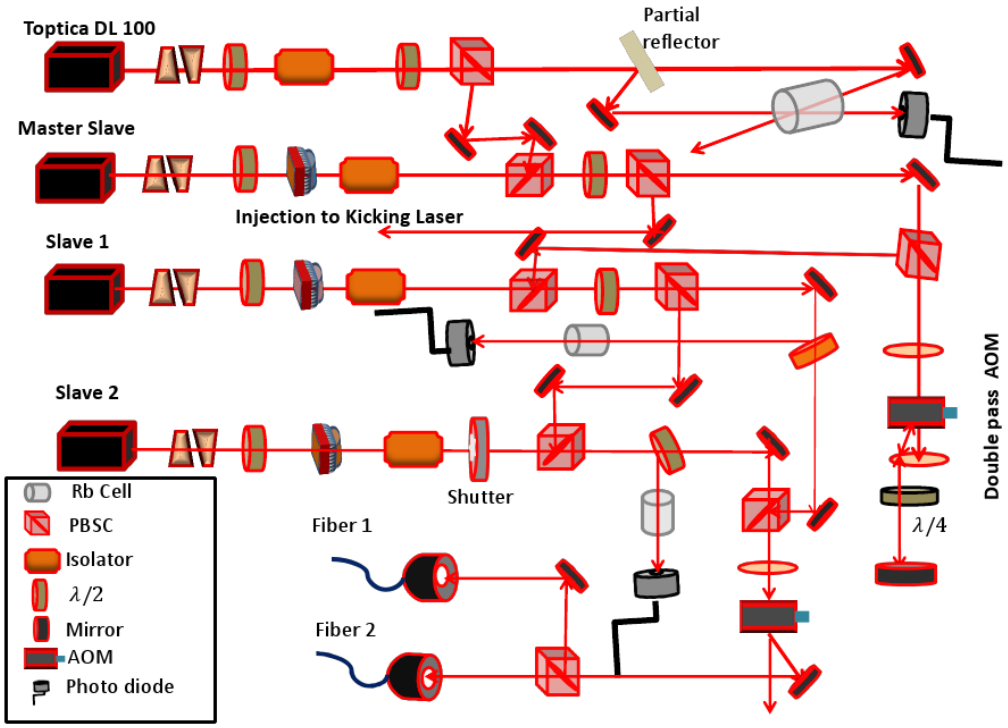

Figure 4.2: Optical setup on the laser optical table showing various optical components and lasers used to prepare the MOT light.

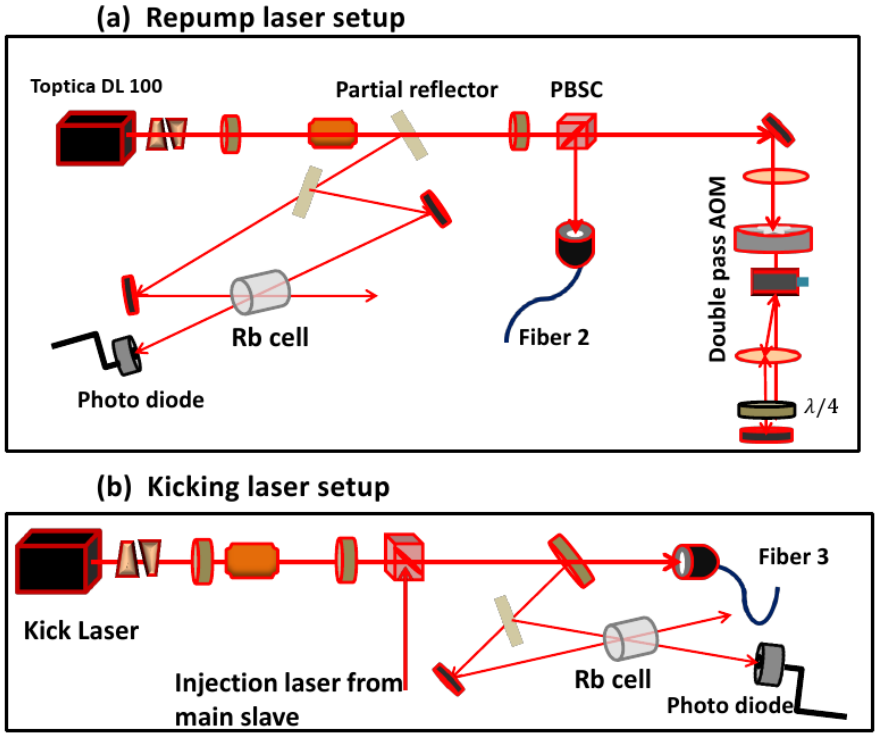

Figure 4.3: Optical setup for (a) repump and (b) kicking lasers.

4.2 BEC optical table

The heart of the experiment was located on the BEC optical table where the vacuum chamber (discussed later) was placed. The optical setup on this table is shown in Fig. 4.5. The light exiting from fiber 1 consisted of a MOT beam (Beam 1) and the imaging beam. Fiber 2 contained a MOT beam (split into two by a PBSC to form Beam 2 and Beam 3) and a repump beam. The beams were expanded to about an inch diameter by using a combination of two lenses and were separately sent through quarter-wave ($\lambda/4$) plates to make the light circularly polarized. For fiber 1 a small portion of the light was taken as an imaging beam using a partial reflector and the main portion of the light was expanded and sent through a quarter-wave plate. These three expanded MOT beams were sent into the vacuum chamber and were retro-reflected using mirrors. These six beams were aligned to intersect at the center of the chamber, with the MOT appearing at the intersection of the beams.

During the experiment, the imaging laser, the MOT laser, and the repump laser were extinguished at different times. In order to facilitate this, each laser beam was passed through a fast electronic shutter(UNIBLITZ LS2T2). These shutters were controlled by drivers which are connected to digital voltage signals using a PCI 6713 card installed on the computer and the LabView program.

4.3 Imaging system

Figure 4.7 shows the schematic for the imaging system that was used in our lab. A small portion of light which was resonant with the atomic transition from the $5^2S_{1/2},\ F = 2$ ground state to the $5^2P_{3/2},\ F = 3$ excited state exited from fiber 1 to form an imaging beam. It was then expanded to 1 cm diameter using a beam expander and passed through a quarter-wave plate to make it circularly polarized. An absorption imaging technique based on the resonant interaction of light with atoms

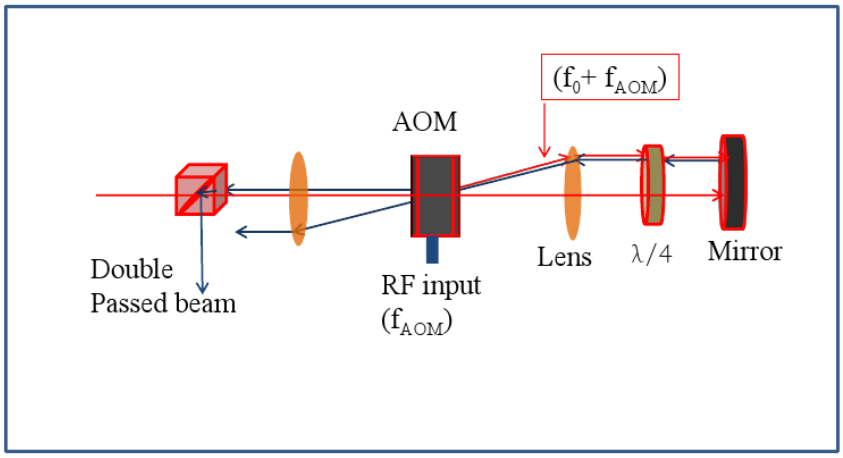

Figure 4.4: A double pass AOM setup. The first order diffracted beam (red) from an AOM placed in between two lenses in a telescopic configuration is retroreflected (blue) and passed through the AOM again. The first order diffracted beam after the second pass co-propagates with the original beam. This light was made orthogonally polarized by sending it twice through a quarter wave plate. It should be noted that the path of the diffracted beam in this setup does not deflect in position, a crucial requirement in the laser cooling and trapping setup. The red and blue lines after the AOM are intentionally drawn slightly apart (even though they really co-propagate) to distinguish the reflected beam from original beam.

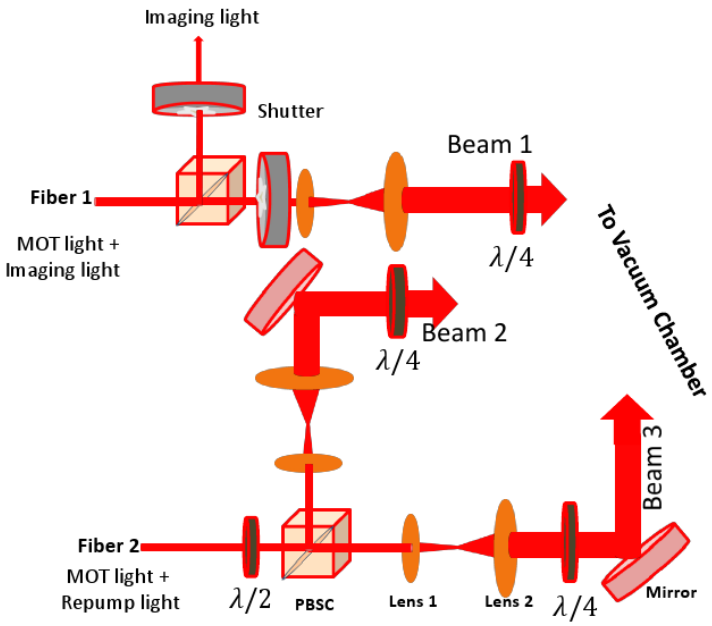

Figure 4.5: Experimental configuration on the BEC optical table. Three MOT beams, the repump laser beam and the imaging beam are shown.

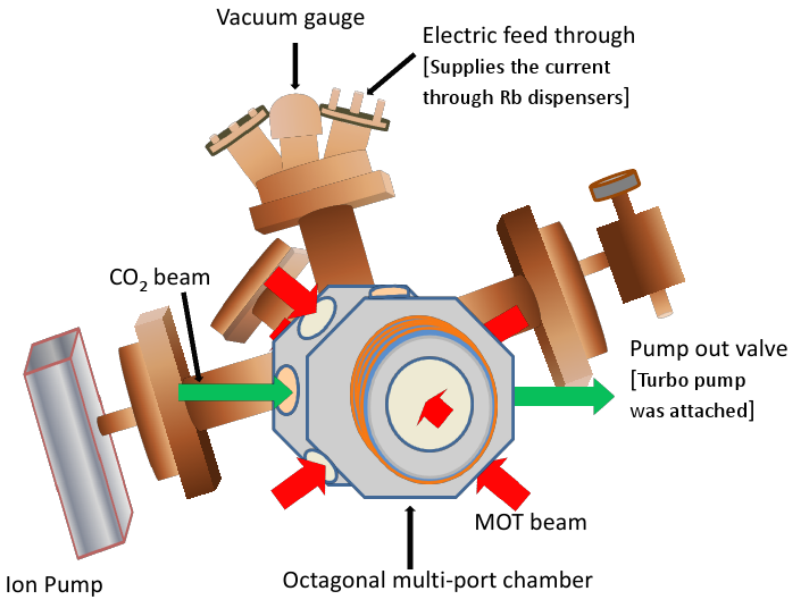

Figure 4.6: Schematic drawing of the vacuum system showing the six way cross and an octagonal multi-port chamber.

was implemented. When the cold atoms were exposed to a weak ($\sim$ 100 nW), short pulse ($50 - 60\mu$s) of resonant light they scattered photons and cast a shadow which was imaged onto a high resolution CCD camera ANDOR DV437-BV. The imaging system is described in more detailed in ref. [28]. The operating temperature and camera shutter time were controlled electronically using the LabView program. The camera had best performance at operating temperature of -20^oC. Two inexpensive security CCD cameras were also used to monitor the MOT in real time.

The number of atoms was calculated from the image as follows: The loss in intensity I of a laser beam traveling in the $z-$direction which passes through a sample of atoms will be given by

$$\frac{dI}{dz} = -\sigma n I, \tag{4.2}$$

where n is the density of atoms and the scattering cross section [36] $\sigma = \frac{\hbar\omega\gamma}{2I_s} = \frac{3\lambda^2}{2\pi}$, with ω the laser frequency, γ the natural linewidth and I_s the saturation intensity. The solution of Eq. (4.2) is $I(x,y) = I_0'(x,y)\exp(-\sigma\tilde{n})$ where $\tilde{n}$ is the column density (number of atoms per unit area). The intensity $I(x,y)$ was found by taking three images. The first image was taken when there was no imaging light to account for background noise which gave the background intensity I_b. The other two images were taken with and without atoms these gave intensity I_1 and I_0 respectively. The intensity profile $I(x,y)$ is then given by

$$I(x,y) = \frac{I_0 - I_b}{I_1 - I_b}. \tag{4.3}$$

The number of atoms can be calculated by integrating over the column density

$$N = -\frac{S}{\sigma}\sum_{\text{pixels}} \ln(I). \tag{4.4}$$

Where $S = (13\mu\text{m})^2$ is the scaled area of a pixel for the ANDOR DV437-BV camera and the sum is taken over all pixels.

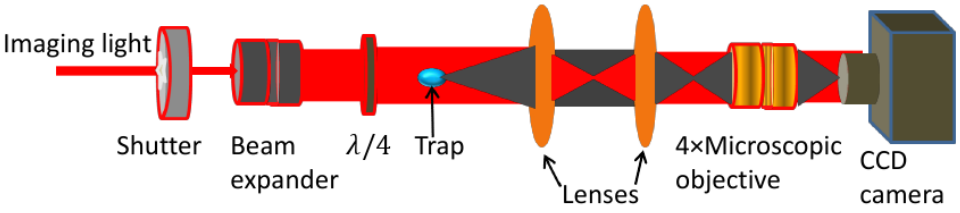

Figure 4.7: Schematic drawing of the imaging setup.

4.4 Vacuum system

The vacuum system is the heart of the experiment. It is where the atoms are trapped, BEC created and the experiments carried out. The vacuum system is shown in Fig. 4.6 and consisted of a six way cross made of stainless steel with an octagonal multi-port chamber from MDC vacuum products attached to one of its flanges. The chamber had four 2.0 inch diameter, antireflection coated, quartz viewports for directing the MOT beams into the chamber, and four 1.0 inch diameter ZnSe viewports. The ZnSe viewports with their low absorption at 10.6 μm were used for directing the high power CO_2 laser beams into the chamber for the dipole trap. A 5.0 inch diameter quartz viewport was attached to one side of the six way cross and another to the large opening on the orthogonal chamber. Each viewport had a conflat flange sealing surface which enabled baking to 200^{o}C.

One side of the six way cross provided an outlet valve to connect a turbo-molecular pump during the initial pumping of the vacuum system . A Turbovac model # 151 C was used for this purpose. A two port generic *Varian style* 8 liter/s ion pump powered by Terrenova 751 controller was connected to another side of the six way cross to maintain a pressure of $\sim 10^{-10}$ Torr. Three SAES Getter rubidium dispenser sources were installed in the vacuum chamber and were connected to electric feed through terminals installed on one side of the six way cross. The remaining side of the six way cross was sealed. The vacuum chamber was shielded from the ion pump's magnetic field using magnetic shields (not shown in the figure).

During the installation process, many precautions were taken to ensure cleanliness. All parts were cleaned with methanol to remove any foreign material and gloves were worn to prevent clean parts from contamination. A Travac-b rotary vane vacuum pump was used as a roughing pump and then a Turbo-molecular pump, Turvac model # 151 C, was turned on to pump the vacuum chamber to a lower pressure. A Varian 0351 vacuum gauge was installed in order to indicate pressures in the range

of atmospheric down to 10^{-4} Torr. The leakage on the system was checked by using Helium and Argon gas, with a sudden increase in pressure while applying the gas to a seal indicative of a leak. Any leaks were removed by tightening the bolts evenly and carefully. The entire vacuum system was then baked in a tent with insulating sides. Ceramic heaters powered by variacs (variable transformers) provided the heat source for the baking process and thermocouples were attached to the various parts of the system in order to monitor the temperature. The temperature was gradually increased and raised to a maximum of $\approx 200^o$C over two days and then left to bake for 3 days. While baking, the turbo-molecular pump was running. The temperature was decreased gradually and the heaters turned off. A Varian Valcon Plus 55 ion pump was turned on which after several weeks pumped the system to a pressure of 10^{-10} Torr.

4.5 Magnetic coil

In order to trap and cool the atoms, a suitable magnetic field gradient, in addition to the optical field provided by the lasers was also required. The necessary magnetic field was provided by a pair of coils (referred to as the main coils) in anti-Helmoltz configuration (identical coils separated from each other by a distance equal to its radius with current flowing in opposite direction). The coils had a radius of 3 inches and consisted of 5×5 layers (25 turns) of copper tube with a square cross section of external dimension of 0.125 inch and internal dimension 0.016 inch. The coil was designed in such a way that coolant could circulate internally so that a large current could be used in the experiments if needed. In order to trap atoms and create BEC about a 16A current was supplied. This produced an inhomogeneous magnetic field between the coils with a field gradient of $\approx 16G$/cm and a zero field at the center as shown in Fig.4.8. The current was supplied by a remotely programmable Lambda ESS 45-333-2-D DC power supply which required a three phase 190-250 V, 60A AC

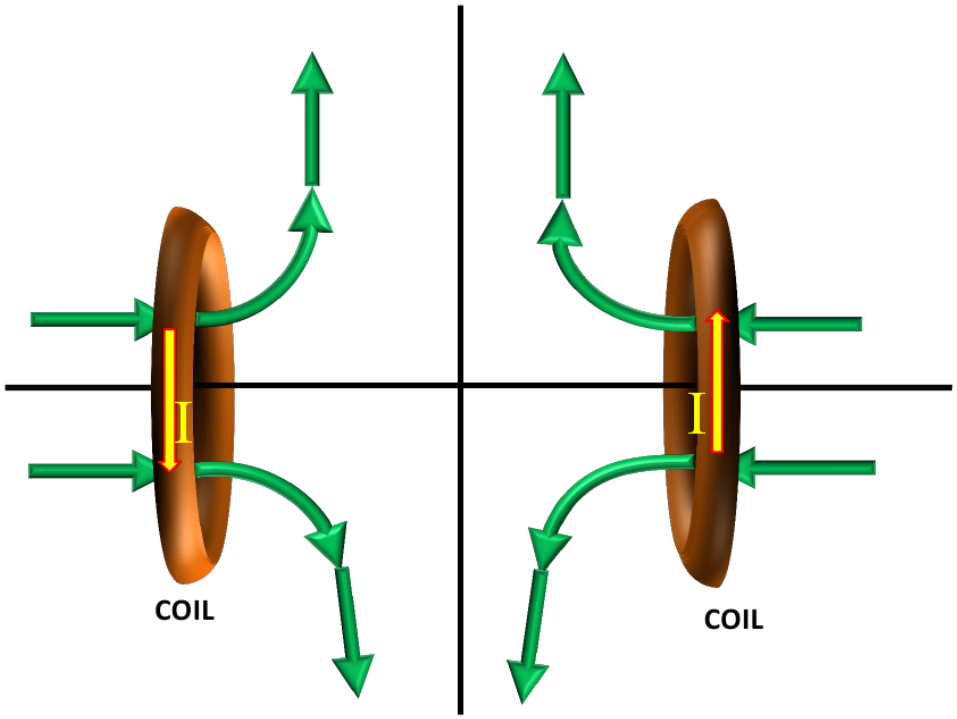

Figure 4.8: Schematic drawing of the coil system. The pair of coils is placed in anti-Helmholtz configuration to produce a zero magnetic field and an approximately linear field gradient near the center.

input. The power supply was reconfigured so that it was able to supply up to 400A DC current controllable with an external 0V to 5V analog signal. Alternatively, the current on the magnetic coils can be turned on and off by using a solid state switch as explained in Appendix A.

Additionally, three pairs of coils were positioned on all six sides of the trapping chamber to nullify the Earth's magnetic field and any stray field produced by other sources. Each coil in a pair had current flowing in the same direction and each pair was powered by a separate DC power supply. Keeping future experiments in mind, one more set of coils made of solid copper wire was wrapped on top of the main coils, however they were not used for the current experiments. The resistance of the copper tube in main coils was 2.356 mΩ/m so the total resistance of a coil was only 28 mΩ ($L = 12$m). With the help of this information, the heat energy developed in the coil can be estimated by $Q = I^2Rt$, where Q, I, R and t are respectively heat energy, current, resistance, and time. Thus a cooling system can be designed accordingly.

4.6 CO_2 laser system

A 50 W cw laser beam at 10.6μm wavelength was used to produce a far off-resonant trap or FORT. This beam originated from a Coherent GEM Select 50 CO_2 laser powered by an Agilent 6573A DC power supply. Thermal plates made with an anodized aluminium heat sink overlayed with thermal sensitive phosphor was used to align and detect the beam. When these thermally sensitive phosphor plates were exposed to infrared laser radiation, the absorbed energy raised the surface temperature and produced corresponding thermal images. These images appeared as dark spots when illuminated by ultraviolet light ($3600A^o$), with the darkness of the spot increasing with laser power. A Macken Instruments' Lamp Model 22-UV was used to sensitize the plates.

Due to the high absorption coefficient of glass and quartz at 10.6μm, the usual

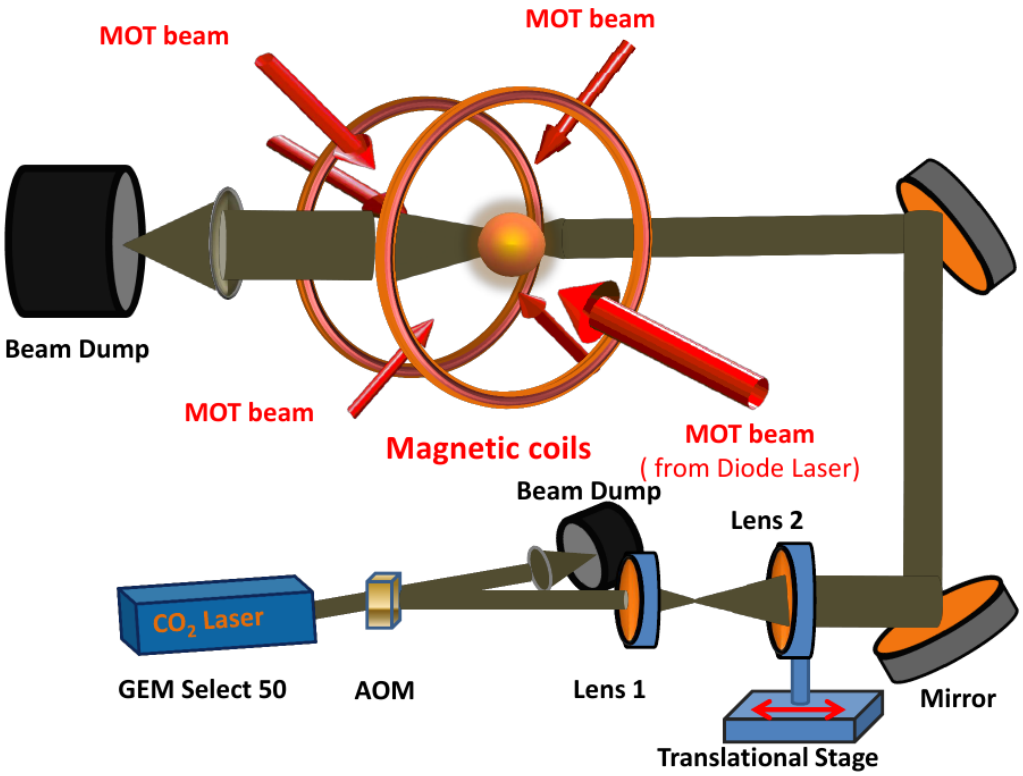

Figure 4.9: CO_2 beam geometry. When aligning the HeNe laser described in the text the beam dump was removed.

optics for the near infra-red MOT lasers could not be used. One of the materials with the lowest absorption coefficient at this wavelength is Zinc-Selenide (ZnSe). Lenses and viewports were made of this material. The 50W laser beam exited from the CO_2 laser and was carefully aligned and directed to the vacuum chamber as shown in Fig. 4.9. The beam was passed through a water cooled Intra Action Corp. Model AGM-406B1 AOM driven by Intra Action Modulator Driver Model GE-4030H which was electronically controlled by using an analog voltage signal from the computer. The AOM was placed as close as possible to the laser source in order to minimize the divergence of the beam which is quite substantial due to the long wavelength. The zeroth order AOM beam was sent to a beam dump and the first order beam ($\approx$ 30W) was transported into the chamber through an assembly of three lenses. The first two lenses formed a beam expander in a telescopic configuration and were followed by a third focussing lens of focal length 1.5 inches which was installed inside the vacuum chamber. The beam was directed into the chamber through a 1 inch diameter ZnSe viewport. The final spot size of the beam at the center of the chamber was $w_0 = \lambda f/(\pi R)$, where R is the radius of the beam incident on the third lens and f is the focal length of the lens. For the loading and evaporative cooling phases, the beam waist was set at either a large or small size respectively. In order to facilitate this, the second lens of the beam expander was mounted on a Aerotech translation stage Model 101SMB2-HM driven by a Soloist driver interface.

4.6.1 CO_2 beam alignment with the MOT

The frequency of the CO_2 light is far-off resonant from any electronic transition of the Rb atoms making it difficult to align the FORT beam with the MOT. Compounding the difficulty of manipulating this light is that it is invisible to the eye and very high power. The method (trick) that was used for aligning purposes required several steps. First, since the MOT was formed at the center of the chamber, a HeNe laser was sent

from the other end of the chamber through the center of both ZnSe viewports in the opposite direction to that of the CO_2 laser. The HeNe laser was aligned through the rest of the optics by using mirrors, with two pinhole apertures used to define the beam path. Finally the CO_2 beam was aligned to pass through the same apertures by adjusting its optical components before the apertures. After this procedure the FORT beam usually passed through the center of the ZnSe viewports and hence through the center of the chamber where the MOT was located. In order to observe the FORT beam, the fluorescence of the MOT was reduced by increasing the detuning of the MOT light from resonance. The FORT beam was then turned off and on every 500 ms and the MOT was slowly moved in x, y and z directions with the help of the three pairs of nulling coils. Due to the Stark effect changing the effective detuning of the MOT light, the presence of the far off-resonant electric field could be seen as a flashing of the MOT at the location of the CO_2 light.

4.7 Polarization

In order to produce the magneto optical trap, the polarization configuration of the six MOT beams was very important. Setting the beams to a circularly polarized state was not sufficient. The four beams which propagate along the direction perpendicular to the axis of the coils used to produce the magnetic field gradient should all have the same circular polarization relative to the direction of propagation of the beams. On the other hand the beams that propagate along the axis of the coil should have opposite circular polarization to the first four beams. The σ^+ and σ^- polarization configurations of the beams are determined by the direction of current on the coils. Although in principle it is possible to set the polarization of all beams correctly with respect to the field gradient, in practice it is much simpler to set the polarization combinations of the six beams by switching the direction of current on the coils to determine which sign of the magnetic field gradient makes the trap work.

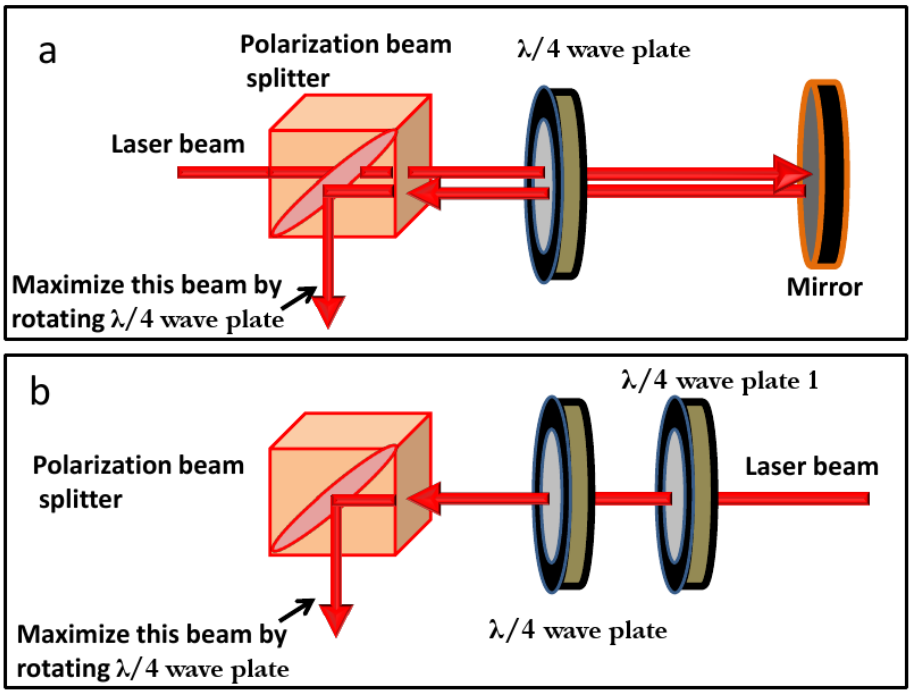

Figure 4.10: Schematic to set up the circulation polarization analyzer (a). Panel (b) shows how to use the analyzer to make a circularly polarized laser beam.

A circular polarization analyzer was used to make the beams circularly polarized. The analyzer consisted of a combination of a PBSC cube, a $\lambda/4$ waveplate and a mirror as shown in Fig. 4.10 (a). A laser beam sent from the left was reflected back using a mirror and the beam reflected from the cube was maximized by rotating the $\lambda/4$ waveplate. Then using the analyzer, the MOT beams directed into the chamber were made circularly polarized with the help of "$\lambda/4$ waveplate 1". The reflected and transmitted beam from the cube showed the amount of light in each type of circular polarization. Pure circular polarization was obtained by rotating the $\lambda/4$ waveplate 1 until all the light from cube was either transmitted or reflected as shown in Fig.4.10(b). Each of the retro-reflected MOT beams was sent through an additional $\lambda/4$ wave plate so that the three pairs of MOT beams would have correct σ^+, σ^- combinations.

4.8 Kicking Laser alignment

The kicking laser was derived from a slave diode laser which was injection locked to the master laser from the $5^2S_{1/2}$, $F = 2$ ground state to the cross over line between $5^2P_{3/2}$, $F = 2$ and $F = 3$ excited state. It was thus 6.8 GHz red detuned with respect to the atoms in the condensate which is in the $5^2S_{1/2}$, $F = 1$ state (Fig. 4.1). This laser was transported to the BEC table using a single mode polarization preserving fiber. On the BEC table, the light exited the fiber and was divided into two beams using a 50-50 beam splitter cube. Each of these beams had 20 mW of power and was separately passed through an Isomet Model 40N AOM. The first order beam diffracted by the AOMs was directed into the vacuum chamber using the same two view ports used for two of the MOT beams as shown in Fig. 4.11. Each beam made 53^o with the vertical forming a horizontal standing wave of wavelength $\lambda/2\sin 53^o$, where $\lambda = 780nm$.

Each AOM was driven by an rf electrical signal supplied by an arbitrary waveform

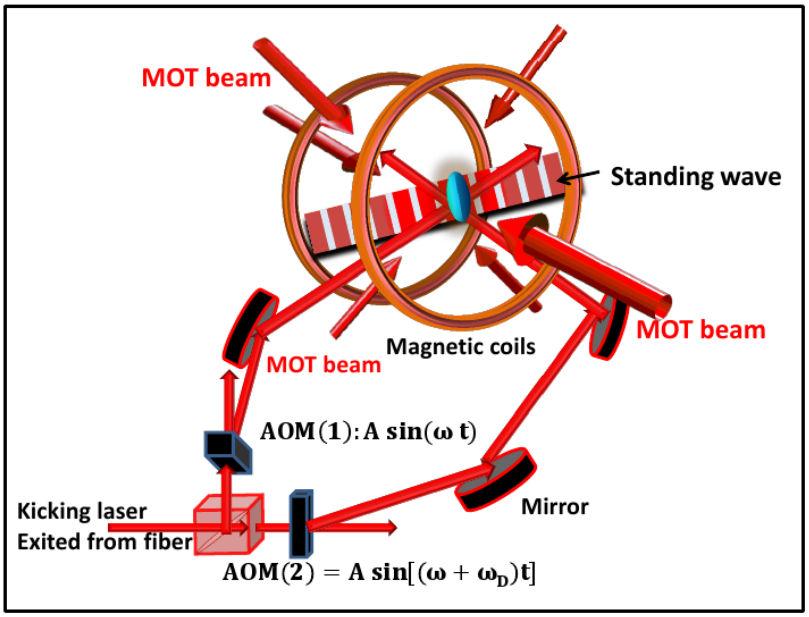

Figure 4.11: Optical setup for the kicking standing wave. Two laser beams were sent into the chamber making 53^o to the vertical thus forming a horizontal standing wave.

generator HP8770A which passed through a 1W amplifier. This rf signal generates the acoustic wave in the AOM and thus the first order beam diffracted by the AOM is Doppler shifted by an amount equal to the frequency of the acoustic wave. The same order from both AOMs was used for each kicking beam. One of the AOMs was driven by a function generator HP8770A at a fixed 40 MHz frequency while the other was driven at a variable frequency by another HP8770A which was phase-locked to the first one. Each of these function generators was programmed using a GPIB interface card allowing for control of all rf waveform properties directly from a LabView program. By adjusting the variable part of the frequency, $\omega_D = \frac{2\pi}{T_{1/2}}\beta + \frac{1}{2}Gat$, where $G = \frac{4\pi}{\lambda}\sin 53^o$ is the grating vector of the standing wave and $T_{1/2}$ is the half Talbot time (discussed later), the initial (quasi) momentum β, and the acceleration a, of the standing wave relative to the condensate could be controlled.

4.9 Bose-Einstein condensation of ^{87}Rb

The atomic gas BEC can be regarded as a macroscopic matter wave that is an ideal testing ground for the investigation of quantum many-body physics. BEC can also be regarded as an atom laser since it provides a phase-coherent intense atomic source. With the advent of laser cooling and trapping as well as the evaporative technique, alkali atoms became the best candidates for realizing BEC since their optical transitions can be addressed by available lasers. They also have a favorable internal energy-level structure for cooling to a very low temperature.

In order to create a BEC in our lab, atomic vapor of ^{87}Rb is used which can be cooled and trapped by using inexpensive diode lasers at a wavelength of 780nm. We employed all-optical trapping method pioneered by M. Chapman's group [25, 26] at the Georgia Institute of Technology to create BEC. We started by creating a MOT of about 30 million atoms and then a high power single beam from CO_2 laser was aligned with the MOT using a technique described in Chapter 4.6.1. A focused CO_2

laser beam at a wavelength of 10.6μm which is far detuned from the atomic transition forms a far off-resonant trap (FORT). The effect of this laser beam on the atoms can be considered as that of a static electric field. This electric field induces a dipole moment on the atoms which then interacts with the electric field of the radiation. Since the laser frequency is far below the atomic transition (red detuned), it creates an attractive interaction potential given by

$$U = -\frac{1}{2}\alpha_g E^2. \tag{4.5}$$

Where $\alpha_g (= 5.3 \times 10^{-39} m^2 C/V$ for ^{87}Rb) is the ground state polarizabity of atoms. For a gaussian beam propagating in the $z-$direction, the electric field $E(x, y, z)$ is given by

$$E(x, y) = E_0 \frac{\exp\left[\frac{-(x^2+y^2)}{w_0^2(1+(z/z_R)^2)}\right]}{\sqrt{1+(z/z_R)^2}}. \tag{4.6}$$

Where w_0 is the beam waist size at the focus and $z_R = \pi w_0^2/\lambda$ is the Rayleigh range which gives the axial extent of the trap. Taking $z << z_R$, the trapping potential can be approximated as a harmonic potential given by

$$\begin{aligned} U &\approx -\frac{1}{2}\alpha_g E_0^2 \left(1 - \frac{2x^2}{w_0^2} - \frac{2y^2}{w_0^2} - \frac{z^2}{z_R^2}\right) \\ &= -U_0 + \frac{1}{2}\left[K_x x^2 + K_y y^2 + K_z z^2\right]. \end{aligned} \tag{4.7}$$

Where K is a positive constant. The trapping frequencies defined as $w = \sqrt{K/M}$ in x, y, and z directions are given by

$$\begin{aligned} w_x = w_y &= \sqrt{2\alpha_g E_0^2/(M w_0^2)} \\ w_z &= \sqrt{\alpha_g E_0^2/(M z_R^2)}. \end{aligned}$$

The Output of the CO_2 laser was passed through an AOM driven by a 40 MHz RF signal. The first order diffracted beam from the AOM was overlapped with the MOT for about 20 seconds in order to load the atoms in the FORT trap. Then the power on the repump MOT laser beam, which was originally about 1.8 mW

(intensity $\approx 1\mathrm{W/m}^2$), was reduced by a factor of at least 10 to make a temporal dark SPOT [82, 83]. This is a very crucial step for effective loading, where the atoms start entering into a state that is "dark" to the cooling light. The resultant decrease in the recoil heating and the excited state collisions lead to an increase in the phase space density. The detuning of the cooling light was then changed to -90 MHz so that even after the consideration of the ac-stark shift between the ground and the excited states which reduces their energy difference, the atoms still see the MOT beams negatively detuned. About 100 ms later, the MOT beams and repump beam were extinguished by using fast electronic shutters and the magnetic field was turned off by reducing the current on the coils to zero. About 2 millions atoms were loaded in the trap. During the loading, the FORT beam had a waist of about 100μm so as to optimize the loading, it was then compressed tightly to about 25μm to increase the elastic collision rate and hence the efficiency of the evaporative cooling. This was done by using the beam expander geometry discussed in Chapter 4.6.

The next step was to implement a two-stage evaporative cooling (EVC) process. The first stage was an exponential ramp down of the CO_2 laser power from 35 W to about 2W with a time constant of 2 seconds. This was done by reducing the RF power driving the CO_2 AOM. The second stage involved the reduction of laser power in a series of tiny steps followed by a times to allow rethermalization. The power in the second stage was reduced to about 50mW over 5s, to produce a pure condensate of about 40,000 atoms in the $5S_{1/2}$, $F = 1$. In order to image the BEC, a destructive absorption method was used. After being released from the trap, the repump light was turned on so that the the atoms on the condensate were pumped $5S_{1/2}$, $F = 2$ state. After 9 ms of expansion, the BEC was then exposed to a 100ns pulse of imaging light which was resonant with the transition from the $5S_{1/2}$, $F = 2$ to the $5P_{3/2}$, $F = 3$ state. Due to absorption, a shadow of the BEC was observed on the CCD camera (signal). Taking another image without the condensate (which was

referred as reference image) and dividing with the signal gave the final view of the BEC.

CHAPTER 5

Fidelity

The study of non-linear systems is important to many branches of science. Consequently the chaotic behavior that they can exhibit in the classical regime has been extensively studied and used [75,76,84]. A particularly interesting aspect of such systems is that due to the linearity of the Schrödinger equation, their quantum and classical dynamics can be dramatically different. For this reason the so called $\delta-$kicked rotor and its quantum analog the quantum $\delta-$kicked rotor (QDKR) have received much attention. The latter can be experimentally realized by subjecting a sample of cold atoms to short pulses of an off-resonant standing wave of laser light [53]. The QDKR has proved to be a paradigmatic model to study several important phenomena including quantum resonances (QR) [55, 57–59], dynamical localization [55, 56], and quantum ratchets [60–66]. A closely related system, the quantum delta kicked accelerator (QDKA), differs from the usual QDKR by adding a linear potential in the form of an acceleration. The QDKA has been used in studying aspects of the transition to chaos in both classical and quantum regimes [68], and is a system in which quantum accelerator modes [69–74] are observed.

One of the common themes in the experiments mentioned above is that the quantum evolution is typically measured indirectly through observations of the momentum distribution. However recently it has become possible to study the coherent evolution of a superposition of state vectors directly by examining the overlap of the atomic state with a reference state. This quantity is termed "fidelity". It has garnered considerable interest as an alternative way of studying coherent evolution in the context of

quantum-classical correspondence [85, 86] and quantum information processing [87]. It can be shown that the width of a pulse period fidelity resonance of the QDKR exhibits sub-Fourier scaling [88, 89], where the width of the resonance scales as the inverse cube of the number of applied pulses. Because of this sensitivity to the pulse period, the fidelity technique was proposed as a means for improving the precision of frequency measurements [89]. Although subsequent work has shown possible limitations with this approach [90], there are still parameter regimes where the fidelity may be useful for precision measurements. In this chapter both theoretical and experimental aspects of fidelity measurements are discussed for the QDKR and the QDKA.

5.1 Fidelity of a quantum $\delta-$kicked rotor

The theory and mathematical details of fidelity in the case of the quantum $\delta-$kicked rotor are presented in references [31, 88, 89]. In this section we give a brief review of the theory as well as experimental and numerical simulation results.

The dynamics of the QDKR can be described by a Hamiltonian (3.10) which in dimensionless units is:

$$\hat{H} = \frac{\hat{p}^2}{2} + \phi_d \cos(\hat{x}) \sum_{q=1}^{\mathrm{t}} \delta(t' - q\tau). \tag{5.1}$$

We start from the evolution of an initial state $|\psi(0)\rangle$ due to t kicks at a period close to the Talbot time, i.e., $\tau = 4\pi + \varepsilon$, which is given by

$$|\psi(t' = \mathrm{t}\tau)\rangle = \hat{\mathcal{U}}^{\mathrm{t}}|\psi(0)\rangle. \tag{5.2}$$

Where $\hat{\mathcal{U}}$, the one-period evolution operator, is given by

$$\hat{\mathcal{U}} = e^{(-i\hat{p}^2\tau/2)} e^{-i\phi_d \cos(\hat{x})}. \tag{5.3}$$

As noted previously, at quantum resonance the free evolution term $e^{(-i\hat{p}^2\tau/2)} = 1$ so the kicks add constructively such that several kicks behave like a single kick of

strength equal to the sum of the individual kicks. McDowall et al. [88] proposed a scheme for measuring the fidelity of a QDKR by the application of a tailored pulse at the end of a rotor pulse sequence. The fidelity is then defined as

$$F = |\langle\psi(0)|\hat{\mathcal{U}}_R\hat{\mathcal{U}}^{\mathrm{t}}|\psi(0)\rangle|^2, \tag{5.4}$$

where $\hat{\mathcal{U}}_R = e^{[i\mathrm{t}\phi_d\cos(\hat{x})]}$ is the tailored pulse, shifted in phase by π (that is the potential is displaced by $\lambda_G/2$) and carrying a strength of $\mathrm{t}\phi_d$. This is referred to as a "reversal pulse". A perturbative treatment near the Talbot time, $\tau = 4\pi + \varepsilon$, where ($\varepsilon \ll 1$) showed that the fidelity is given by [88]

$$F(\varepsilon, \beta = 0, \eta = 0) \simeq J_0^2\left(\frac{1}{12}\mathrm{t}^3\phi_d^2\varepsilon\right), \tag{5.5}$$

where J_ℓ is the Bessel function of the first kind. Thus the fidelity width in ε scales as $1/(\mathrm{t}^3\phi_d^2)$, displaying a sub-Fourier dependence on the measurement time, expressed in units of kick number. In a similar way, we investigated the effect of acceleration on fidelity at Talbot time. The derivations of the theory are detailed in [31]. For a perturbation only due to acceleration close to $\eta = 0$, this leads to an expression for the fidelity which is

$$F(\eta, \beta = 0, \varepsilon = 0) \simeq J_0^2\left(\frac{4\pi}{3}\mathrm{t}^3\phi_d\eta\right). \tag{5.6}$$

This shows that the width of the fidelity peak centered at zero acceleration ($\eta = 0$) drops as $1/\mathrm{t}^3$, which is again sub-Fourier. With a similar approach, the fidelity as a function of the initial momentum, β, near $\beta = 0$ is [88]

$$F(\beta, \eta = 0, \varepsilon = 0) \simeq J_0^2\left[2\pi\phi_d\mathrm{t}(\mathrm{t}+1)\beta\right]. \tag{5.7}$$

.

5.1.1 Experimental configuration and results

Our experiments to investigate the fidelity of a kicked rotor were performed by creating a BEC of about 30,000 ^{87}Rb in the $5S_{1/2}$, $F = 1$, $m_F = 0$ level. The creation of

the $m_F = 0$ Zeeman sublevel BEC was done by keeping the magnetic field on during evaporative cooling. Only atoms in the $m_F = 0$ level, which are insensitive to the magnetic field, undergo a stable evaporation and the pure condensate in the $m_F = 0$ level is produced.

Approximately 5 ms after being released from the trap, the condensate was exposed to a pulsed horizontal standing wave as shown in Fig. 4.11. This was formed by two laser beams of wavelength $\lambda = 780$ nm, detuned 6.8GHz to the red of the atomic transition. The direction of each beam was aligned at 52^{o} to the vertical. With these parameters the primary QR (half-Talbot time) occurred at multiples of 53.25 ± 0.05 μs. Each laser beam passed through an acousto-optic modulator driven by an arbitrary waveform generator. This enabled control of the phase, intensity, pulse length, and the relative frequency between the kicking beams.

The kicking pulse sequence used in these experiments is shown in Fig. 5.1. The atoms were exposed to a set of t periodic pulses (forward pulses) each of length 0.8 μs and kicking strength $\phi_d = 0.6$ followed by the reversal pulse with a strength tϕ_d. The reversal pulse was obtained by displacing the standing wave by $\lambda_G/2$. We varied the intensity rather than the pulse length to change the kicking strength ϕ_d. This was done by adjusting the amplitudes of the RF waveforms driving the kicking pulses. This ensured that the experiments were always performed in the Raman-Nath regime (the distance an atom travels during the pulse is much smaller than the spatial period of the potential). Adding two counterpropagating waves differing in frequency by Δf resulted in a standing wave that moved with a velocity $v = 2\pi\Delta f/G$. Since the quasi-momentum β of the BEC relative to the standing wave is proportional to v, changing Δf enabled the value of β and η to be systematically controlled. Finally the kicked atoms were absorption imaged in a time-of-flight experiment. A time-of-flight image of a kicking sequence on resonance is shown in Fig. 5.2.

Experimentally the fidelity was defined as $F = p_0/\sum_n p_n$ where p_n is the number

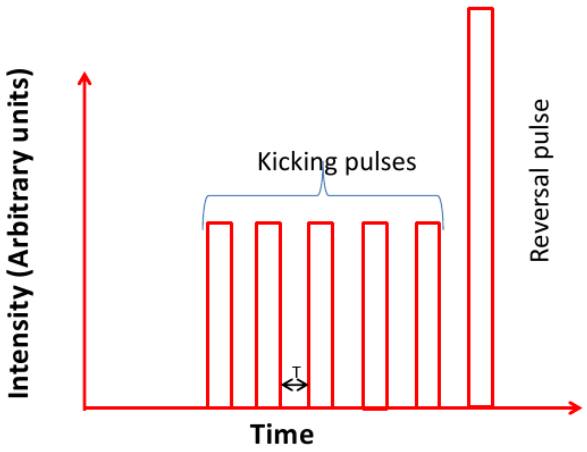

Figure 5.1: The schematic of the pulse sequence used in the fidelity experiment. A sequence of t rotor pulses each of strength ϕ_d was followed by a $\pi-$phase shifted reversal pulse of strength $t\phi_d$.

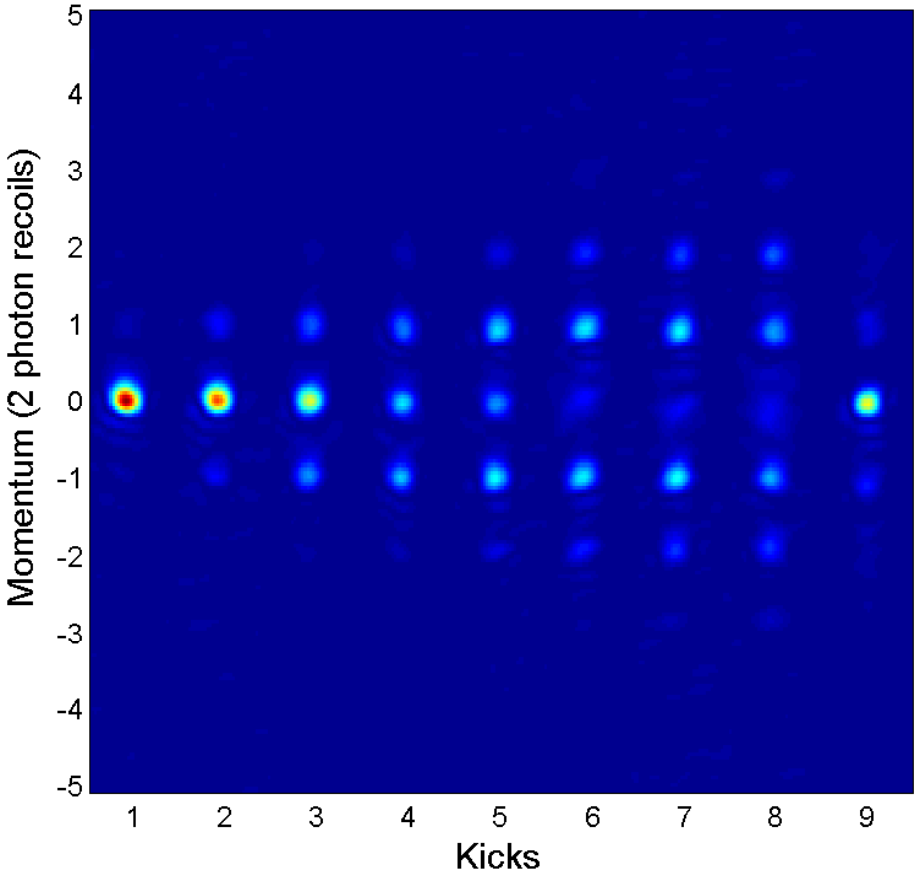

Figure 5.2: Horizontal stack of the momentum distributions due to a sequence of 8 kicks of strength ϕ_d=0.6 with a pulse period equal to the Talbot time, 106.5μs, followed by a $\pi-$phase shifted reverse kick of strength $8\phi_d$.

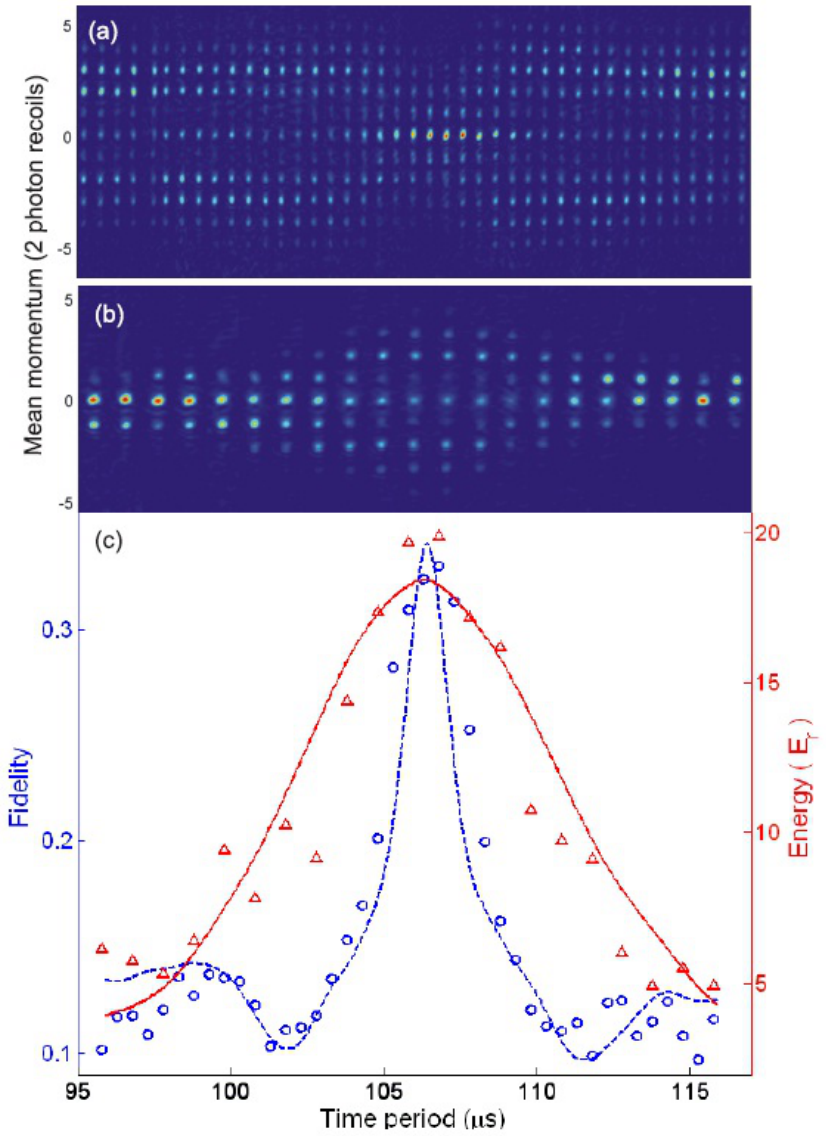

Figure 5.3: Pulse period scans comparing fidelity and mean energy. (a) Shows the momentum distributions from a fidelity experiment around the Talbot time. Each image was due to 5 kicks with $\phi_d = 0.6$ followed by a $\pi-$phase shifted reversal kick of strength $5\phi_d$. In (b) The experiment consisted of 5 kicked rotor pulses (no reversal). Panel (c) shows the fidelity (circles) and mean energy (triangles) derived from the data in (a) and (b). Please see the main text for a description of how these quantities are determined. The results of numerical simulations of the experiment for a condensate with an initial momentum width of $0.06\hbar G$ are also plotted for fidelity (blue dashed line) and for mean energy (red solid line). The offset and amplitude of the simulated fidelity were adjusted to account for the experimentally imperfect reversal phase.

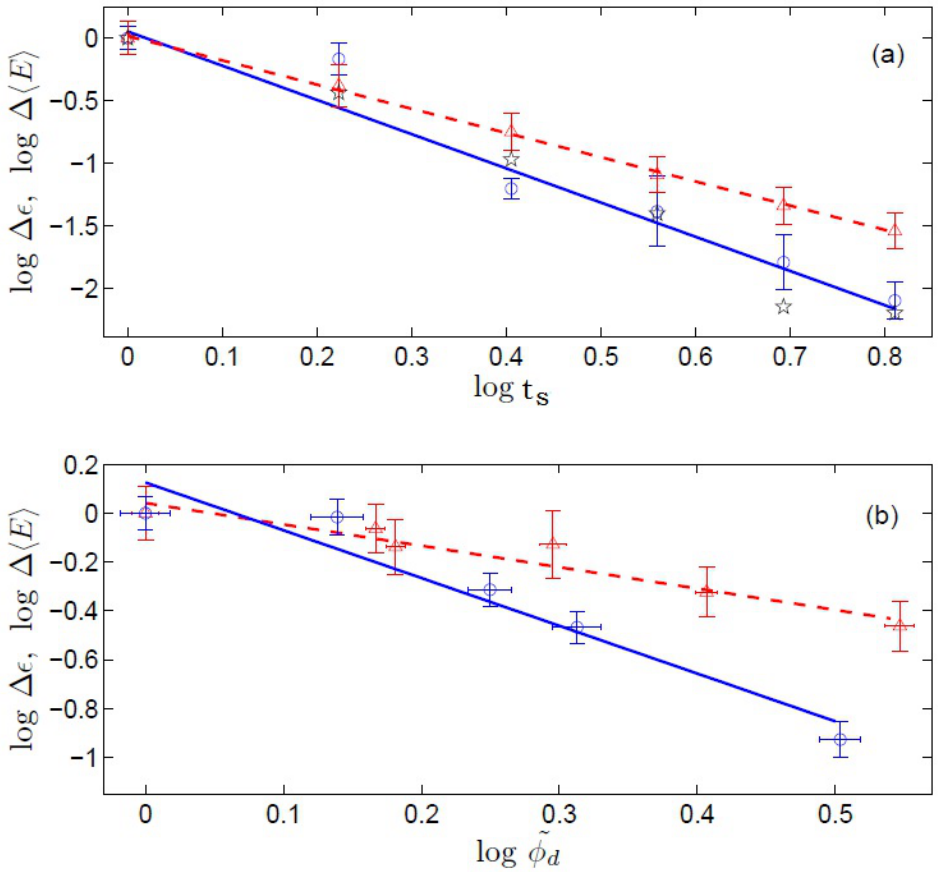

Figure 5.4: The plot of pulse period fidelity resonance width (FWHM) (circles) and the mean energy width (FWHM) (triangles) as a function of (a) scaled kick number and (b) scaled kick strength. In (a) the data are for 4 to 9 kicks in units of width that are normalized to the 4^{th} kick. In (b) the kick strength $\tilde{\phi}_d$ is scaled to the strength ϕ_d of the first data point. The lines are the linear fit to the data. Error bars in (a) are found by taking standard deviation from three sets of experiment and in (b) are 1σ of a Gaussian fit to the distribution. Stars are the data from numerical simulations for an initial state with an initial momentum width of $0.06\hbar$G.

of atoms in the n^{th} momentum state. Thus the fidelity is the fraction of atoms which return to the initial momentum state. The fidelity (blue circles) and mean energy (red triangles) due to 5 kicks with $\phi_d = 0.6$ are plotted as a function of pulse period in Fig. 5.3 (c). The results of the numerical simulations of the experiment for a BEC with an initial momentum width of $0.06\hbar G$ are also plotted in the same figure, where the red solid line is the mean energy and the blue dashed line corresponds to the fidelity. It can be seen that even for a few kicks, the fidelity resonance width is much narrower than that of mean energy. The respective time-of-flight images for fidelity and mean energy are shown in Fig. 5.3 (a) and (b).

In order to investigate the scaling of the resonance width with kick number, a scan in pulse period around the Talbot time was performed for each kick. To facilitate the analysis of the data, all of the resonance widths, $\delta\epsilon$, were scaled to that of a reference kick number of t = 4. That is a scaled fidelity width $\Delta\epsilon = \delta\epsilon/\delta\epsilon_{\text{t=4}}$ was calculated for each scaled pulse number $\text{t}_s = \text{t}/4$. From Eq. (5.5) it is expected that $\log \Delta\epsilon = -3 \log \text{t}_s$. The scaled resonance width (FWHM) of fidelity (circles) and mean energy (triangles) as a function of the scaled kick number on a log scale are plotted in Fig. 5.4 (a). A linear fit to the data gives a slope of -2.73 ± 0.13, which is in reasonable agreement (within an experimental error) with the predicted value of -3 [89]. In a similar way the mean energy width (FWHM) $\Delta\langle E\rangle$ was scaled to that of the fourth kick. On the log scale, the width gets narrower with the pulse number with a slope of -1.93 ± 0.21 as shown in Fig. 5.4 (a), in agreement with previous results [57, 108]. In Fig. 5.4 (b), the scaled fidelity width and mean energy width are plotted as a function of kick strength $\tilde{\phi_d}$ scaled to the ϕ_d of the first data point. It was found that the fidelity width changes with ϕ_d with a slope of -1.96 ± 0.30, close to the predicted value of -2 and the mean energy width decreases with a slope of -0.88 ± 0.24 close to the theoretical value which is -1.

From Eq. (5.7), the fidelity width in β is expected to change as $1/[\text{t}(\text{t} + 1)]$

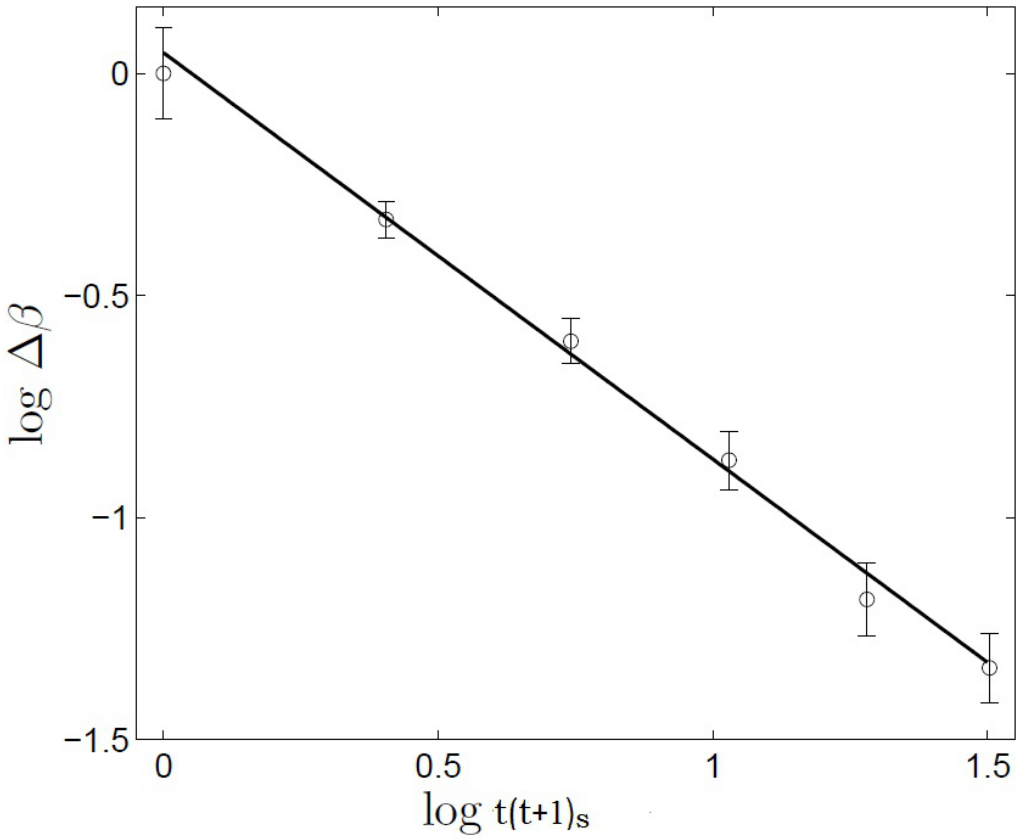

Figure 5.5: Plot of fidelity width in β around $\beta = 0$ as a function of kick number $\mathrm{t(t+1)_s = t(t+1)/20}$ scaled to the fourth kick. A straight line is a linear fit to the data with a slope of -0.92 ± 0.06. Error bars are found by taking standard deviation from three sets of experiment.

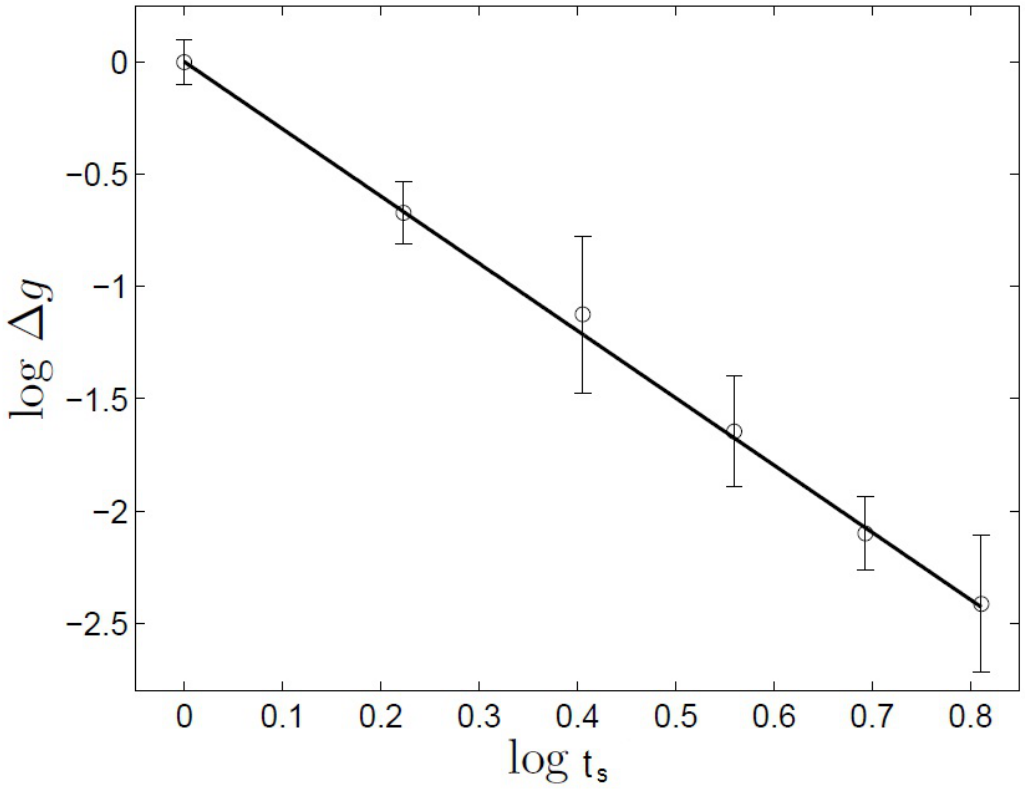

Figure 5.6: The fidelity width in acceleration around $\eta = 0$ at Talbot time as a function of kick number in units scaled to fourth kick. The solid line is a liner fit to the data with a slope of -3.00 ± 0.23. Error bars are the standard deviation from three sets of experiments.

around the resonance. In order to test this prediction, the initial momentum of the condensate with respect to the standing wave was changed by moving the standing wave and several scans were performed around the resonant value of β for 4 to 9 kicks. The measured width in β was then scaled to that of the fourth kick i.e., $\Delta\beta = \delta\beta/\delta\beta_{t=4}$ and was then plotted as a function of $t(t+1)$ in Fig. 5.5. This shows a scaling of $\Delta\beta \propto [t(t+1)]^{-0.92}$ close to the theoretical value.

We also investigated the sensitivity of the fidelity resonance width in acceleration by changing the acceleration of the condensate relative to the standing wave around $\eta = 0$ and at the Talbot time. The width Δg scaled to that of the fourth kick is plotted as a function of kick number in Fig. 5.6. The linear line is a linear fit to the data points and shows that the width of the peak decreases with a slope of -3.00 ± 0.23 in excellent agreement with the value predicted Eq. (5.6). A more in-depth investigation of the fidelity of the $\delta-$kicked accelerator is provided in the following section.

In conclusion, we performed an experimental investigation of the fidelity of the $\delta-$kicked rotor near a quantum resonance. The width of the fidelity resonance peak centered at the Talbot time was found to decrease as $1/t^{2.73}$ in good agreement with the predicted value of $1/t^3$. This is much narrower than the mean energy width that decreases at a rate of only $1/t^{1.93}$. Furthermore, the fidelity width in momentum was found to decrease at the rate of $1/[t(t+1)]^{0.92}$ which is also consistent with the theory. We also demonstrated a $1/t^3$ dependence of the resonance width with acceleration. This fast scaling of the fidelity resonances could be exploited in determining the resonance frequency with a resolution below the Fourier limit. This could lead to measurement of the photon recoil frequency and fine structure constant with higher precision [91–93].

5.2 Fidelity of a quantum $\delta-$kicked accelerator

In this section we discuss in more detail the fidelity of the QDKA. A full analytical theory (neglecting atomic interactions) along with corresponding experimental results and numerical simulations are presented. We show that the width of the resonant peaks in fidelity as a function of acceleration are sensitive to the momentum width of the atomic sample, the pulse period, and the magnitude and direction of the acceleration.

The dynamics of the kicked accelerator are described by the dimensionless Hamiltonian (3.20) which is:

$$\hat{H} = \frac{\hat{p}^2}{2} + \frac{\eta}{\tau}\hat{x} + \phi_d \cos(\hat{x}) \sum_{q=1}^{\mathrm{t}} \delta(t' - q\tau). \tag{5.8}$$

In the absence of acceleration, the above Hamiltonian reduces to the standard kicked rotor system (3.10). Due to the spatial periodicity of the kicking potential the momentum can be decomposed as $p = n+\beta$ where n is the integer part of the momentum and β $(0 \leq \beta < 1)$ is the fractional part of the momentum or quasi-momentum. The spatial periodicity of the kicking potential only allows transitions between momenta that differ by an integer multiple of two photon recoils, $\hbar G$, ensuring the conservation of quasi-momentum. The dynamics of any single value of the quasi-momentum is the same as that of a rotor known as a $\beta-$rotor.

With a non-zero acceleration, the kicked particle becomes the kicked accelerator and the quantum dynamics of the system can be understood by applying the one-step operator,

$$\hat{\mathcal{U}}_{\beta,\phi_d,\eta}(q) = e^{-i\phi_d \cos\hat{\theta}} e^{-i\frac{\tau}{2}(\hat{\mathcal{N}}-\beta-\eta q-\eta/2)^2}, \tag{5.9}$$

which is time dependent. Thus the quasi-momentum will no longer be conserved. However, conservation of quasi-momentum can be restored by writing Eq. (5.8) in a

freely falling frame using a gauge transformation. The Hamiltonian then becomes,

$$\hat{\mathcal{H}}(\hat{\mathcal{N}},\hat{\theta},t') = \frac{1}{2}\left(\hat{\mathcal{N}}+\beta-\eta\frac{t'}{\tau}\right)^2 + \phi_d\cos(\hat{\theta})\sum_{q=1}^{\mathrm{t}}\delta(t'-q\tau). \tag{5.10}$$

Here $\hat{\theta} = \hat{x} \mod (2\pi)$ and $\hat{\mathcal{N}} = -i\frac{d}{d\theta}$ is the angular momentum operator.

In the current fidelity experiments, the initial state $|\psi(0)\rangle$ was kicked t times, each kick having a strength ϕ_d. At the end of the t^{th} kick a $\pi-$ phase shifted reversal kick with strength $\mathrm{t}\phi_d$ was applied. Thus the fidelity for a particular $\beta-$rotor is :

$$F(\eta,\mathrm{t}) = |\langle\psi(0)|\hat{\mathcal{U}}^{\dagger}_{\beta,\mathrm{t}\phi_d,\eta=0}\hat{\mathcal{U}}^{\mathrm{t}}_{\beta,\phi_d,\eta}|\psi(0)\rangle|^2. \tag{5.11}$$

Following the technique introduced in [95, 96], the final expression for the fidelity is then given by,

$$F(\eta,\mathrm{t}) = \Bigg| e^{-i\phi(\beta,\eta,\mathrm{t})-in_0\ell\pi(2\beta+1)(\mathrm{t}-1)+i\ell\pi n_0\eta\mathrm{t}^2} J_0\left(\sqrt{(\mathrm{t}\phi_d)^2+\phi_d^2|W_\mathrm{t}|^2-2\mathrm{t}\phi_d^2\mathrm{Re}W_\mathrm{t})}\right)\Bigg|^2, \tag{5.12}$$

where $p_0 = n_0 + \beta$ is the initial momentum of the plane wave. The global phase $\phi(\beta,\eta,\mathrm{t})$ and $W_\mathrm{t}(\beta,\eta)$ are given by

$$\phi(\beta,\eta,\mathrm{t}) = \ell\pi\sum_{q=0}^{\mathrm{t}-1}(\beta-q\eta-\eta/2)^2 \tag{5.13}$$

$$W_\mathrm{t}(\beta,\eta) = \sum_{q=0}^{\mathrm{t}-1} e^{-i[(2\beta+1)\ell\pi]q+2\ell\pi iq\eta\mathrm{t}-i\ell\pi\eta q^2}. \tag{5.14}$$

In the limit $\eta \to 0$ for $\ell = 2$ and $\beta = 0$, the general result in Eq. (5.12) reduces to Eq. (5.6), obtained there by the use of several approximations. As discussed previously, this shows a sub-Fourier scaling of the fidelity resonance width, verified from the experimental results presented in Fig. (5.6). Equation (5.12) can allow for consideration of cases in which the initial state is a mixture of plane waves, this state is assumed to have a Gaussian distribution with a FWHM = $\Delta\beta$. For a given distribution $\rho(\beta)$ of the quasi-momentum, the formula for fidelity is generalized as:

$$F(\eta,\mathrm{t}) = \Big|\int_0^1 \rho(\beta)\langle\psi(0)|\hat{\mathcal{U}}^{\dagger}_{\beta,\mathrm{t}\phi_d,\eta=0}\hat{\mathcal{U}}^{\mathrm{t}}_{\beta,\phi_d,\eta}|\psi(0)\rangle d\beta\Big|^2, \tag{5.15}$$

where the average is computed numerically based on Eq. (5.12) [94–96]. From the global phase term, $\phi(\beta, \eta, \mathrm{t})$, it can be seen that when $\beta \neq 0$ the phase induced by different values of η depends not only on the magnitude of η but also on its sign.

5.2.1 Experimental configuration and results

Our experiments to investigate this theory were performed using a similar set up to that described in Section 5.1.1 with the exceptions that the BEC was created in the $5S_{1/2}$, $F = 1$ level and the kicking beam was aligned at 53^{o} to the vertical so that the value of half-Talbot time was changed slightly to 51.5 ± 0.05 μs. The value of $\Delta\beta$ was varied by changing the power of the CO_2 laser beam which formed the dipole trap used to perform evaporative cooling in the experiment. By adjusting the final power of the laser beam we were able to change $\Delta\beta$.

Figure 5.7 is the momentum distribution showing the fidelity at multiple values of acceleration due to four kicks with the scaled period of 2π ($\ell = 1$), each of strength $\phi_d \approx 0.6$ followed by a reversal kick of strength $\phi_d \approx 2.4$. The initial momentum $\beta = 0.5$ was used. The experimentally measured fidelity for these experimental parameters as a function of acceleration is shown in Fig. 5.8. Numerical simulations were performed with these experimental parameters under two different conditions. First the black solid line is a simulation in which the reversal pulse is perfect in amplitude (amplitude = $\mathrm{t}\phi_d$), and there are no random phase variations in the standing wave that could be caused by vibrations of the optics used to form it. In order to attempt to explain the large deviation of this simulation from the experiment, we also carried out a simulation in which the above experimental imperfections were included (red dashed line). Here we used experimentally realistic values of strength of the reversal kick ($\pm 7\%$ from the ideal kick strength) and a random phase variation due to vibrations of 0.02π per pulse. As can be seen the fit to the experiment is quite good, leading us to believe that these effects are the most likely reason for the black

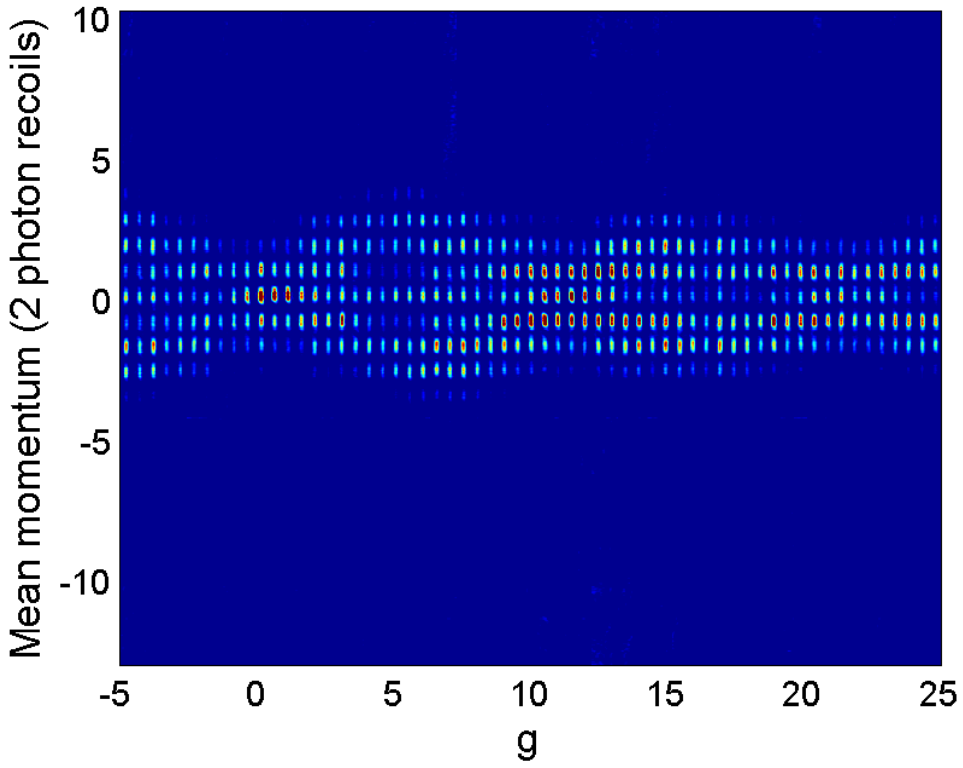

Figure 5.7: Horizontally stacked time-of flight images of a fidelity scan as a function of effective acceleration due to four kicks of strength $\phi_d \approx 0.6$ followed by a reversal kick of strength $\phi_d \approx 2.4$ for $\tau = 2\pi$ and $\beta = 0.5$.

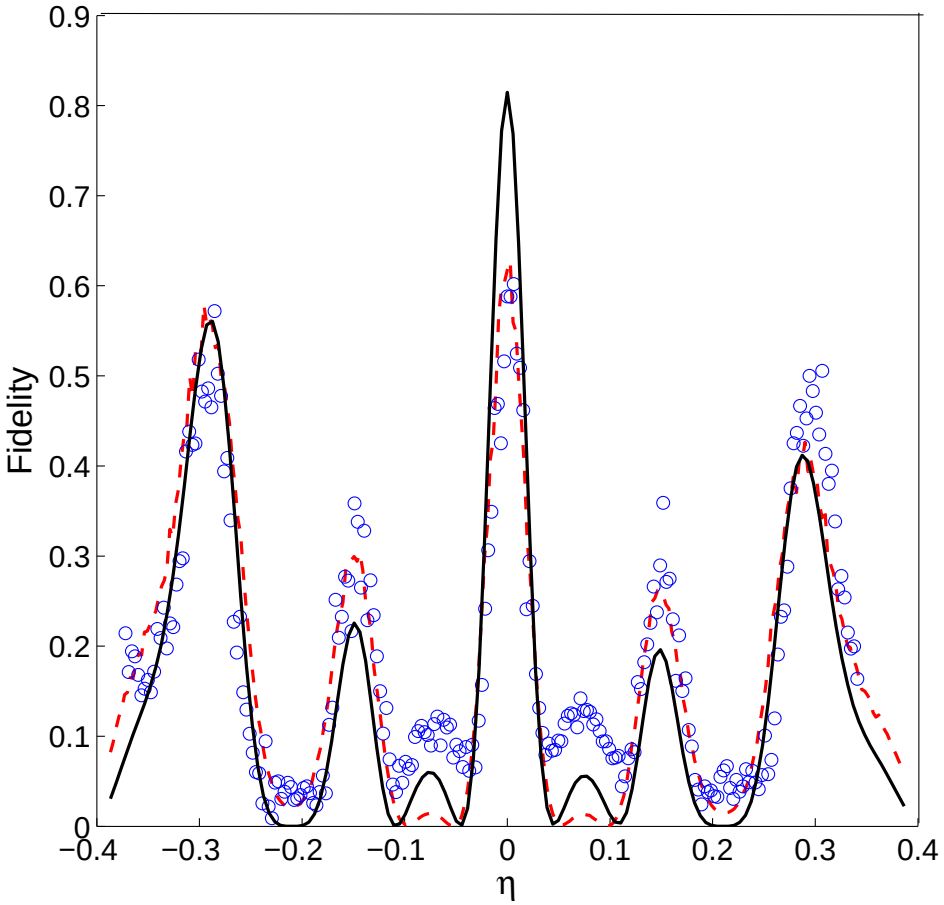

Figure 5.8: Fidelity as a function of the scaled acceleration, η, due to four kicks of strength $\phi_d \approx 0.6$ followed by a reversal kick of strength $\approx 4\phi_d$. The black solid (red dashed) line is a numerical simulation with $\tau = 2\pi$ (i.e. $\ell = 1$), $\beta = 0.5$ and initial momentum width $\Delta\beta = 0.06\hbar G$ without (with) effects such as vibrations and reversal phase imperfections (see more in the text). Circles are experimental data. Note that the fidelity has a rich structure with multiple resonant peaks. All fidelity measurements are ± 0.01.

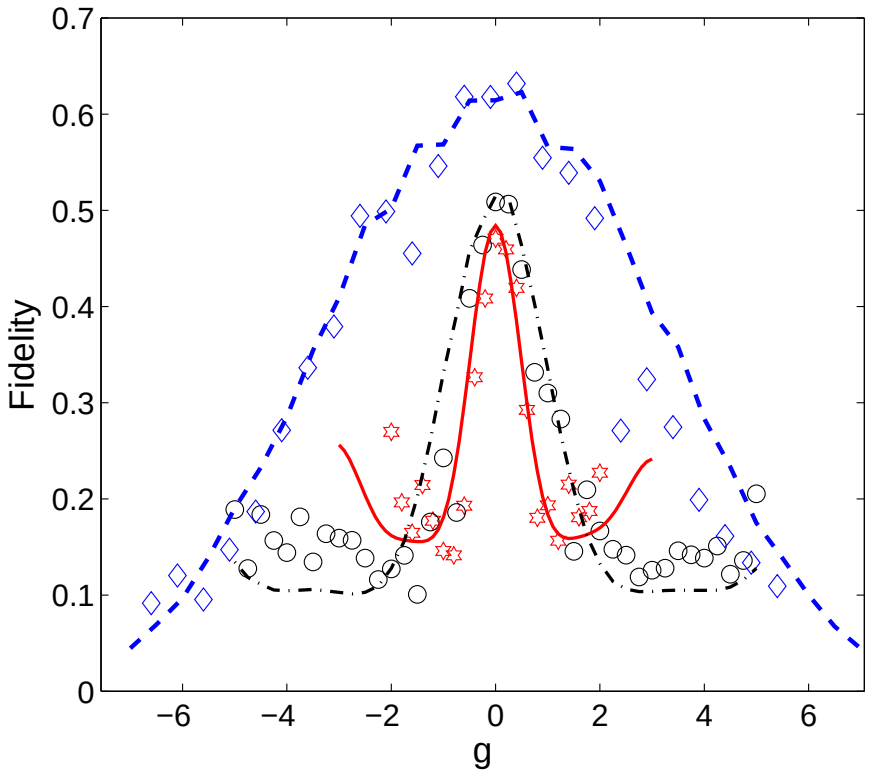

Figure 5.9: Plot showing the fidelity as a function of acceleration. Experimentally measured fidelity for $\ell = 1$ (blue diamonds), $\ell = 2$ (black circles) and $\ell = 3$ (red stars) due to four kicks of strength $\phi_d \approx 0.6$ followed by a reversal kick of strength $\approx 4\phi_d$. The lines are the corresponding fidelity from numerical simulations with $\Delta\beta = 0.06\hbar G$. Note that the horizontal axis is the real acceleration in order to show the reduction in the peak width as ℓ increases.

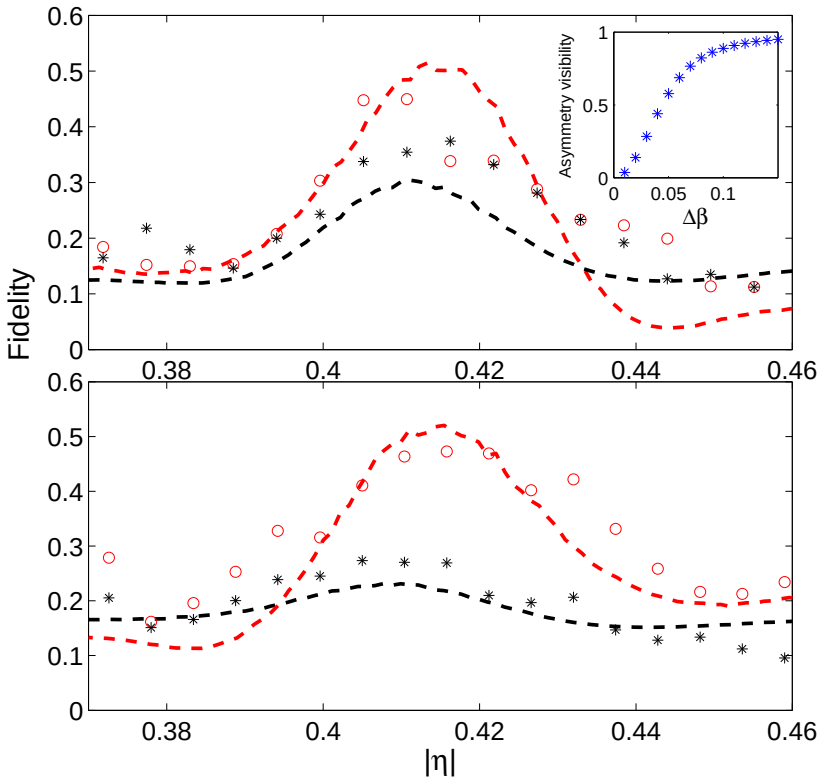

Figure 5.10: Fidelity as a function of η for $\tau = 4\pi$ and $\beta = 0.5$. Red circles and black stars represent experimental fidelity with negative and positive accelerations respectively. Panels (a) and (b) correspond to different $\Delta\beta$ (panel (b) with higher $\Delta\beta$). The measurements were done with four kicks of strength $\phi_d \approx 0.6$ followed by a reversal kick of strength $\approx 4\phi_d$. The dashed lines are the simulations for (a) $\Delta\beta = 0.06\hbar G$, and (b) $\Delta\beta = 0.07\hbar G$. The inset shows the theoretical asymmetry visibility (see text) as a function of $\Delta\beta$.

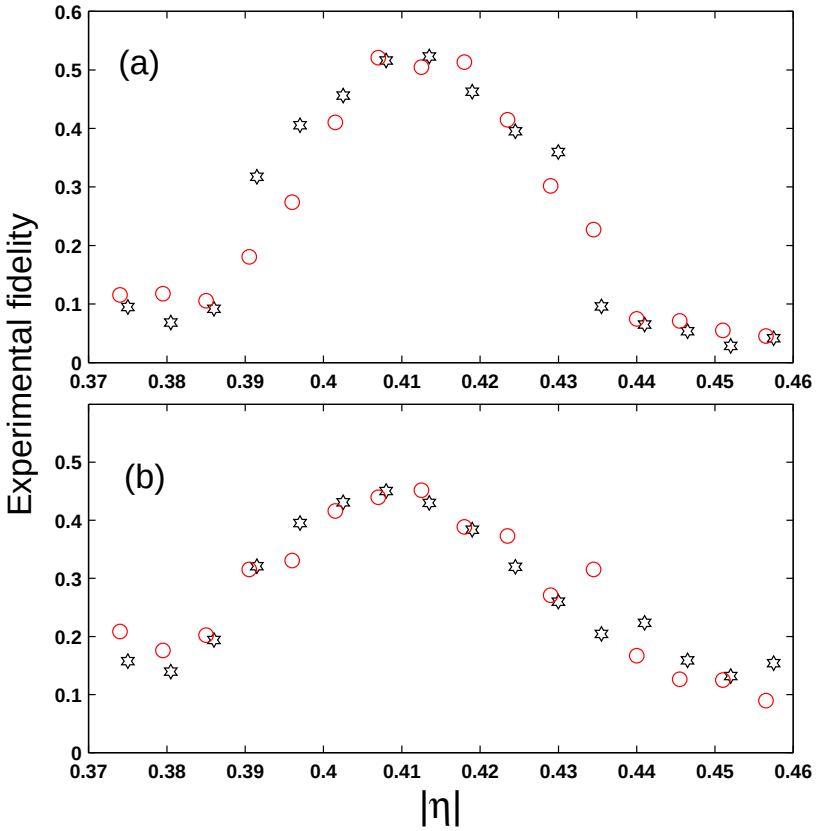

Figure 5.11: Fidelity as a function of η for $\tau = 4\pi$ and $\beta = 0$. Red circles and black stars correspond to the fidelity measured with negative and positive accelerations respectively. The measurements were done with four kicks of strength $\phi_d \approx 0.6$ followed by a reversal kick of strength $\approx 4\phi_d$. The $\Delta\beta$'s are the same as that used in Fig. 5.10. Note that in contrast to Fig. 5.10 there is no asymmetry between the positive and negative η's.

curves poor match to the experiment at the $\eta = 0$ resonance. In the simulations that follow, we will employ the method used to generate the red dashed curve (with the same parameters for the experimental imperfections). Unlike in previous work where only the central resonance was observed [88, 89], it is now possible to see that the fidelity has a more complex structure with many resonances away from $\eta = 0$. The validity of the theory for higher resonances at $\ell = 2$ and $\ell = 3$ was also tested, the results of which are presented in Fig. 5.9. Here the central fidelity resonance as a function of acceleration g is plotted. Due to the longer time available for the momentum state phases to evolve at the larger ℓ, the peaks become narrower as ℓ is increased. It is important to note that for $\ell = 2$ (Talbot time), the width (FWHM) of this peak reduces as $1/\mathrm{t}^3$ (refer to Fig. 5.6). Note that the fidelity is presented as a function of real acceleration and not η in order to show this effect.

We also examined the dependence of the fidelity to the sign of η (positive and negative acceleration). A scan was performed by changing the value of η over a large range on both sides of the resonance for two different $\Delta\beta's$. The experimentally measured fidelity is plotted as a function of $|\eta|$ in Fig. 5.10 and Fig. 5.11. When the $\beta-$rotor distribution was centered at $\beta = 0.5$ an asymmetry was observed which became more prominent as $\Delta\beta$ was increased as shown in Fig. 5.10. Note that the results correspond to pulse periods, $\tau = 4\pi$ ($\ell = 2$). This was found to lead to larger asymmetries as compared to the case of $\ell = 1$ in Fig. 5.8. The origin of the asymmetry is the different phases $\phi(\beta, \eta, \mathrm{t})$ induced by the negative and positive values of acceleration. Figure 5.10 shows the development of the asymmetry, both in the experiment and simulations, as $\Delta\beta$ is increased. The dashed lines are the plot of the simulations with $\Delta\beta = 0.06\hbar G$ and $0.07\hbar G$ (panels (a) and (b) respectively). Calculations of visibility signal for the asymmetry defined by $(F(\eta_-) - F(\eta_+))/(F(\eta_-) + F(\eta_+))$, shows an almost linear scaling with the momentum width ($\Delta\beta \leq 0.08\hbar G$) of the cloud (see inset).Thus the measurement of the asymmetry may provide a means of measuring

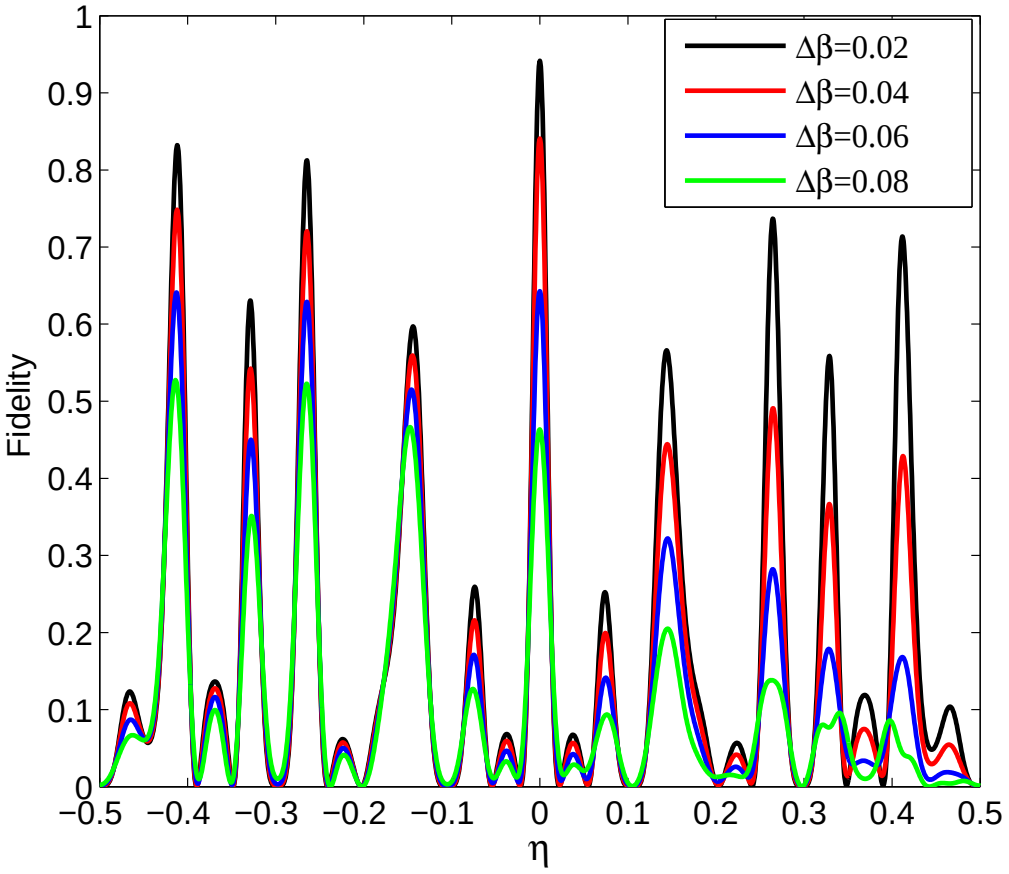

Figure 5.12: Numerical data for the fidelity due to four kicks, each of strength $\phi_d = 0.6$, followed by a reversal kick, showing the asymmetry in the fidelity with the sign of acceleration for various $\Delta\beta$. Other parameters used were $\tau = 4\pi$ and $\beta = 0.5$.

small $\Delta\beta$ and hence the temperature.

Interestingly, if the initial β distribution is chosen centered at $\beta = 0$, as is possible for $l = 2$, the asymmetry goes away. This is shown in Fig. 5.11 for the same two $\Delta\beta$'s used in Fig. 5.10. The reason behind this asymmetry is understood in terms of the initial distribution of the $\beta-$ rotors. For the case of a distribution centered at $\beta = 0$, the distribution is symmetric so that the distribution on the negative side is identical to that on the positive side. Thus changing the sign of the acceleration, η, has no effect on the dynamics or in other words the effect of changing the sign of acceleration or the sign of β will have same effect and there is no asymmetry. However with the β distribution centered at any value other than zero, the distribution is no longer symmetric and the effect of η will be different for each half of the β distribution. This causes an asymmetry and will be maximized when $\beta = 0.5$. A numerical calculation of fidelity (in which the reversal pulse is perfect in amplitude (amplitude = $t\phi_d$) and there are no random phase variations in the standing wave that could be caused by vibrations of the optics used to form it) as a function of η for different $\Delta\beta$ is plotted in Fig. 5.12. As expected, the asymmetry increases as $\Delta\beta$ gets larger.

In conclusion, we performed an experimental investigation on the sensitivity of the fidelity to the acceleration by exposing a BEC to a set of δ-kicked rotor optical pulses followed by a stronger reversal pulse. The experimental results and analytical theory were in good agreement, with both showing the presence of multiple fidelity resonances. The width of the central fidelity resonance was found to become narrower as the pulse period increased. The importance of the position of the center of the initial momentum distribution was also explored. When the distribution was centered at some values other than zero, an asymmetry between the fidelity at positive and negative values of acceleration was observed which became more prominent with increasing $\Delta\beta$. The asymmetry was maximized for a distribution centered at $\beta = 0.5$, disappearing almost completely when the distribution was centered at $\beta = 0$.

These findings may be useful in determining externally applied accelerations and the temperature of ultracold atoms.

CHAPTER 6

The quantum ratchet

A ratchet is a mechanical device that allows motion in only one direction. The concept of classical ratchet was discussed by Feynman in his famous lectures on physics [97]. He demonstrated how random thermal noise could be used to extract useful work after cleverly designing a device called a "ratchet and pawl". However if the system is in thermal equilibrium, no useful work can be extracted according to the second law of thermodynamics. Thus the combination of non-equilibrium and an asymmetry generally leads to a ratchet effect [98–102]. The basic idea is that the system which is not in thermal equilibrium tends towards equilibrium. If the system is asymmetric, then moving towards equilibrium will usually involve spatial movement. In order to keep the system moving, it is necessary to perpetually keep it away from thermal equilibrium, this costs energy and this is the energy that drives the motion. An example of this is a flashing ratchet [103] (Fig. 6.1). Here Brownian particles are trapped in a periodic, asymmetric (sawtooth-like) potential that can be turned on and off. When the potential is off the particles undergo random diffusion which is converted into a net motion to the left by the asymmetry. Some of the interesting applications of a classical ratchet are a flow of current without bias voltage in a metal [104] and some biological motors [105, 106] which can use thermal fluctuations to establish particle current. Classical ratchets require dissipative energy to produce a directed transport.

A quantum ratchet is a Hamiltonian ratchet (no dissipation) and has no classical analog. It is manifested by a directed current of particles in the absence of net bias

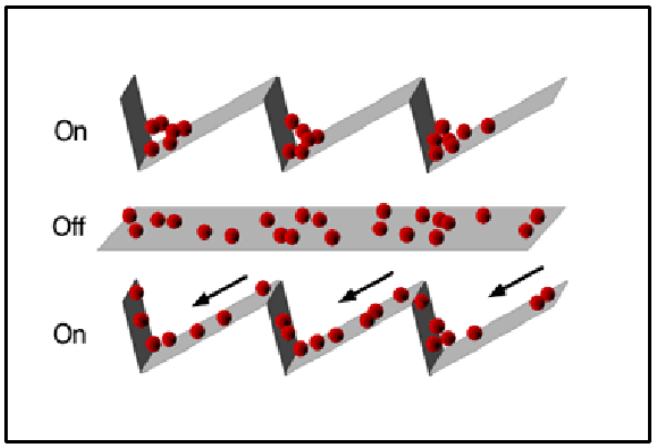

Figure 6.1: The flashing ratchet. The sawtooth-like potential is periodically switched on and off. The particles subjected to Brownian motion are on average transported in a specific direction (towards the left in the picture) by the asymmetric potential.

forces and has been extensively studied theoretically and experimentally [60–67]. The basic idea behind the quantum ratchet effect due to a sinusoidal periodic potential is that the initial atomic distribution experiences a force from the potential gradient. The net force on the distribution equals zero (as shown in panel (a) and (b) in Fig. 6.2) when the initial distribution is symmetric with respect to the potential, so that the ratchet effect does not appear. However in the case of the non-coincidence of the symmetry centers of the atomic state and the potential (panel (c) in Fig. 6.2), the atoms experience a net force due to the potential gradient thus causing an atomic ratchet effect. Such a ratchet phenomenon is discussed in Section 6.1 at QR and the away from resonance case is discussed in Section 6.2.

6.1 Ratchet at resonance: a quantum treatment

In order to create a ratchet we start with an initial state that is a superposition of two plane waves. The potential and the particle distributions are shown in Fig. 6.2 (a)-(c), where γ is the offset phase. As described earlier, the atoms can experience a net force due to the potential gradient. To understand the theoretical basis for this process, consider an initial state given by

$$|\psi_0\rangle = \frac{1}{\sqrt{2}}\left[|0\hbar G\rangle + e^{i\gamma}|1\hbar G\rangle\right], \tag{6.1}$$

this is equivalent to the rotor state

$$|\psi_0(\theta)\rangle = \frac{1}{\sqrt{4\pi}}[1 + e^{i(\theta+\gamma)}]. \tag{6.2}$$

Here γ is an additional phase used to account for the fact that the initial atomic distribution is shifted in position relative to the applied periodic potential. As discussed earlier, the dynamics of the kicked rotor system can be described by the Hamiltonian (3.10) which in dimensionless units is

$$\mathcal{H} = \frac{\hat{p}^2}{2} + \phi_d \cos(\hat{X}) \sum_{q=1}^{\mathrm{t}} \delta(t - q\tau). \tag{6.3}$$

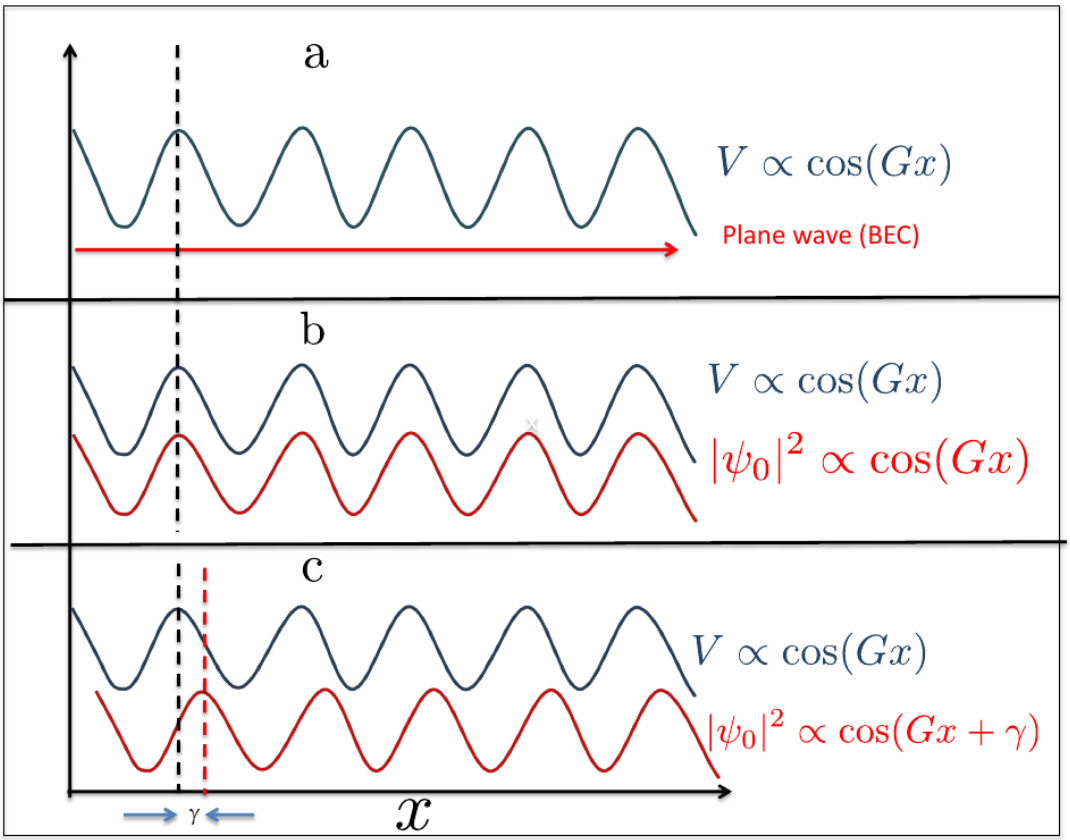

Figure 6.2: Picture of the potential and initial atomic state distribution. In panels (a) and (b) the net forces experienced by the state from the potential gradient is zero. Thus the directed motion of the atoms are not possible. However due to the non-coincidence of the symmetry centers in panel (c), the state experiences a net force which causes a directed motion of the atoms to the right.

Since the momentum in this system is only changed in quanta of $\hbar G$, we break down $\hat{p}$ as $\hat{p} = \hat{\mathcal{N}} + \beta$ where $\hat{\mathcal{N}} = -i\frac{\mathrm{d}}{\mathrm{d}\theta}$ is the angular momentum operator with an eigenvalue n, and β (the quasi-momentum) is conserved. Here $\hat{\theta} = \hat{X} \mod (2\pi)$. The one step evolution operator for this Hamiltonian is given by

$$\begin{aligned}\hat{\mathcal{U}}_\beta &= e^{-i\phi_d \cos(\hat{\theta}+\gamma)} e^{-i(\hat{\mathcal{N}}+\beta)^2 \frac{\tau}{2}} \\ &= e^{-i\phi_d \cos(\hat{\theta}+\gamma)} e^{-i\pi\ell(\hat{\mathcal{N}}^2 + 2\hat{\mathcal{N}}\beta + \beta^2)} \\ &= e^{-i\phi_d \cos(\hat{\theta}+\gamma)} e^{-i\hat{\mathcal{N}}\tau_\beta},\end{aligned} \tag{6.4}$$

where $\tau_\beta = \pi\ell(2\beta + 1)$ with ℓ an integer and the irrelevant phase factor $e^{-i\pi\ell\beta^2}$ has been ignored. In the last step, the relation $e^{-i\pi\ell n^2} = e^{-i\pi\ell n}$ is also used. The mean momentum after time q is given by [61]

$$\langle \hat{\mathcal{N}} \rangle = \langle \psi_q | \hat{\mathcal{N}} | \psi_q \rangle \tag{6.5}$$

where the rotor state after q kicks can be explicitly calculated as,

$$\begin{aligned}\psi_q(\theta) &= \hat{\mathcal{U}}_\beta^q \psi_0(\theta) \\ &= \hat{\mathcal{U}}_\beta^{q-1} e^{-i\phi_d \cos(\hat{\theta}+\gamma)} \psi_0(\theta - \tau_\beta) \\ &= \hat{\mathcal{U}}_\beta^{q-2} e^{-i\phi_d \cos(\hat{\theta}+\gamma)} e^{-i\phi_d \cos(\hat{\theta}+\gamma-\tau_\beta)} \psi_0(\theta - 2\tau_\beta) \\ &= e^{-i\phi_d \sum_{s=0}^{q-1} \cos(\hat{\theta}+\gamma-s\tau_\beta)} \psi_0(\theta - q\tau_\beta).\end{aligned}$$

Using the geometric series relation $\sum_{s=0}^{q-1} e^{as} = \frac{1-e^{aq}}{1-e^a}$ we get

$$\psi_q(\theta) = e^{\left[-i\phi_d \frac{\sin(q\tau_\beta/2)}{\sin(\tau_\beta/2)} \cos[\theta - (q-1)\frac{\tau_\beta}{2} + \gamma]\right]} \psi_0(\theta - q\tau_\beta). \tag{6.6}$$

Now applying Eq. (6.6) and the definition of $\hat{\mathcal{N}}$, Eq. (6.5) gives

$$\begin{aligned}
\langle\hat{\mathcal{N}}\rangle_q &= -i\int_0^{2\pi}\psi_q^*(\theta)\frac{\mathrm{d}\psi_q(\theta)}{\mathrm{d}\theta}\mathrm{d}\theta \\
&= -i\int_0^{2\pi}[i\phi_d\frac{\sin(q\tau_\beta/2)}{\sin(\tau_\beta/2)}\sin\{\theta-(q-1)\frac{\tau_\beta}{2}+\gamma\}|\psi_0(\theta-q\tau_\beta)|^2 \\
&\quad + \psi_0^*(\theta-q\tau_\beta)\frac{\mathrm{d}\psi_0(\theta-q\tau_\beta)}{\mathrm{d}\theta}]\mathrm{d}\theta \\
&= -i\int_0^{2\pi}\left[i\phi_d\frac{\sin(q\tau_\beta/2)}{\sin(\tau_\beta/2)}\sin\{\theta-(q-1)\frac{\tau_\beta}{2}+\gamma\}|\psi_0(\theta-q\tau_\beta)|^2\right]\mathrm{d}\theta \\
&\quad + \langle\hat{\mathcal{N}}\rangle_0. \qquad (6.7)
\end{aligned}$$

The momentum current, also called a ratchet current, is defined as the change in the mean momentum at any time relative to its initial value. Mathematically it is given by [61, 64]

$$\begin{aligned}
\Delta\langle\hat{p}\rangle_q &= \langle\hat{\mathcal{N}}\rangle_q - \langle\hat{\mathcal{N}}\rangle_0 \\
&= \frac{\phi_d}{2}\frac{\sin(q\tau_\beta/2)}{\sin(\tau_\beta/2)}\sin\left[(q+1)\frac{\tau_\beta}{2}+\gamma\right]. \qquad (6.8)
\end{aligned}$$

It can be seen clearly that if an initial state is a plane wave, the integral in Eq. (6.7) vanishes and there will be no ratchet current. This is a justification of why a special initial state is required to produce ratchet current. For $\tau_\beta = 2\pi r$, r is an integer, Eq. (6.8) reduces to

$$\Delta\langle\hat{p}\rangle_{q,r} = -\frac{\phi_d}{2}\sin(\gamma)q \qquad (6.9)$$

which shows a linear growth of current in time. This theory has been extended to the general case which considers the finite width of initial momentum $\Delta\beta$ which is a more realistic model of the experiments [30, 31, 61]. This assumes a condensate as a mixture of quasimomenta β' with a Gaussian distribution centered at β given by [61]

$$\Gamma_{\beta,\Delta\beta}(\beta') = \frac{1}{\sqrt{2\pi(\Delta\beta)^2}}\exp\left[\frac{-(\beta'-\beta)^2}{2(\Delta\beta)^2}\right] \qquad (6.10)$$

Then the expressions for momentum current given by Eqs. (6.8) and (6.9) takes the following forms:

$$\langle \Delta\langle \hat{p}\rangle_q\rangle_{\Delta\beta} = \frac{\phi_d}{2}\sum_{s=1}^{q}\sin(s\tau_\beta+\gamma)\exp[-2(\pi\ell\Delta\beta s)^2] \tag{6.11}$$

and

$$\langle \Delta\langle \hat{p}\rangle_q\rangle_{r,\Delta\beta} = -\frac{\phi_d}{2}\sin(\gamma)\sum_{s=1}^{q}\exp[-2(\pi\ell\Delta\beta s)^2. \tag{6.12}$$

6.1.1 Experimental configuration and results

The experimental details and the results on the ratchet phenomenon at QR are presented in references [30,31,61]. As explained in the following section, the initial state was prepared as a superposition of two momentum states $|p = 0\hbar G\rangle$ and $|p = 1\hbar G\rangle$ and the experiments were performed by using the pulse scheme as shown in Fig. 6.3. The main results are presented in Fig. 6.4 and 6.5. The mean momentum of the kicked BEC was experimentally measured as a function of several variables. Figure 6.4 shows the dependence of mean momentum on the phase γ for resonant $\beta = 0.5$ after 5 kicks. The maximum value of mean momentum was achieved for $\gamma = \pi/2$ as suggested by the theory. The dependence of mean momentum current on quasi-momentum β for $\gamma = \pi/2$ and $\gamma = -\pi/2$ are shown in Fig. 6.5(a) and (b) respectively. The mean momentum is a maximum at $\beta = 0.5$ in both panels. In both figures, the dashed line is a plot of Eqs. (6.8) and the solid line is a plot of Eq. (6.12) with initial momentum width of $\Delta\beta = 0.056$. The ratchet effect is found to be suppressed by the width in the initial momentum distribution. The error bars in both figures correspond the standard deviation from three sets of experiments.

In summary, a quantum-resonance ratchet was realized by applying pulses from a symmetric optical potential to a superposition of two momentum states. The ratchet current was created by the asymmetry between the center of the kicking potential and the initial distribution. The ratchet current was a maximum at $\gamma = \pm\pi/2$ and

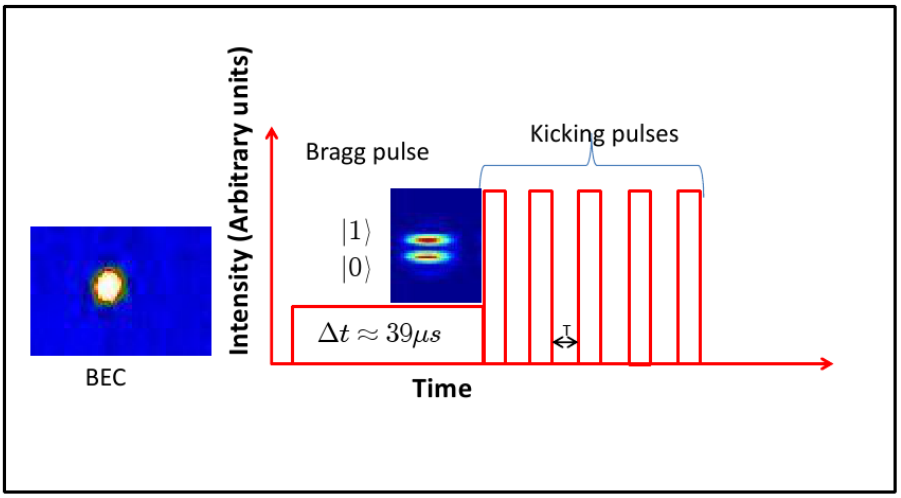

Figure 6.3: Initial state preparation for the ratchet experiment. A long, weak intensity Bragg pulse creates a superposition of two momentum states with an equal population. The kicking pulses were applied immediately after the Bragg pulse

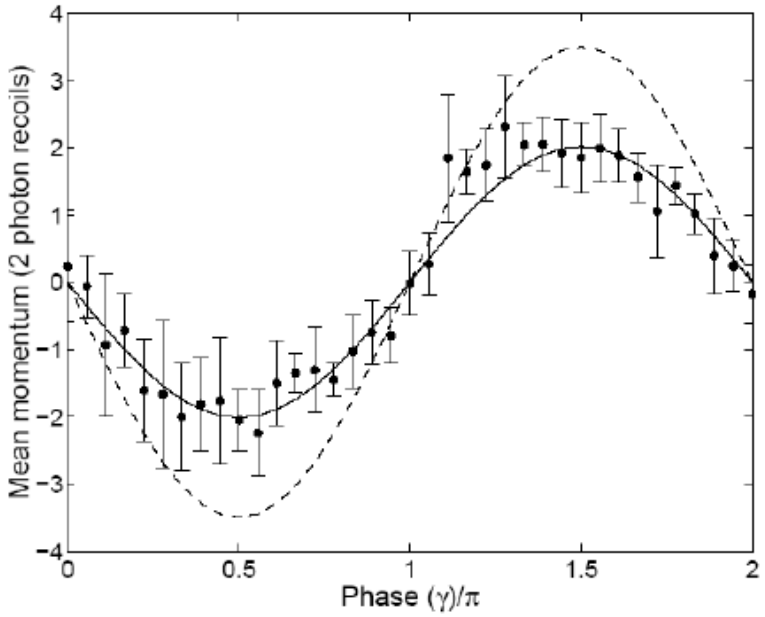

Figure 6.4: Change in mean momentum as a function of phase angle γ after 5 kicks each of strength $\phi_d = 1.4$ and resonant quasimomentum $\beta = 0.5$. The filled circles with associated error bars are from the experiment. The dashed line is the plot of Eq. (6.8) and the solid line is the plot of Eq. (6.12) with $\Delta\beta = 0.056$.

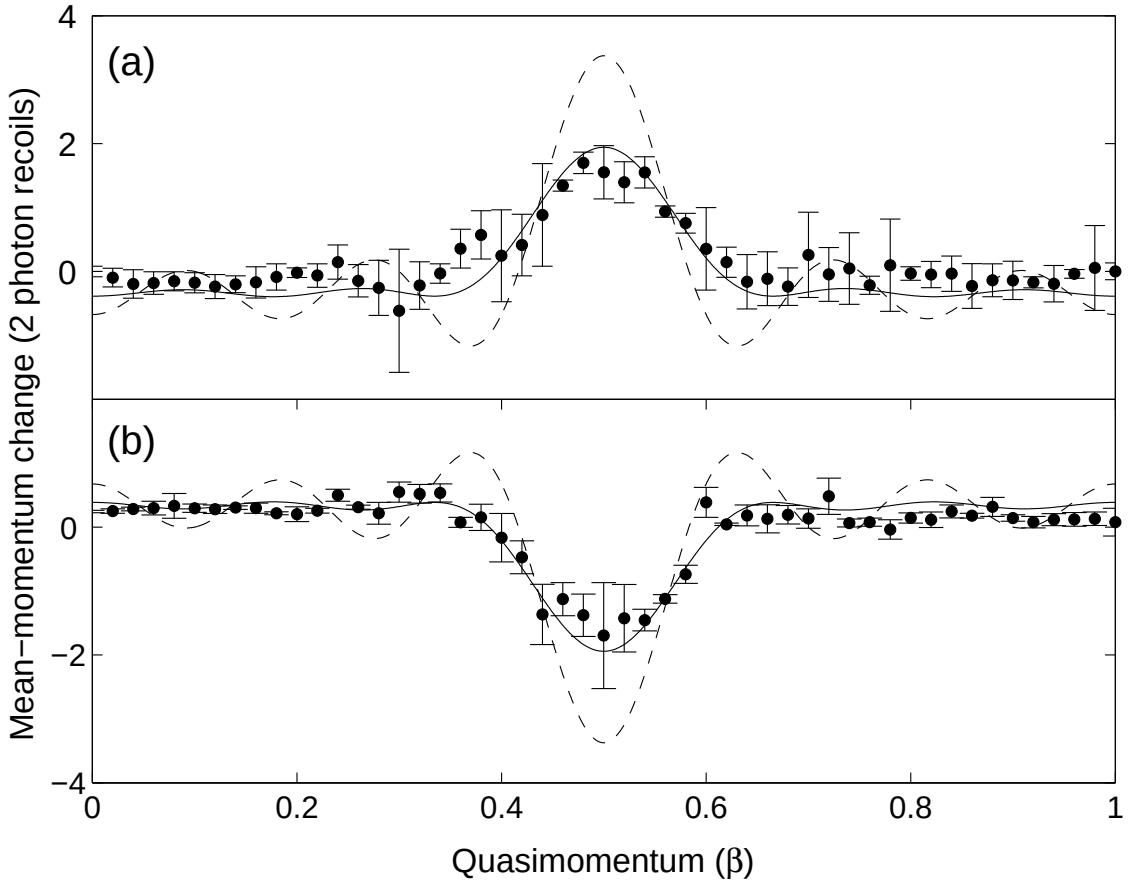

Figure 6.5: Plot of change in mean momentum as a function of quasimomentum β after 5 kicks each of kick strength $\phi_d = 1.4$ for (a) $\gamma = -\pi/2$ and (b) $\gamma = \pi/2$. The filled circles with error bars are the experimental data. The dashed line and the solid lines are plot of Eqs. (6.8) and (6.12) with $\Delta\beta = 0.056$.

$\beta = 0.5$, and was suppressed by an initial momentum width $\Delta\beta$.

6.2 Off-resonant ratchet: a classical treatment

We now discuss the ratchet phenomenon away from quantum resonance. The question of what happens to a ratchet in this regime was addressed in a recent theoretical paper [107]. In that work, the authors developed a classical-like theory and proposed the existence of a one-parameter scaling law that could be used to predict the ratchet current for a wide variety of parameters. It was also shown that an *inversion* of the momentum current might be possible for some sets of scaling variables. In this section, we discuss the experimental observation of such an inversion and the verification of the scaling law for a wide variety of experimental parameters. Moreover the cross over between the classical and the quantum regimes can also be studied using the off-resonant ratchet effect.

The dynamics of the AOQKR system can be described using the Hamiltonian of Eq. (6.1). A successful approach to treating this system close to resonant values of τ (i.e. $\tau = 2\pi\ell$, with $l > 0$ integer) is the so called $\varepsilon-$classical theory. Here the scaled pulse period is written as $\tau = 2\pi\ell + \varepsilon$, where $|\varepsilon| \ll 1$, and can be shown to play the role of Planck's constant. In this case the dynamics can be understood by the classical mapping (3.33),

$$J_{q+1} = J_q + \tilde{k}\sin(\theta_{q+1}), \quad \theta_{q+1} = \theta_q + J_q, \tag{6.13}$$

where $\tilde{k} = |\varepsilon|\phi_d$ is the scaled kicking strength, $J_q = \varepsilon p_q + \ell\pi + \tau\beta$ is the scaled momentum variable and $\theta_q = X \mod (2\pi) + \pi[1 - \mathrm{sign}(\varepsilon)]/2$ is the scaled position exploiting the spatial periodicity of the kick potential. As mentioned previously, in order to create the ratchet we start with a superposition of plane waves $|\psi_0\rangle = \frac{1}{\sqrt{2}}\left[|0\hbar G\rangle + e^{i\gamma}|1\hbar G\rangle\right]$, or equivalently a rotor state $\frac{1}{\sqrt{4\pi}}[1 + e^{i(\theta+\gamma)}]$. This leads to the position space probability distribution function

$$P(\theta) = |\psi(\theta)|^2$$
$$= \frac{1}{2\pi}[1 + \cos(\theta + \gamma)]. \tag{6.14}$$

Here γ is an additional phase used to account for the possibility that the initial spatial atomic distribution is shifted in position relative to the applied periodic potential. Although the distribution $P(\theta)$ is quantum in origin, in what follows it will be interpreted as a classical probability.

The original application of $\varepsilon-$classical theory to the kicked rotor system showed the existence of a one-parameter scaling law for the mean energy [94]. This was experimentally verified in the vicinity of the first and second quantum resonances ($\ell = 1$ and $\ell = 2$) in Ref. [108]. It was found that the scaled energy could be written as

$$\frac{E}{\phi_d^2 q} = 1 - \Phi_0(x) + \frac{4}{\pi x} G(x) \tag{6.15}$$

where $x = \sqrt{\phi_d|\varepsilon|}\, q$ is a scaling variable and $\Phi_0(x)$ and $G(x)$ are closed form functions of x. The existence of a one-parameter scaling law for the ratchet current using the same scaling parameter x was proposed [107]. In what follows the consequences of such an assumption are explored and shown to lead to the possibility of current reversals for some values of x.

To begin the theoretical discussion we make the pendulum approximation [109] in which the motion of the kicked rotor in continuous time is described by the scaled Hamiltonian

$$H' \approx (J')^2/2 + |\varepsilon|\phi_d \cos(\theta), \tag{6.16}$$

where $J' = J/(\sqrt{\phi_d|\varepsilon|})$ is a scaled momentum variable. Near the quantum resonance, using the position space probability distribution function $P(\theta)$, one can calculate the

ratchet current, $\langle J' - J'_0 \rangle$, as

$$\langle J' - J'_0 \rangle = \int_{-\pi}^{\pi} d\theta_0 P(\theta_0)(J' - J'_0). \tag{6.17}$$

For $|\varepsilon| \lesssim 1$, Eq. (6.13) gives a phase space dominated by a pendulum-like resonance island of extension $4\sqrt{\tilde{k}} \gg |\varepsilon|$ [94]. Hence $p = 0$ and $p = 1$ essentially contribute in the same way giving $J'_0 = 0$ so that the map (6.13) can be rewritten as

$$J'_{q+1} = \sqrt{\tilde{k}} \sum_{q=0}^{\mathrm{t}-1} \sin(\theta_{q+1}). \tag{6.18}$$

Using Eq. (6.14) and scaling variable x, Eq. (6.17) becomes

$$\begin{aligned}
\langle J' - J'_0 \rangle =& \frac{1}{2\pi} \int_{-\pi}^{\pi} \mathrm{d}\theta_0 [1 + \cos(\theta_0 + \gamma)] J'(\theta_0, J_0 = 0, x) \\
=& \frac{1}{2\pi} \int_{-\pi}^{\pi} \mathrm{d}\theta_0 J'(\theta_0, J_0 = 0, x) + \frac{1}{2\pi} \cos\gamma \int_{-\pi}^{\pi} \cos\theta_0 \mathrm{d}\theta_0 J'(\theta_0, J_0 = 0, x) \\
& - \frac{1}{2\pi} \sin\gamma \int_{-\pi}^{\pi} \sin\theta_0 \mathrm{d}\theta_0 J'(\theta_0, J_0 = 0, x) \\
=& - \sin\gamma \frac{1}{2\pi} \int_{-\pi}^{\pi} \sin\theta_0 \mathrm{d}\theta_0 J'(\theta_0, J_0 = 0, x) \\
=& - \sin\gamma F(x).
\end{aligned} \tag{6.19}$$

Here the integrals in the first and second term at the second step vanish due to the fact that J' is an odd function. We also define

$$F(x) = \frac{1}{2\pi} \int_{-\pi}^{\pi} \sin\theta_0 J'(\theta_0, J'_0 = 0, x) d\theta_0. \tag{6.20}$$

Thus the mean momentum (units of $\hbar G$) expressed in terms of the scaled variables is

$$\begin{aligned}
\langle p \rangle =& \sqrt{\frac{\phi_d}{|\varepsilon|}} \langle J' - J'_0 \rangle = -\frac{\phi_d t \sin\gamma}{x} F(x) \\
\frac{\langle p \rangle}{-\phi_d q \sin\gamma} =& \frac{F(x)}{x}
\end{aligned} \tag{6.21}$$

where $F(x)$ can be computed from the pendulum approximation [107].

6.2.1 Experimental configuration and results

We now discuss the experiments that were carried out to observe the ratchet effect away from resonance. Mostly the underlying setup was very similar to that used to measure fidelity (Sec. 5.1.1). Nevertheless there were some important differences so the full setup is described. The experiments used the setup shown in Fig. 4.11. A BEC of about 40000 ^{87}Rb atoms was created in the $5S_{1/2}$, $F = 1$ level using an all-optical trap technique. Approximately 5 ms after being released from the trap, the condensate was exposed to a pulsed horizontal standing wave of wavelength λ_G. This was formed by two laser beams of wavelength $\lambda = 780$ nm, detuned 6.8GHz to the red of the atomic transition. The direction of each beam was aligned at 53^o to the vertical to give $\lambda_G = \lambda/(2\sin 53^o)$. With these parameters the primary QR (half-Talbot time [57,79,80]) occurred at multiples of 51.5 ± 0.05 μs. Each laser beam was passed through an acousto-optic modulator driven by an arbitrary waveform generator. This enabled control of the phase, intensity, and pulse length as well as the relative frequency between the kicking beams. Adding two counterpropagating waves differing in frequency by Δf resulted in a standing wave that moved with a velocity $v = 2\pi\Delta f/G$. The initial momentum or quasi-momentum β of the BEC relative to the standing wave is proportional to v, so that by changing Δf the value of β could be systematically controlled. The kicking pulse length was fixed at 1.54 μs, so we varied the intensity rather than the pulse length to change the kicking strength ϕ_d. This was done by adjusting the amplitudes of the RF waveforms driving the kicking pulses, ensuring that the experiments were performed in the Raman-Nath regime (the distance an atom travels during the pulse is much smaller than the period of the potential).

The initial state for the experiment was prepared as a superposition of two momentum states $|p = 0\hbar G\rangle$ and $|p = 1\hbar G\rangle$ by applying a long ($\Delta t = 38.6\mu$s) and very weak standing wave pulse (Bragg pulse). By using a pulse of suitable strength,

an equal superposition of the two aforementioned external atomic states was created ($\pi/2$ pulse). The Bragg pulse was immediately followed by the kicking pulses in which a relative phase of γ between the beams was applied. This phase was experimentally controlled by adjusting the phase difference between the RF waveforms driving the two AOMs. The schematic of the pulse sequences to prepare the initial superposition state and to create the ratchet current is shown in Fig. 6.3. Finally the kicked atoms were absorption imaged after 9 ms using a time-of-flight measurement technique to yield momentum distributions like those seen in Fig. 6.6.

Figure 6.6 shows raw momentum distributions as a function of the pulse period's offset from the first QR and the kick number (Fig. 6.6 (a) and (b) respectively). It can be seen that there are certain values of time offset and kick number where the distribution is weighted more strongly towards negative momentum. This is evidence of a current reversal. Furthermore, Fig. 6.6 (a) and (b) contain other similarities. For example, there are parameter regimes where the momentum distributions tend strongly towards positive momenta, followed by the current reversal regions where the distributions tend negative. This suggests a link to the single-parameter ratchet theory described in Section 6.2. Moreover, since the time offset from QR effectively defines a new Planck constant [69, 94], we can easily switch from the classical to the quantum regime by a simple change of the pulse period. This allows for the study of the crossover between classical and quantum dynamics.

The measurements involve the determination of the mean momentum of kicked BECs for various combinations of the parameters q, ϕ_d, ε and γ. The measured momentum was then scaled by $-\phi_d q \sin\gamma$ and is plotted as a function of the scaling variable x for $\ell = 1$ in Fig. 6.7 and for $\ell = 0$ in Fig. 6.8. In Fig. 6.7(a) and Fig. 6.8, x was changed by varying kick number, q, while in Fig. 6.7(b) different x were obtained by scanning either $|\varepsilon|$ (red circles and green squares) or ϕ_d (blue triangles). The solid line in both panels is a plot of the function $\frac{F(x)}{x}$ given by Eq. (6.21). It can be seen

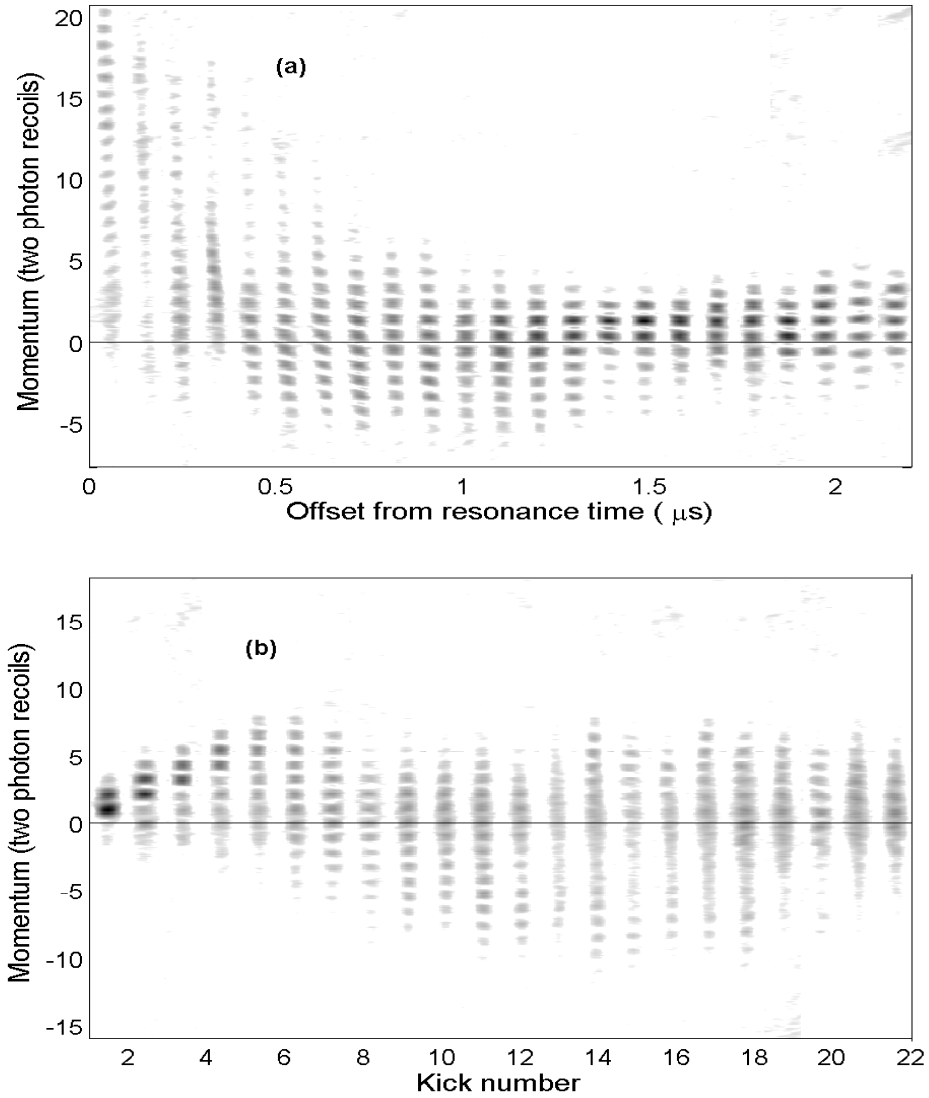

Figure 6.6: Experimental momentum distributions after exposing a BEC to short pulses of an off-resonant standing wave of light. The momentum distributions are shown as a function of (a) pulse period offset from resonance (μs) (10 kicks, $\phi_d = 2.6$, $\gamma = -\pi/2$), and (b) kick number ($|\varepsilon| = 0.18$, $\phi_d = 1.8$ and $\gamma = -\pi/2$.). Each momentum distribution was captured in a separate time-of-flight experiment.

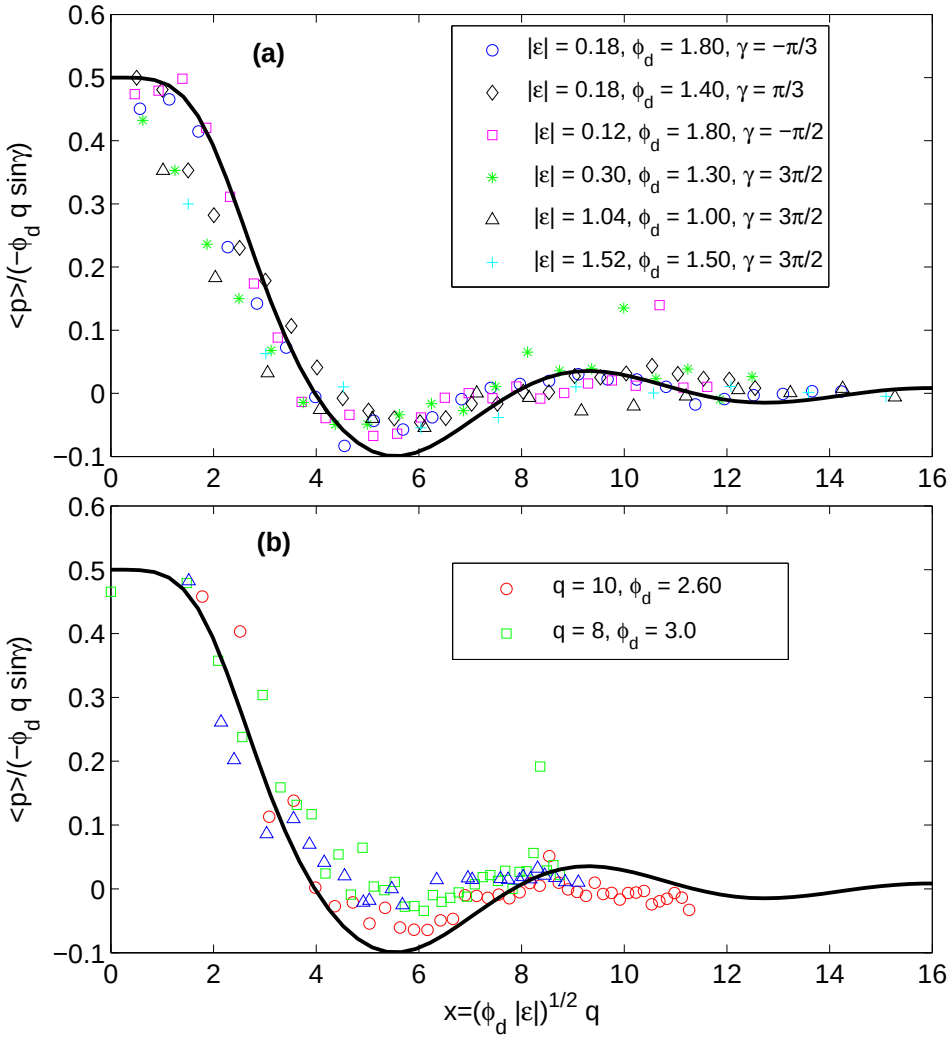

Figure 6.7: Scaled mean momentum $\langle p\rangle/(-\phi_d q \sin\gamma)$ as a function of the scaling variable $x = \sqrt{(\phi_d|\varepsilon|)}\; q$. The data were taken away from QR ($\ell = 1$). In (a) x was varied by scanning over kick number for different combinations of ϕ_d, $|\varepsilon|$ and γ. In panel (b) x was varied by scanning over $|\varepsilon|$ with $q = 8$, $\phi_d = 3.0$ (green squares), and with $q = 10$, $\phi_d = 2.6$ (red circles). Also plotted in (b) is data from a scan over ϕ_d with $|\varepsilon| = 0.18$, $q = 8$ (blue triangles). In both panels, the solid line is the function $F(x)/x$ given by Eq. (6.21). This demonstrates that no matter how x is obtained, the scaled mean momentum is approximately universal.

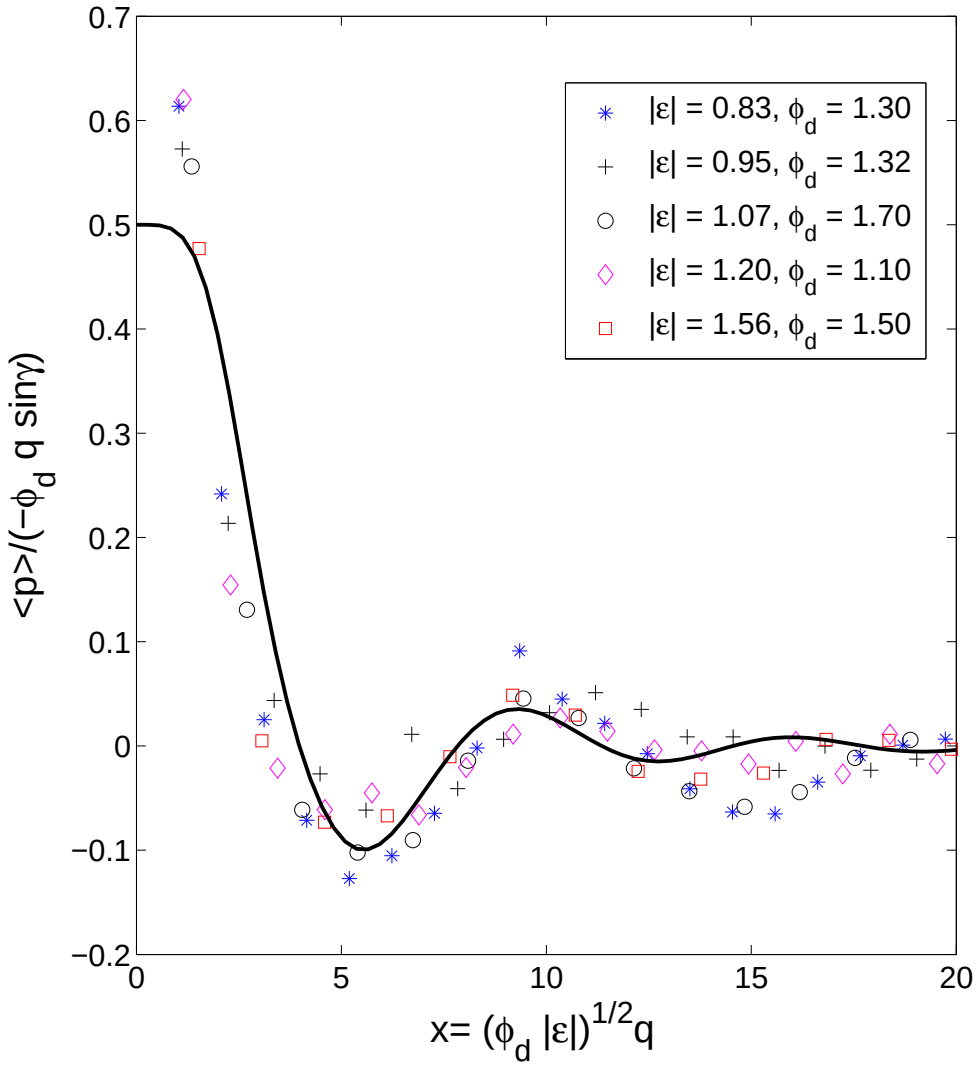

Figure 6.8: Scaled mean momentum $\langle p\rangle/(-\phi_d q \sin\gamma)$ as a function of the scaling variable $x = \sqrt{(\phi_d|\varepsilon|)}\ q$. The data were taken away from $\ell = 0$, the true classical regime. x was varied by scanning over kick number for different combinations of ϕ_d, $|\varepsilon|$ and $\gamma = -\pi/2$. The solid line is the function $F(x)/x$ given by Eq. (6.21).

that no matter how x is varied, the experimental results are in good agreement with the theory for many different combinations of parameters. An exception to this is seen in Fig. 6.8 at high x values. We postulate that this could be due to the lack of precision in the measurement of the kick strength. In addition, there is a regime over x where an inversion of the ratchet current takes place, with a maximum inversion at $x \approx 5.6$. Interestingly this reversal of the ratchet takes place without altering any of the centers of symmetry of the system. Even though the $\varepsilon-$classical theory assumes $|\varepsilon|$ is small, the experimental results show that it remains valid for higher values of $|\varepsilon|$ as well. This is also the case in the true classical regime near $\ell = 0$. In fact the window of valid $|\varepsilon|$ depends on the kick number [94], being rather large for small $q \lesssim 10 - 15$. This is expected from a Heisenberg/Fourier argument [108, 110, 112].

Since the time offset from QR effectively defines a new Planck constant [69, 94], we can easily switch from the classical to the quantum regime by a simple change of the pulse period. Figure 6.9 is a false color plot of scaled mean momentum for the pulse periods starting from close to true classical limit ($\ell = 0$) up to the first quantum resonance ($\ell = 1$). The data were collected by scanning over the kick number for the different pulse periods. The data presentation is such that the scaling variable x is on the $x-$axis, pulse periods are on the $y-$axis and the mean momentum is plotted on the color axis. The deep blue color represents negative scaled mean momentum. It can be clearly seen that, when the pulse periods are closer to the classical limit, $\tau = 0$ (bottom of the $y-$axis) and to the first quantum resonance $\tau = 2\pi$ i.e. $T = 51.5\mu$s (top of the $y-$axis), an inversion of the momentum current is present. However the inversion becomes weak and disappears far away from either end (in the middle). Also visible near $\tau = 0$ is a second region of inversion around $x = 15$. This is the same as the second inversion seen in Fig. 6.8.

If a ratchet is to be used to transfer momentum, an important question is, how sensitive will the momentum transfer be to an unavoidable finite spread in initial

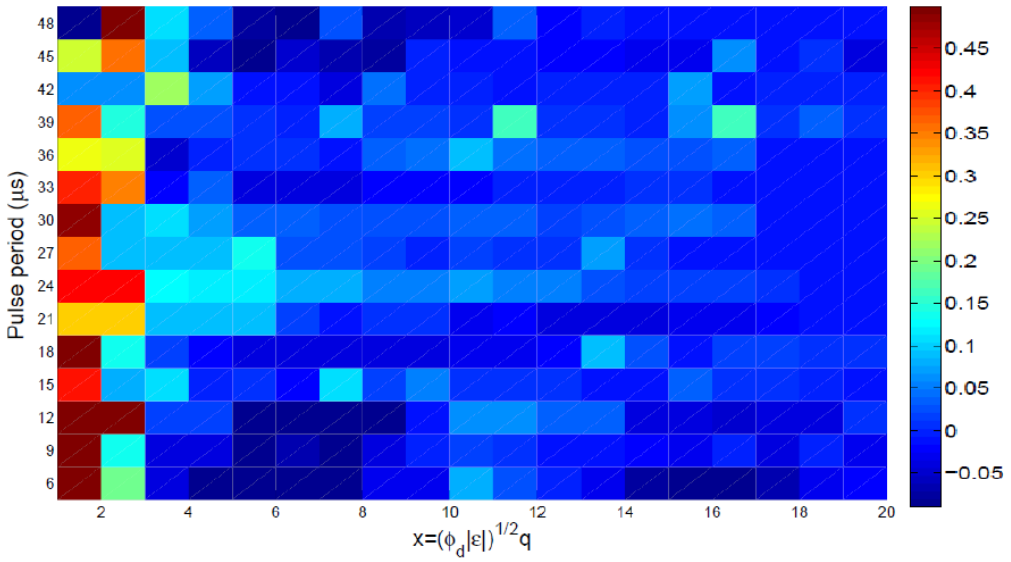

Figure 6.9: False color plot of the mean momentum current as a function of scaling variable x (the $x-$axis) and pulse period (the $y-$axis). The color scale is the magnitude and direction of the mean momentum. The deep blue color represents the lowest value of mean momentum (negative in this case) showing regions of current inversion. Note that there is a momentum current inversion close to true classical and $\varepsilon-$classical (bottom and top on the $y-$axis respectively) regimes which disappears if one goes away from either (towards the region between $\ell = 0$ and $\ell = 1$).

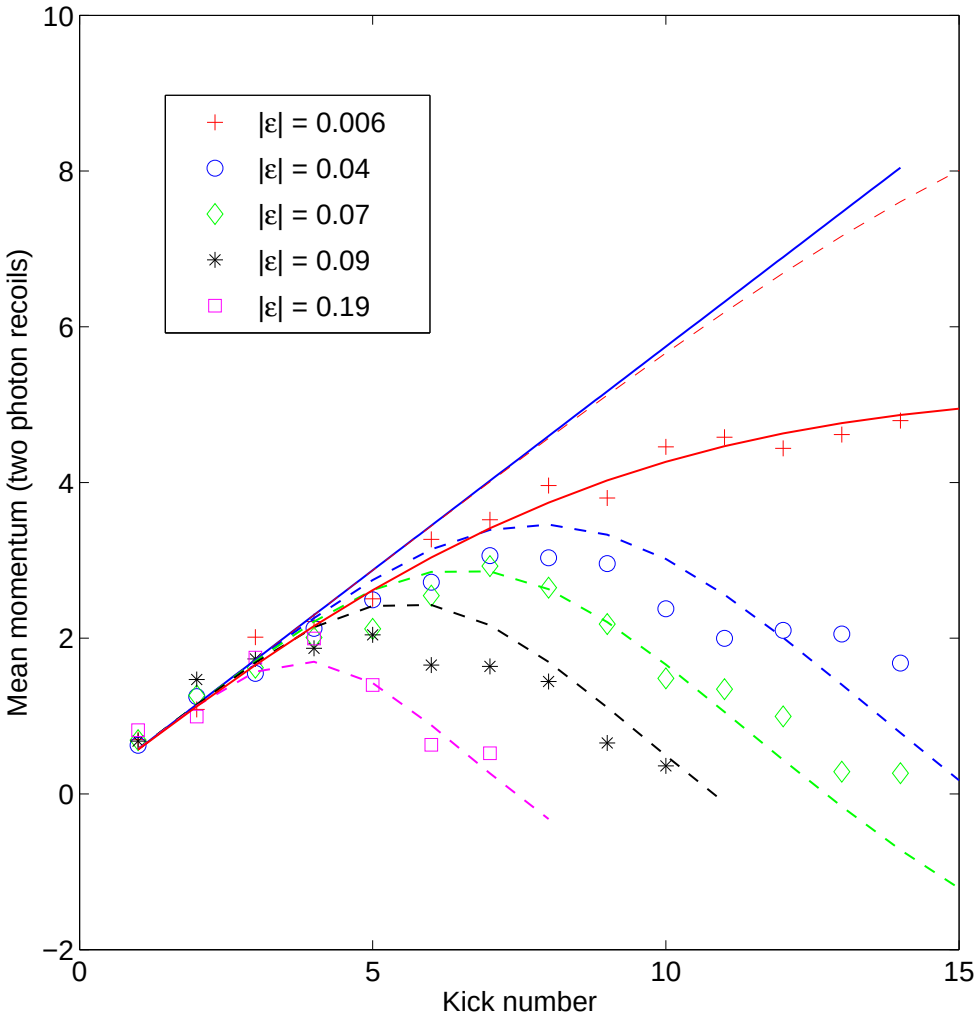

Figure 6.10: Momentum current as a function of kick number for $|\varepsilon| = 0.006$ (red crosses), $|\varepsilon| = 0.04$ (blue circles), $|\varepsilon| = 0.07$ (green diamonds), $|\varepsilon| = 0.09$ (black stars) and $|\varepsilon| = 0.19$ (purple squares). The blue solid line is the plot of $\langle p_{t,res} \rangle = -\frac{\phi_d t}{2} \sin\gamma$ for $\phi_d = 1.3$ and $\gamma = -\pi/3$. The dashed lines are the plot of Eq. (6.21) with corresponding $|\varepsilon|$ and the red solid line is the plot of Eq.(2) in Ref. [61] for $\beta = 0.5$ and $\Delta\beta = 0.02$.

quasi-momentum, $\Delta\beta$? Figure 6.10 shows a plot of momentum current as a function of kick number for $|\varepsilon| = 0.006$ (red crosses), $|\varepsilon| = 0.04$ (blue circles), $|\varepsilon| = 0.06$ (green diamonds), $|\varepsilon| = 0.09$ (black stars) and $|\varepsilon| = 0.19$ (purple squares) for fixed $\phi_d = 1.5$ and $\gamma = 4\pi/3$. The solid blue line is a plot of Eq. (6.9) and the dashed lines are plots of Eq. (6.21) for the corresponding experimental parameters. The experiment shows that the farther one goes from resonance the sooner the momentum current turns towards negative values (current reversal). These results are in good agreement with the theory except very close to resonance, where the red dashed curve fits poorly to the red crosses. For this data, we note that the suppression in momentum current is likely to be caused mainly by the effect of the initial spread of quasi-momentum. This phenomenon was also seen in Ref. [61] where the ratchet current for finite $\Delta\beta$ was given by Eq. (6.11). This equation with $\Delta\beta = 0.028$ (independently estimated from time-of-flight measurements) is also plotted in Fig. 6.10 (red solid line). It can be seen to agree well with experiment. We thus conclude that for $|\varepsilon| \gtrsim 0.04$ (corresponding to an offset from resonance of 0.3 μs), $\Delta\beta$ plays an unimportant role in the dynamics of the ratchet. This is because at resonance the total phase the momentum states acquire must be an integer multiple of 2π. Any deviation from this condition significantly suppresses the momentum current at longer times. However the momentum state phases away from resonance are already pseudo-random, so the phase changes caused by $\Delta\beta$ have a negligible effect.

In conclusion, We have performed experiments to investigate several aspects of the off-resonant atomic ratchet by exposing an initial atomic state which was a superposition of two momentum states to a series of standing wave pulses. We measured the mean momentum current as a function of a scaling variable x, which contained important pulse parameters such as the offset of the kicking period from resonance, the kick number, and the kick strength both in true classical ($\ell = 0$) and the $\varepsilon-$classical ($\ell = 1$) regimes. We showed that a scaled version of the mean momentum

in both cases could be described solely by x, a result postulated by a theory based on a classical treatment of the system [107]. The experiment verified that for certain ranges of x the momentum current exhibited an inversion. We showed that the true classical and $\varepsilon-$ classical regimes essentially display the same behavior. However it should be noted that in the $\ell = 0$ case, the amplitude of the ratchet current oscillations as a function of x are more pronounced and are a better match to the theory. We postulate that this is due to the fact that the short time between the pulses near $\ell = 0$ provides little opportunity for dephasing effects from vibrations and spontaneous emission to become important. The experiment verified that for certain ranges of x the momentum current exhibited an inversion. We also studied the effect of initial quasi-momentum width on the ratchet current away from resonance. This width has a large impact extremely close to resonance, but plays an unimportant role as we go only a little farther from resonance. Ultimately one can now control the strength and direction of the ratchet without changing the underlying relative symmetry between the initial state and the potential. In addition the crossover between classical and $\varepsilon-$classical dynamics was observed.

CHAPTER 7

Accelerator modes

The mean energy of the QDKR at quantum resonance increases ballistically while the mean momentum remains fixed. The presence of a linear potential such as gravity breaks the symmetry of the system. The experimental realization of the atom-optical quantum kicked accelerator (AOQKA) has provided a testing ground for studying aspects of the transition to chaos in both classical and quantum regimes [68]. The most striking feature is the observation of quantum accelerator modes (QAMs) [69–74, 81, 113–116]. The QAMs are characterized by a linear growth of momentum of a fraction of atomic ensemble with time. These modes appear for pulse periods close to an integer multiple of the half-Talbot time.

7.1 Theory

We now briefly review the accelerator mode theory based on the $\varepsilon-$classical model presented in Ref. [69,70]. Fishman, Guarneri, and Rebuzzini pioneered an approach to understanding the QAM, the so called $\varepsilon-$ classical theory [69,70], which describes the strongly quantum mechanical dynamics in terms of an effective classical map. It has been been used to great effect in the interpretation and prediction of experimentally observable QAMs [71, 116, 117]. They defined the closeness of the kicking period to a particular quantum resonance $\tau = 2\pi\ell$, where ℓ is an integer, by a small parameter $\varepsilon = 2\pi(T/T_{1/2} - \ell)$. It was found that $|\varepsilon|$ could be assigned the role of Planck's constant and for small $|\varepsilon|$ the dynamics can be described by a Hamiltonian which is

a formal quantization of the following maps (3.33):

$$J_{q+1} = J_q + \tilde{k}\sin\theta_{q+1} \pm \tau\eta,$$
$$\theta_{q+1} = \theta_q \pm J_q. \tag{7.1}$$

Where $\tilde{k} = |\varepsilon\phi_d|$, $\eta = mgT/\hbar G$ and $\tau = 2\pi\alpha$. The dimensionless variables J and θ are defined as

$$J_q = I_q \pm \pi\ell \pm \tau(\beta - \eta q - \eta/2) \tag{7.2}$$

and

$$\theta = GX \mod 2\pi. \tag{7.3}$$

These area-preserving maps are $2\pi-$periodic in J and θ with $p/(\hbar G) = I/|\varepsilon| + \beta$. The map of Eq. (7.1) can have period-$\mathfrak{p}$ fixed points. These fixed points are "stable" and will be surrounded by regions of phase space that can also be classified as stable. If the atomic wave packet has a sizable overlap with one of these stable islands, its momentum will grow linearly with time thus realizing the accelerator modes. The momentum of the atoms in the accelerator mode after q kicks is given by the relation

$$r = r_0 + \frac{\eta\tau}{\varepsilon}q + \frac{2\pi\mathfrak{j}}{\mathfrak{p}\varepsilon}. \tag{7.4}$$

These accelerator modes are characterized by the parameters $(\mathfrak{p}, \mathfrak{j})$ where $\mathfrak{p}$ is the order $\mathfrak{j}$ is the jumping index. The parameter $\mathfrak{p}$ represents the number of kicks required before cycling back to the initial point in phase space, while the jumping index $\mathfrak{j}$ represents the number of units of momentum acquired in each of those cycles. Modes of order 1 are given on the $2-$torus by $J_0 = 0$, $\theta_0 = \theta_{\mathfrak{j}}$ where

$$\sin(\theta_{\mathfrak{j}}) = (2\pi\mathfrak{j} \mp \tau\eta)/\tilde{k}, \tag{7.5}$$

and $\mathfrak{j}$ is any integer such that the absolute value on the right-hand side of the equation is less than 1. For a primary QAM (the most predominant modes in experiment),

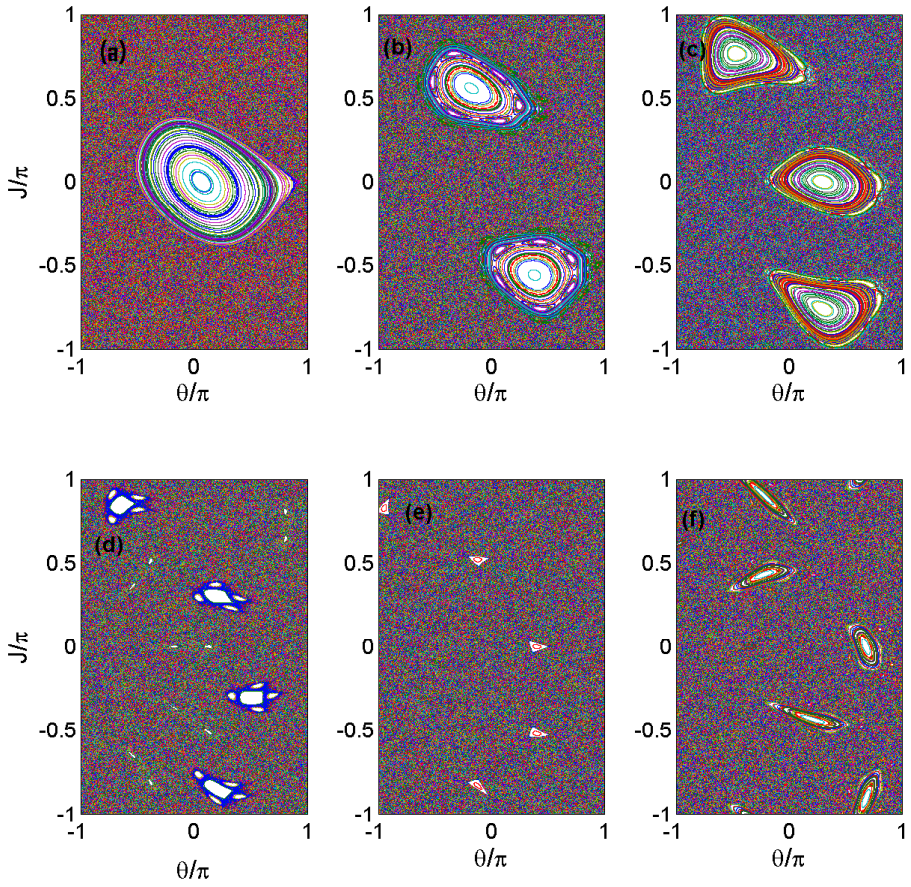

Figure 7.1: Phase space of QAMs generated by the map of Eq. (7.1) for $\tau = 5.86$, $\phi_d = 1.4$ and $\eta = 2.14$. Primary QAMs is seen with mode (a) $(\mathfrak{p}, \mathfrak{j})$= (1,0). The higher order modes are seen with mode $(\mathfrak{p}, \mathfrak{j})$ equal to (b) (2,1), (c) (3,1) (d) (4,1) (e) (5,1) and (f) (5,2).

$\mathfrak{j} = 0$,

$$r = \frac{\eta\tau}{\varepsilon} q \tag{7.6}$$

The phase space of QAMs generated by the map of (7.1) is shown in Fig. 7.1. Primary QAMs is seen with mode (a) $(\mathfrak{p}, \mathfrak{j})$= (1,0). The higher order modes with $(\mathfrak{p}, \mathfrak{j})$ equal to (b) (2,1), (c) (3,1) (d) (4,1) (e) (5,1) and (f) (5,2) are seen.

7.2 Decay of QAMs

Classical Hamiltonian systems display a combination of regular motion and chaotic motion in phase space [118]. Although there is no classical transport allowed between two regions, quantum transport is possible due to dynamical tunneling [119–121]. The wave-packets which are initially localized within the stable island leak to the chaotic region and decay after a long time. QAMs which are formed when an atomic wave-packet is at least partially trapped inside a stable island thus decays with time. The decay rate can be estimated as [122]

$$\Gamma = \frac{\omega_0}{2\pi} e^{-A/\hbar}, \tag{7.7}$$

where A is the area of the island in phase space and ω_0 is the angular frequency of the small oscillations. The decay rate can be extracted from the population of the atoms in the accelerator mode and is defined as

$$P(q) = \sum_{n(q)-\Delta n/2}^{n(q)+\Delta n/2} |\psi(n)|^2, \tag{7.8}$$

where $n(q) = n_0 - \frac{\tau\eta}{\varepsilon} q$ and Δn is the width of the accelerator mode centered at n_0. In the experiments, it is very challenging to observe the small tunneling decay since the decay of the QAM is dominated by other effects, mostly spontaneous emission and dephasing. With the scaling of

$$\frac{A}{2\pi|\varepsilon|} \approx \frac{\phi_d}{\sqrt{\tau\eta}} \tag{7.9}$$

The decay rate can be estimated as

$$\Gamma = \frac{\omega_0}{2\pi} e^{\left[\frac{-2\pi\phi_d}{\sqrt{\tau\eta}}\right]}. \tag{7.10}$$

7.3 Experimental configuration and results

We now discuss the experiments that were carried out to observe the QAMs and to investigate its decay behavior. Mostly the underlying setup was similar to that described in Sec.6.2.1. The condensate was exposed to a pulsed horizontal standing wave of wavelength λ_G. Several scans were performed by increasing the number of pulses at fixed pulse period and effective acceleration. The time-of-flight images of one such scans for $T = 49\mu$s (close to $T_{1/2} = 51.5\mu$s) and $g = 5\text{m/s}^2$ is shown in Fig. 7.2. These experimental parameters correspond to $\eta = 0.0257$ and $\varepsilon = -0.305$. The decay of the accelerator mode after a long time was calculated using an exponential fit to the population as a function of time (kick numbers) as shown in Fig. 7.3. We performed such scans for different ϕ_d and the experimentally measured decay rate as a function of ϕ_d is plotted in Fig. 7.5 (a). This shows that the decay rate decreases as ϕ_d increases as predicted by Eq. (7.2). Furthermore the area of the islands was calculated from the phase space plot of maps (7.1) as a function of ϕ_d used in Fig. 7.5 (a). The calculated areas are then plotted as a function of ϕ_d in Fig. 7.5 (b). Finally, the dependence of decay rates on the size of islands is depicted in Fig. 7.5 (c). As mentioned earlier, it is very challenging to observe decays purely from the quantum tunneling. However the observed decay rates are qualitatively in agreement with the theory, showing a decrease in decay rate with increasing ϕ_d and area. This is exactly the opposite effect one would expect from the decay due to spontaneous emission where the decay rate should increase with larger ϕ_d.

In conclusion, we have investigated the QAMs and its decay behavior. The depen-

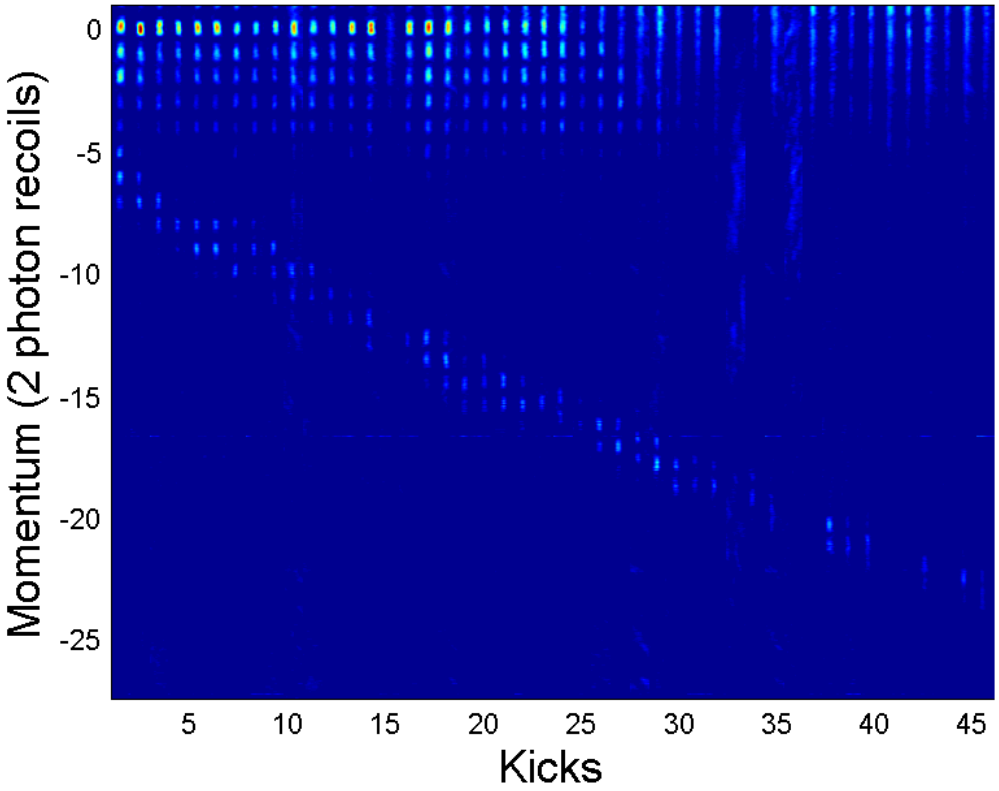

Figure 7.2: Momentum distribution of a kicked BEC as a function of kick number showing the accelerator mode close to $T_{1/2}$. The scan was performed with an effective acceleration of $g = 5\text{ms}^{-2}$, kicking strength of $\phi_d \approx 0.9$ and kicking period of $T = 49\mu\text{s}$.

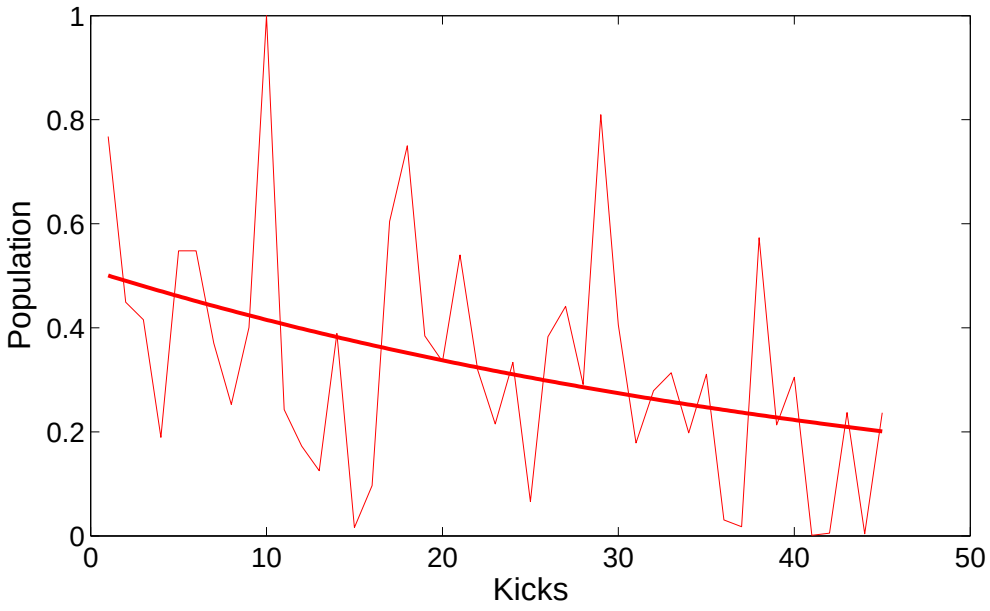

Figure 7.3: Population in the accelerator modes as a function of kick number in Fig. 7.2. The solid line is an exponential fit to the population.

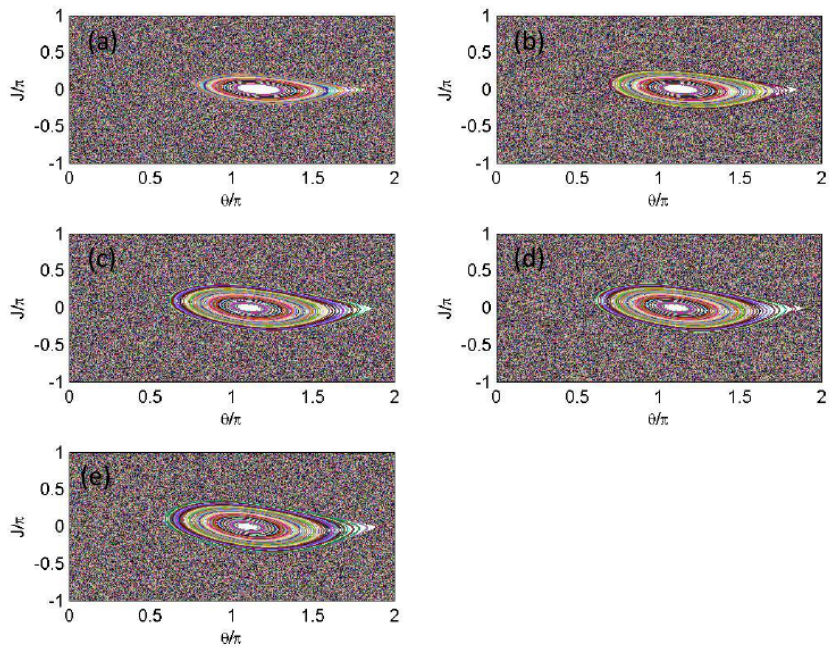

Figure 7.4: Phase space plot of the map in Eq. (7.1) for $T = 49\mu$s and $g = 5\text{m/s}^2$ for $\phi_d =$ (a) 0.88 (b) 1.06 (c) 1.3 (d) 1.4 (e)1.5.

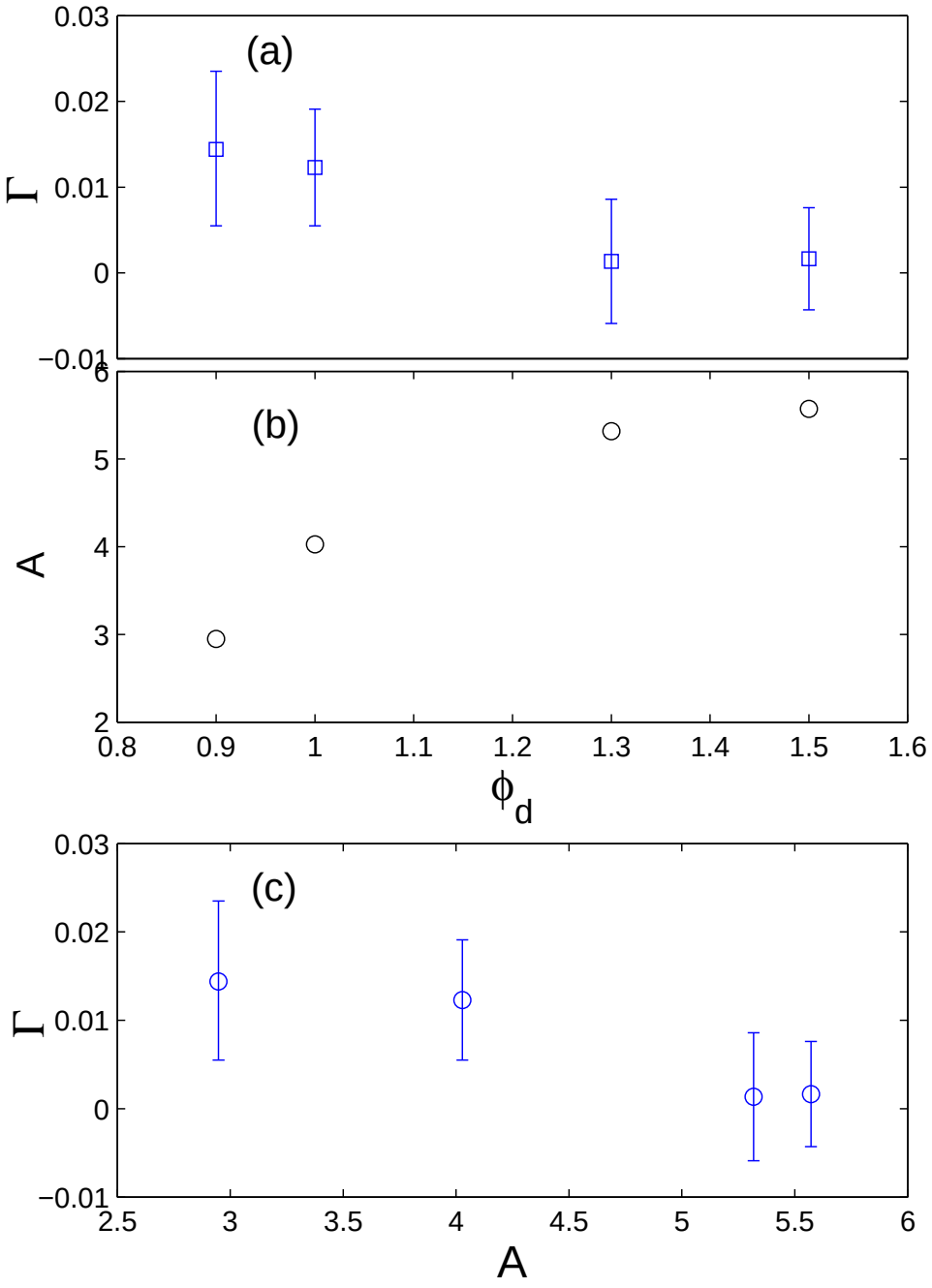

Figure 7.5: Experimentally measured decay rate Γ as a function of kicking strength ϕ_d in panel (a) and area A of the stable islands in the phase space (θ, J) plot of Eq. (7.1) as a function of kicking strength ϕ_d in panel (b) for $\tau = 5.98$ and $\eta = 0.0257$. The decay rate as a function of area of the island is plotted in (c). Error bars are the standard deviations of the exponential fitting.

dence of the decay rate on the kick strength and the area of the islands in the phase space was explored. The decay rates were found to decrease as the kick strength increased.

CHAPTER 8

CONCLUSIONS

8.1 Summary

The work described in this thesis mainly explored the applications of the atom-optical kicked rotor. The experiments began with the creation of Bose-Einstein condensate (BEC) of ^{87}Rb atoms in an all-optical trap. The quantum delta kicked rotor (QDKR) system was realized by exposing a BEC to short periodic pulses (kicks) of an off-resonant standing wave formed by the interference of two laser beams. A closely related system called quantum delta kicked accelerator (QDKA) was realized by exposing BEC to short pulses of optical standing wave in presence of external acceleration. Two main applications of the QDKR and QDKA were studied in this thesis.

Measurement of the fidelity or the overlap of a resonant QDKR state with a reference state was performed. The width of the fidelity peaks were found to scale as the inverse cube of the measurement time, in units of kicks. The sensitivity of the QDKR to the external acceleration was also investigated by performing the fidelity measurement. It was found that the fidelity width in acceleration also scaled as the inverse cube of the pulse number. Additionally, the fidelity was found to depend on the direction of external acceleration provided the distribution of atomic ensemble had some initial momentum width and was centered at a quasimomentum of 0.5 (in units of two photon recoils).

The quantum ratchet effect at a primary resonance ($T_{1/2}$) as well as away from resonance was investigated. The directed ratchet current as a function of initial mo-

mentum of the atomic ensemble and the asymmetry between the atomic distribution and potential were experimentally investigated and explained by the theory. The off-resonant ratchet behavior had some additional interesting features. It was shown to be determined by a single variable which consisted of the main experimental parameters, and in addition could exhibit inversion of the momentum current even though the underlying symmetries of the system were unaltered. The off-resonant ratchet behavior was used for crossover studies between classical and $\varepsilon-$classical regimes. The effect of the width in initial momentum on the quantum ratchet was also demonstrated.

Using a QDKA, quantum accelerator modes were studied and its decay behavior was discussed.

8.2 Future work

With the slight modification on the existing experimental setup, we have realized that a second off-resonant standing light wave with a grating vector which is one half of that of the existing standing wave can be applied. One of the distinguished features of applying two different optical lattices is that the basis momentum states for each of the spatial frequencies are independent. Both the standing waves are formed from the same off-resonant laser beam aligned at two different geometry. Using these two sets of optical lattices of different spatial periods, several interesting experiments can be performed. These include: (i) the measurement of the quantum fidelity to study quantum chaotic behavior (ii) to study the quantum non-linear dynamics of a non-Kolmogorov-Arnold-Moser system and (iii) phase selected momentum transport using a two-component kicking potential.

BIBLIOGRAPHY

[1] S. N. Bose, " Plancks Gesetz und Lichtquantenhypothese", Zeitschrift f*u*r Physik, **26**, 178 (1924.)

[2] A. Einstein, "Quantentheorie des einatomigen idealen gases", Diese. Ber., **22**, 261 (1924).

[3] A. Einstein, "Quantentheorie des einatomigen idealen gases. Zweite abhandlung", Sitzungsber. Preuss. Akad. Wiss., Bericht **1**, 3 (1925).

[4] Eric A. Cornell and Carl Wieman, "Bose-Einstein Condensation in a Dilute Gas: The First 70 Years and Some Recent Experiments", Nobel Lecture, December 8, 2001.

[5] Wolfgang Ketterle, "Nobel lecture: When Atoms Behave as Waves: Bose-Einstein Condensation and the Atom Laser", Rev. Mod. Phys. **74**, 1131 (2002).

[6] F. Dalfovo, S. Giorgini, L. P. Pitaevskii, S. Stringari, "Theory of Bose-Einstein Condensation in trapped gasses", Rev. Mod. Phys. **71**, 463 (1999).

[7] F. London, "The $\lambda-$ Phenomenon of Liquid Helium and the Bose-Einstein Degeneracy", Nature, **141**, 643 (1938).

[8] L. Tisza, "Transport Phenomenena in Helium II", Nature, **141**, 913 (1938).

[9] J. H. Van Vleck , "A Survey of the Theory of Ferromagnetism", Rev. Mod. Phys. **17**, 27 (1945).

[10] Charles Kittel, "Introduction to Solid State Physics", John Wiley and Sons, (1996).

[11] J. Bardeen, L. N. Cooper, and J. R. Schrieffer, "Microscopic Theory of Superconductivity", Phys. Rev. **106**, 162 (1957).

[12] J. Bardeen, L. N. Cooper, and J. R. Schrieffer, " Theory of Superconductivity". Phys. Rev. **108**, 1175 (1957).

[13] M.H. Anderson, J.R. Ensher, M.R. Matthews, C.E. Wieman, and E.A. Cornell, "Observation of Bose-Einstein Condensation in a dilute atomic vapor", Science **269**, 198 (1995).

[14] K. B. Davis, M.-O. Mewes, M. R. Andrews, N. J. van Druten, D. S. Durfee, D. M. Kurn, and W. Ketterle, "Bose-Einstein Condensation in a Gas of Sodium Atoms", Phys. Rev. Lett. **75**, 3969 (1995).

[15] C. C. Bradley, C. A. Sackett, J. J. Tollett, and R. G. Hulet, "Evidence of Bose-Einstein Condensation in an Atomic Gas with Attractive Interactions", Phys. Rev. Lett. **75**, 1687 (1995).

[16] C.A. Sackett, C.C. Bradley, M. Welling, R.G. Hulet, "BoseEinstein condensation of lithium", Appl. Phys. B **65**, 433 (1997).

[17] C.C. Bradley, C.A. Sackett,and R.G. Hulet, "Bose-Einstein Condensation of Lithium: Observation of Limited Condensate Number", Phys. Rev. Lett., **78**, 985 (1997).

[18] D. G. Fried, T. C. Killian, L. Willmann, D. Landhuis, S. C. Moss, D. Kleppner, and T. J. Greytak , "Bose-Einstein Condensation of Atomic Hydrogen", Phys. Rev. Lett. **81**, 3811 (1998).

[19] A. L. Migdall, J. V. Prodan, W. D. Phillips, T. H. Bergeman and H. J. Metcalf, "First Observation of Magnetically Trapped Neutral Atoms", Phys. Rev. Lett. **54**, 2596 (1985).

[20] S. Chu, J. E. Bjorkholm, A. Ashkin, and A. Cable, "Experimental Observation of Optically Trapped Atoms", Phys. Rev. Lett. **57**, 314 (1986).

[21] E. Raab, M. Prentiss, A. Cable, S. Chu, and D. Pritchard, "Trapping of Neutral-Sodium Atoms with Radiation Pressure", Phys. Rev. Lett. **59**, 2631 (1987).

[22] W. Petrich, M. H. Anderson, J. R. Ensher, and E. A. Cornell, "Forteenth International Conference on Atomic Physics", Boulder, Colorado, 1994, Book of Abstracts, 1m-7.

[23] K. B. Davis, M. O. Mewes, M. A. Joffe, and W. Ketterle, "Forteenth International Conference on Atomic Physics", Boulder, Colorado, 1994, Book of Abstracts, 1m-3.

[24] W. Petrich, M. H. Anderson, J. R. Ensher, and E. A. Cornell, "Stable, Tightly Confining Magnetic Trap for Evaporative Cooling of Neutral Atoms", Phys. Rev. Lett. **74**, 3352 (1995).

[25] M. D. Barrett, J. A. Sauer, and M. S. Chapman, "All-Optical Formation of an Atomic Bose-Einstein Condensate", Phys. Rev. Lett. **87**, 010404 (2001).

[26] Murray D. Barrett, "A Quest for BEC: An all optical alternative", Doctoral thesis, Georgia Institute of Technology, May 2002.

[27] Brian P. Timmons, "Dynamics of kicked laser cooled rubidium atoms", Doctoral thesis, Oklahoma State University, July 2006.

[28] Peyman Ahmadi, "Investigating optical atom traps for Bose-Einstein condensation", Doctoral thesis, Oklahoma State University, July 2006.

[29] Ghazal Behin Aein, "Quantum Chaos with a Bose-Einstein condensate", Doctoral thesis, Oklahoma State University, July 2007.

[30] Vijayashankar Ramareddy "Study of Quantum chaos using a kicked Bose-Einstein condensate", Doctoral thesis, Oklahoma State University, December 2008.

[31] Ishan Talukdar, "Transport and resonances in kicked Bose-Einstein condensates" Doctoral thesis, Oklahoma State University, December 2010.

[32] Wolfgang Pauli "Exclusion principle and quantum mechanics", Nobel Lecture, December 13, 1946.

[33] Masahito Ueda, "Fundamentals and New Frontiers of Bose-Einstein Condensation", (World Scientific, Singapore, 2010).

[34] L. Allen and J. H. Elberly, "Optical Resonance and Two-level Atoms", (Dover, New York, 1987).

[35] Peter E. Bernath, "Specra os Atoms and Molecules", (Oxford, New York, 1995).

[36] Harold J. Metcalf and Peter van der Straten, "Laser Cooling and Trapping", (Springer 1999).

[37] S. Chu, L. Hollberg, J. E. Bjorkholm, A. Cable, and A. Ashkin, "Three-Dimensional Viscous Confinement and Cooling of Atoms by Resonance Radiation Pressure", Phys. Rev. Lett. **55**, 48 (1995).

[38] P. D. Lett, R. N. Watts, C. I. Westbrook, W. D. Phillips, P. L. Gould, and H. J. Metcalf, "Obserevation of Atoms Laser Cooled below the Doppler Limit", Phys. Rev. Lett. **61**, 169 (1998).

[39] W. D. Phillips, "Nobel Lecture: Laser Cooling and Trapping of Neutral Atoms", Rev. Mod. Phys. **70**, 721 (1998).

[40] P. L. Gould, P. D. Lett, and W. D. Phillips, "New Measurements with Optical Molasses", in Laser Spectroscopy VIII, (SpringerVerlag, Berlin 1987).

[41] J. Dalibard and C. Cohen-Tannoudji, "Laser Cooling Below the Doppler Limit by Polarization Gradients-Simple Theoretical Models", J. Opt. Soc. Am. B **6**, 2023 (1989).

[42] Kerson Huang, "Statistical Mechanics", second edition (Wiley, New York, 1987).

[43] H. F. Hess, Bull. Am. Phys. Soc. **30**, 854 (1985).

[44] H. F. Hess, "Evaporative cooling of magnetically trapped and compressed spin-polarized hydrogen", Phys. Rev. B **34**, 3476 (1986).

[45] H. F. Hess, G. P. Kochanski, M. J. Doyle, N. Masuhara, D. Kleppner, And T. Greytak, "Magnetic trapping of spin-polarized atomic hydrogen", Phys. Rev. Lett. **59**, 672 (1987).

[46] J. D. Miller, R. A. Cline, and D. J. Heinzen, "Far-off-resonance optical trapping of atoms", Phys. Rev. A **47**, 4567 (1993).

[47] J. M. Doyle, J. C. Sandberg, I. A. Yu, C. L. Cesar, D. Kleppner, and T. J. Greytak, "Hydrogen in the submillikelvin regime: Sticking probability on superfluid ^{4}He", Phys. Rev. Lett. **67**, 603 (1991).

[48] J. M. Doyle, J. C. Sandberg, I. A. Yu, C. L. Cesar, D. Kleppner, and T. J. Greytak, "Hydrogen in the submillikelvin regime: Sticking probability on superfluid ^{4}He", Phys. Rev. Lett. **67**, 1476 (1991).

[49] K. B. Davis, M. O. Mewes, and W. Ketterle, "An analytical model for evaporative cooling of atoms", Appl. Phys. B **60**, 155 (1995).

[50] W. Ketterle and N. J. Van Druten, Adv. Atom. Mol. Opt. Phys. **37**, 181 (1996).

[51] H. Wu, C. J. Foot, "Direct simulation of evaporative cooling", J. Phys. B. **29**, L321 (1996).

[52] V. Bagnato, D. E. Pritchard, and D. Kleppner, "Bose-Einstein condensation in an external potential", Phys. Rev. A **35**, 4354 (1987).

[53] F. L. Moore, J. C. Robinson, C. F. Bharucha, B. Sundaram, and M. G. Raizen, "Atom Optics Realization of the Quantum delta-Kicked Rotor", Phys. Rev. Lett. **75**, 4598 (1995).

[54] M.G. Raizen, F.L. Moore, J.C. Robinson, C.F. Bharucha, and B. Sundaram, "An Experimental Realization of the Quantum delta-Kicked Rotor", Quantum and Semiclassical Optics **8**, 687 (1996).

[55] F. L. Moore, J. C. Robinson, C. Bharucha, P. E. Williams, and M. G. Raizen, "Observation of Dynamical Localization in Atomic Momentum Transfer: A New Testing Ground for Quantum Chaos", Phys. Rev. Lett. **73**, 2974 (1994).

[56] J. Ringot, P. Szriftgiser, J. C. Garreau, and D. Delande, "Experimental Evidence of Dynamical Localization and Delocalization in a Quasiperiodic Driven System", Phys. Rev. Lett. **85**, 2741 (2000).

[57] C. Ryu, M. F. Anderson, A. Vaziri, M. B. d′Arcy, J. M. Grossman, K. Helmerson, and W. D. Phillips, "High-Order Quantum Resonances Observed in a Periodically Kicked Bose-Einstein Condensate", Phys. Rev. Lett. **96**, 160403 (2006).

[58] F. M. Izrailev, "Simple models of quantum chaos: Spectrum and eigenfunctions", Phys. Rep. **196**, 299 (1990).

[59] W. H. Oskay, D. A. Steck, V. Milner, B. G. Klappauf, and M. G. Raizen, "Ballistic peaks at quantum resonance", Opt. Comm. **179**, 137 (2000).

[60] T. S. Monteiro, P. A. Dando, N. Hutchings , M. Isherwood, " A chaotic ratchet: proposed atom optics realisation", Phys. Rev. Lett. **89**, 194102 (2002).

[61] I. Dana, V. Ramareddy, I. Talkukdar, and G. S. Summy, "Experimental realization of quantum-resonance-ratchets", Phys. Rev. Lett. **100**, 024103 (2008).

[62] M. Sadgrove, M. Horikoshi, T. Sekimura and K. Nakagawa, "Coherent control of ballistic energy growth for a kicked Bose-Einstein condensate", Eur. Phys. J. D **45**, 229 (2007).

[63] M. Sadgrove, M. Horikoshi, T. Sekimura, and K. Nakagawa "Rectified Momentum Transport for a Kicked Bose-Einstein Condensate", Phys. Rev. Lett. **99**, 043002 (2007).

[64] I. Dana and V. Roitberg, "Quantum resonances and ratchets in freely-falling frames", Phys. Rev. E. **76**, 015201(R) (2007).

[65] E. Lundh and M. Wallin, "Ratchet Effect for Cold Atoms in an Optical Lattice", Phys. Rev. Lett. **94**, 110603 (2005).

[66] A. Wickenbrock, D. Cubero, N. A. Abdul Wahab, P. Phoonthong, F. Renzoni, "Current reversals in a rocking ratchet: the frequency domain", Phys. Rev. E **84**, 021127 (2011).

[67] T. Salger, S. Kling, T. Hecking, C. Geckeler, L. M.-Molina, M. Weitz, Science, **326**, 1241 (2009).

[68] L. E. Reichl, "The Transition to Chaos", 2nd ed.(Springer, New York, 2004).

[69] S. Fishman, I. Guarneri and L. Rebuzzini, "Stable Quantum Resonances in Atom Optics", Phys. Rev. Lett. **89**, 084101 (2002).

[70] S. Fishman, I. Guarneri and L. Rebuzzini, "A Theory of Quantum Accelerator Modes in Atom Optics", J. Stat. Phys. **110**, 911 (2003).

[71] G. Behinaein, V. Ramareddy, P. Ahmadi, and G. S. Summy, "Exploring the phase space of the quantum $\delta-$kicked accelerator", Phys. Rev. Lett. **97**, 244101 (2006).

[72] V. Ramareddy, G. Behinaein, I. Talukdar, P. Ahmadi and G. S. Summy, "High-order resonances of the quantum δ-kicked accelerator", Euro. Phys. Lett. **89**, 33001 (2010).

[73] M. K. Oberthaler, R. M. Godun, M. B. d'Arcy, G. S. Summy, and K. Burnett, "Observation of Quantum Accelerator Modes", Phys. Rev. Lett. **83**, 4447 (1999).

[74] P. Ahmadi, G. Behinaein, V. Ramareddy, and G. S. Summy, "Creation mechanism of quantum accelerator modes", Phys. Rev. A **80**, 053418 (2009).

[75] M. C. Gutzwiller, "Chaos in Classical and Quantum Mechanics", (Springer-Verlag, New York, 1990).

[76] B. V. Chirikov, "A Universal Instability of Many-Dimensional Oscillator Systems", Phys. Rep. **52** , 263, (1979).

[77] J. M. Greene, "Method for Determining a Stochastic Transition", J. Math. Phys., **20**, 1183 (1979).

[78] R. S. MacKay, "A Renormalization Approach to Invariant Circles in Area-preserving Maps", Physica D, **7**, 283 (1983).

[79] L. Deng, E. W. Hagley, J. Denschlag, J. E. Simsarian, Mark Edwards, Charles W. Clark, K. Helmerson, S. L. Rolston, and W. D. Phillips, "Temporal, Matter-Wave-Dispersion Talbot Effect", Phys. Rev. Lett. **83**, 5407 (1999).

[80] M. Lepers, V. Zehnlé and J. C. Garreau, "Kicked-rotor quantum resonances in position space", Phys. Rev. A **77**, 043628 (2008).

[81] R. M. Godun, M. B. d'Arcy, M. K. Oberthaler G. S. Summy, and K. Burnett, "Quantum Accelerator modes: a tool for atom optics", Phys. Rev. A **62**, 013411 (2000).

[82] S. J. M. Kuppens, K. L. Corwin, K. W. Miller, T. E. Chupp, and C. E. Wieman, "Loading an optical dipole trap", Phys. Rev. A **62**, 013406 (2000).

[83] W. Ketterle, K. B. Davis, M. A. Joffe, A. Martin, and D. E. Pritchard, "High Densities of Cold Atoms in a Dark Spontaneous-Force Optical Trap", Phys. Rev. Lett. **70**, 2253 (1993).

[84] G. Casati, B. V. Chirikov, F. M. Izraelev, and J. Ford, "Stochastic Behavior of a Quantum Pendulum Under a Periodic Perturbation, in Stochastic Behavior in Classical and Quantum Hamiltonian Systems", edited by G. Casati and J. Ford (Springer, Berlin, 1979), p. 334.

[85] R. A. Jalabert and H. M. Pastawski, "Environment-Independent Decoherence Rate in Classically Chaotic Systems", Phys. Rev. Lett. **86**, 2490 (2001).

[86] N. R. Cerruti and S. Tomsovic, "Sensitivity of Wave Field Evolution and Manifold Stability in Chaotic Systems", Phys. Rev. Lett. **88**, 054103 (2002).

[87] M. A. Nielsen and I. L. Chuang, "Quantum Computation and Quantum Information" (Cambridge University Press, Cambridge, 2001).

[88] P. McDowall, A. Hilliard, M. McGovern, T. Grnzweig and M. F. Andersen, "A fidelity treatment of near-resonant states in the atom-optics kicked rotor", New J. Phys. **11**, 123021 (2009).

[89] I. Talukdar, R. Shrestha and G. S. Summy, "Sub-Fourier characteristics of a δ-kicked-rotor resonance", Phys. Rev. Lett. **105**, 054103 (2010).

[90] R. A. Horne, R. H. Leonard, and C. A. Sackett, "Utility of atomic kicked-rotor interferometers for precision measurements", Phys. Rev. A **83**, 063613 (2011).

[91] D. S. Weiss, B. C. Young, and S. Chu, "Precision measurement of the photon recoil of an atom using atomic interferometry", Phys. Rev. Lett. **70**, 2706 (1993)

[92] M. Cadoret, E. de Mirandes, P . Cladé, S. Guellati-Khélifa, C. Schwob, F. Nez, L. Julien, and F. Biraben, "Combination of Bloch Oscillations with a Ramsey-Bord Interferometer: New Determination of the Fine Structure Constant", Phys. Rev. Lett. **101**, 230801 (2008).

[93] P. Cladé, E. de Mirandes, M. Cadoret, S. Guellati-Khélifa, C. Schwob, F. Nez, L. Julien, and F. Biraben, "Determination of the Fine Structure Constant Based on Bloch Oscillations of Ultracold Atoms in a Vertical Optical Lattice", Phys. Rev. Lett. **96**, 033001 (2006).

[94] S. Wimberger, I. Guarneri and S. Fishman, "Quantum resonances and decoherence for δ-kicked atoms ", Nonlinearity **16**, 1381 (2003).

[95] R. Dubertrand, I. Guarneri, and S. Wimberger, "Fidelity for kicked atoms with gravity near a quantum resonance", Phys. Rev. E **85**, 036205 (2012).

[96] S. Wimberger and A. Buchleitner, "Saturation of fidelity in the atom-optics kicked rotor", J. Phys. B **39**, L145 (2006).

[97] R. P. Feynman, R. B. Leighton, and M. Sands, "The Feynman Lectures on Physics", Vol. 1, Ch. 46, (Addison-Wesley, Reading, MA, 1963).

[98] P. Reimann, "Brownian motors: noisy transport far from equilibrium", Phys. Rep. **361**, 57 (2002).

[99] R. D. Astumian, "Thermodynamics and Kinetics of a Brownian Motor", Science **276**, 917 (1997).

[100] P. Reimann, P. Hänggi, "Introduction to the physics of Brownian motors", Appl. Phys. A **75**, 169 (2002).

[101] R. D. Astumian and P. Hänggi, "Brownian Motors ", Phys. Today **55**, No.11, 33 (2002).

[102] H., Linke; T.E., Humphrey; P.E., Lindelof; A., L¨fgren; R., Newbury; P., Omling; A.O., Sushkov; R.P., Taylor; H., Xu, "Quantum ratchets and quantum heat pumps", Appl. Phys. A, **75**(2) (2002).

[103] P. Hänggi, "Harvesting randomness ", NATURE MATERIALS **10**, 6 (2011).

[104] H. Linke, W. Sheng, A. Löfgren, H. Xu, P. Omling and P. E. Lindelof, "A quantum dot ratchet: Experiment and theory", Europhys. Lett. **44** 341 (1998).

[105] W. J. Greenleaf, M. T.Woodside, and S. M. Block, "High-Resolution, Single-Molecule Measurements of Biomolecular Motion", Annu. Rev. Biophys. Biomol. Struct. **36**, 171 (2007).

[106] J. Christof M. Gebhardt, Anabel E.-M. Clemen, Johann Jaud, and Matthias Rief, "Myosin-V is a mechanical ratchet", Proc. Nat. Acad. Sci **103**, 8680 (2006).

[107] M. Sadgrove and S. Wimberger, "Pseudo-classical theory for directed transport at quantum resonance", New J. Phys. **11**, 083027 (2009).

[108] S. Wimberger, M. Sadgrove, S. Parkins, and R. Leonhardt, "Experimental verification of a one-parameter scaling law for the quantum and "classical resonances of the atom-optics kicked rotor", Phys. Rev. A **71**, 053404 (2005).

[109] G. Casati and I. Guarneri, "Non-Recurrent Behaviour in Quantum Dynamics", Commun. Math. Phys. **95**, 121 (1984).

[110] M. Sadgrove S. Wimberger, S. Parkins, and R. Leonhardt, "Ballistic and localized transport for the atom optics kicked rotor in the limit of vanishing kicking period", Phys. Rev. Lett. **94**, 174103 (2005).

[111] H. Schanz, M.-F. Otto, R. Ketzmerick, and T. Dittrich, "Classical and Quantum Hamiltonian Ratchets", Phys. Rev. Lett. **87**, 070601 (2001).

[112] M. Sadgrove and S. Wimberger "A pseudo-classical method for the atom-optics kicked rotor: from theory to experiment and back", Adv. At. Mol. Opt. Phys. **60**, 315 (2011).

[113] M. B. d'Arcy, R. M. Godun, M. K. Oberthaler, G. S. Summy, and K. Burnett, S. A. Gardiner, "Approaching classicality in quantum accelerator modes through decoherence", Phys. Rev. E **64**, 056233 (2001).

[114] M.B. dArcy, R.M. Godun, D. Cassettari, and G.S. Summy, "An accelerator mode based technique for studying quantum chaos", Phys. Rev. A **67**, 023605 (2003).

[115] R. Bach, K. Burnett, M.B. d'Arcy, S. A. Gardiner, "Quantum-mechanical cumulant dynamics near stable periodic orbits in phase space: Application to the classical-like dynamics of quantum accelerator modes", Phys. Rev. E **71**, 033417 (2005).

[116] S. Schlunk, M.B. dArcy, S.A. Gardiner, and G.S. Summy, "Experimental observation of high-order quantum accelerator modes", Phys. Rev. Lett. **90**, 124102 (2003).

[117] Z.-Y. Ma, M. B. dArcy, and S. A. Gardiner , "Gravity-Sensitive Quantum Dynamics in Cold Atoms", Phys. Rev. Lett. **93**, 164101 (2004).

[118] A. J. Lichtenberg and A. A. Lieberman, "Regular and Chaotic Motion", (Springer-Verlag, New York, 1992).

[119] A. N. Kolmogorov, "On Conservation of Conditionally Periodic Motions for a Small Change in Hamilton's Function", Dokl. Akad. Nauk SSSR **98**, 527 (1954).

[120] V. I. Arnol'd, "Proof of a Theorem of A. N. Kolmogorov on the Preservation of Conditionally Periodic Motions under a Small Perturbation of the Hamiltonian", Uspehi Mat. Nauk **18**, 13 (1963).

[121] J. Moser, "On Invariant Curves of Area-Preserving Mappings of an Annulus", Nachr. Akad. Wiss.

[122] Michael, Sheinman ; Shmuel, Fishman; Italo, Guarneri; Laura, Rebuzzini "Decay of Quantum Accelerator Modes", Phys. Rev. A, **73**, 052110 (2006).

APPENDIX A

SWITCH

During the process of creating BEC, magnetic field due to main coil was turned on and off at different times. To facilitate this, an electronic switch was designed and built in the lab as shown in Fig. A.1. It was made up of STE250NS10 N-MOSFET. The switch was used in an inductive load (coil) which generates an induced emf and can easily damage the electonic components. In order to prevent from this type of damage, the circuit was clamped by using a fast diode. A 6.5μF nonelectrolytic and 1100μ F electrolyic capacitors were used. The gate source voltage (V_{GS}) needed to operate switch was provided by digital voltage signal from the PCI card. In order to operate it fully, $V_{GS} = 10V$ was applied.

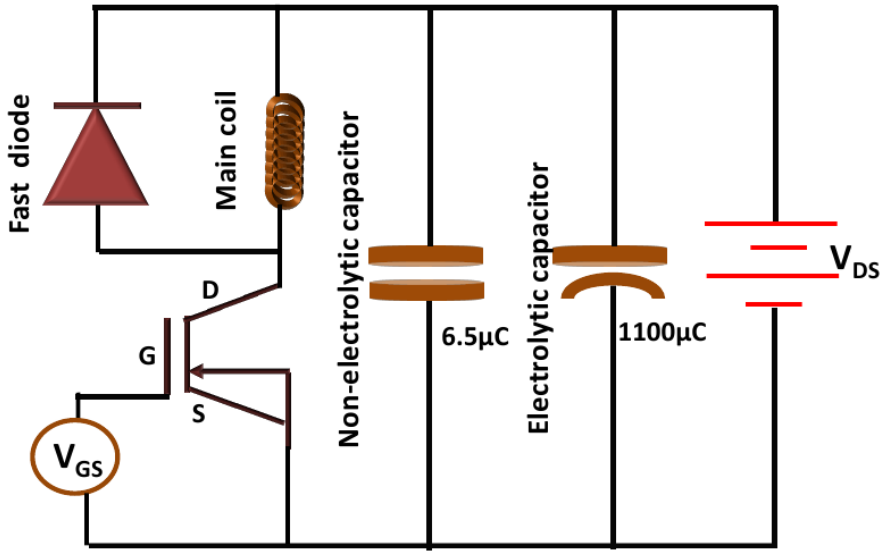

Figure A.1: Schematic drawing of the switch system used for turning the magnetic field produced by main coil on and off .

VITA

RAJENDRA KUMAR SHRESTHA

Candidate for the Degree of

Doctor of Philosophy

Dissertation: APPLICATIONS OF THE ATOM-OPTICAL KICKED ROTOR

Major Field: PHOTONICS

Biographical:

Personal Data: Born in Simjung, Gorkha, Nepal on August 01, 1978, the son of Sita Ram and Chini Maya Shrestha.

Education:

Received the Bachelor of Science degree from Tri-Chandra College, Kathmandu, Nepal, 2000, in Physics

Received the Master of Science degree from Tribhuvan University, Kirtipur, Kathmandu, Nepal, 2003, in Physics

Received the Master of Science degree from Southern Illinois University, Edwardsville, Illinois, USA, 2008, in Physics

Completed the requirements for the degree of Doctor of Philosophy with a major in Photonics Oklahoma State University in May, 2013.

Name: Rajendra Kumar Shrestha Date of Degree: May, 2013

Institution: Oklahoma State University Location: Stillwater, Oklahoma

Title of Study: APPLICATIONS OF THE ATOM-OPTICAL KICKED ROTOR

Pages in Study: 131 Candidate for the Degree of Doctor of Philosophy

Major Field: Photonics

Abstract: This thesis reports on the experimental investigation of several applications of the atom-optical quantum kicked rotor (AOQKR) using a Bose-Einstein condensate (BEC) of 87Rb atoms. The AOQKR was achieved by exposing a BEC to short periodic pulses from a horizontal optical standing wave formed from the interference of two off-resonant laser beams. In the first set of experiments the fidelity or overlap between the kicked rotor states with a reference state was studied. The fidelity resonance widths in pulse period and in acceleration were found to scale as the inverse cube of the kick numbers, a sub-Fourier behavior with possible application in precision measurement experiments. The sensitivity of the fidelity to acceleration was experimentally and theoretically investigated and found to depend on the magnitude and direction of the applied acceleration. The asymmetry between positive and negative acceleration was found to be related to the temperature of the atomic sample. In the second set of experiments, the phenomenon of a quantum ratchet (which is manifested by a directed current of particles in the absence of a net bias force) both at resonance and away from resonance was studied. It was confirmed that the current direction can be controlled by changing experimental parameters which leave the underlying symmetries of the system unchanged. It was demonstrated that this behavior can be understood using a single variable containing many of the experimental parameters. These experiments confirmed that such a ratchet behavior can under certain circumstances be the same in both the true classical and quantum regimes. The final application of the AOQKR discussed in this thesis is the quantum accelerator mode. Both the formation and decay mechanism of these modes were studied.

ADVISOR'S APPROVAL: GIL S. SUMMY